



UNIVERSIDAD DE INVESTIGACIÓN DE TECNOLOGÍA EXPERIMENTAL YACHAY

Escuela de Ciencia Físicas y Nanotecnología

TÍTULO: Photochemical Reduction of Gold and Silver Nanoparticles on Graphene Oxide

Trabajo de integración curricular presentado como requisito para la
obtención del título de Ingeniera en Nanotecnología

Autor:

Pilicita Carua Johanna Pamela

Tutor: Ph.D Sarah Briceño

Co-tutor: Ph.D Gottfried Suppan

Urcuquí, Diciembre 2021

SECRETARÍA GENERAL
(Vicerrectorado Académico/Cancillería)
ESCUELA DE CIENCIAS FÍSICAS Y NANOTECNOLOGÍA
CARRERA DE NANOTECNOLOGÍA
ACTA DE DEFENSA No. UITEY-PHY-2021-00023-AD

A los 3 días del mes de diciembre de 2021, a las 10:00 horas, de manera virtual mediante videoconferencia, y ante el Tribunal Calificador, integrado por los docentes:

Presidente Tribunal de Defensa	Dr. CHACON TORRES, JULIO CESAR , Ph.D.
Miembro No Tutor	Dra. GONZALEZ VAZQUEZ, GEMA , Ph.D.
Tutor	Dra. BRICEÑO ARAUJO, SARAH ELISA , Ph.D.

El(la) señor(ita) estudiante **PILICITA CARUA, JOHANNA PAMELA**, con cédula de identidad No. **1725085110**, de la **ESCUELA DE CIENCIAS FÍSICAS Y NANOTECNOLOGÍA**, de la Carrera de **NANOTECNOLOGÍA**, aprobada por el Consejo de Educación Superior (CES), mediante Resolución **RPC-SO-13-No.156-2015**, realiza a través de videoconferencia, la sustentación de su trabajo de titulación denominado: **Photochemical Reduction of Gold and Silver Nanoparticles on Graphene Oxide**, previa a la obtención del título de **INGENIERO/A EN NANOTECNOLOGÍA**.

El citado trabajo de titulación, fue debidamente aprobado por el(los) docente(s):

Tutor	Dra. BRICEÑO ARAUJO, SARAH ELISA , Ph.D.
Co - Tutor	Dr. SUPPAN FLORES, GOTTFRIED ANDRES , Ph.D.

Y recibió las observaciones de los otros miembros del Tribunal Calificador, las mismas que han sido incorporadas por el(la) estudiante.

Previamente cumplidos los requisitos legales y reglamentarios, el trabajo de titulación fue sustentado por el(la) estudiante y examinado por los miembros del Tribunal Calificador. Escuchada la sustentación del trabajo de titulación a través de videoconferencia, que integró la exposición de el(la) estudiante sobre el contenido de la misma y las preguntas formuladas por los miembros del Tribunal, se califica la sustentación del trabajo de titulación con las siguientes calificaciones:

Tipo	Docente	Calificación
Miembro Tribunal De Defensa	Dra. GONZALEZ VAZQUEZ, GEMA , Ph.D.	10,0
Presidente Tribunal De Defensa	Dr. CHACON TORRES, JULIO CESAR , Ph.D.	10,0
Tutor	Dra. BRICEÑO ARAUJO, SARAH ELISA , Ph.D.	10,0

Lo que da un promedio de: **10 (Diez punto Cero)**, sobre 10 (diez), equivalente a: **APROBADO**

Para constancia de lo actuado, firman los miembros del Tribunal Calificador, el/la estudiante y el/la secretario ad-hoc.

Certifico que *en cumplimiento del Decreto Ejecutivo 1017 de 16 de marzo de 2020, la defensa de trabajo de titulación (o examen de grado modalidad teórico práctica) se realizó vía virtual, por lo que las firmas de los miembros del Tribunal de Defensa de Grado, constan en forma digital.*

PILICITA CARUA, JOHANNA PAMELA
Estudiante



Dr. CHACON TORRES, JULIO CESAR , Ph.D.
Presidente Tribunal de Defensa

Dra. BRICEÑO ARAUJO, SARAH ELISA , Ph.D.
Tutor

Dra. GONZALEZ VAZQUEZ, GEMA , Ph.D.
Miembro No Tutor

CIFUENTES TAFUR, EVELYN CAROLINA
Secretario Ad-hoc

AUTORÍA

Yo, **JOHANNA PAMELA PILICITA CARUA**, con cédula de identidad 1725085110, declaro que las ideas, juicios, valoraciones, interpretaciones, consultas bibliográficas, definiciones y conceptualizaciones expuestas en el presente trabajo; así cómo, los procedimientos y herramientas utilizadas en la investigación, son de absoluta responsabilidad de el/la autora (a) del trabajo de integración curricular. Así mismo, me acojo a los reglamentos internos de la Universidad de Investigación de Tecnología Experimental Yachay.

Urcuquí, Diciembre 2021.



Johanna Pamela Pilicita Carua

CI: 1725085110

AUTORIZACIÓN DE PUBLICACIÓN

Yo, **JOHANNA PAMELA PILICITA CARUA**, con cédula de identidad 1725085110, cedo a la Universidad de Investigación de Tecnología Experimental Yachay, los derechos de publicación de la presente obra, sin que deba haber un reconocimiento económico por este concepto. Declaro además que el texto del presente trabajo de titulación no podrá ser cedido a ninguna empresa editorial para su publicación u otros fines, sin contar previamente con la autorización escrita de la Universidad.

Asimismo, autorizo a la Universidad que realice la digitalización y publicación de este trabajo de integración curricular en el repositorio virtual, de conformidad a lo dispuesto en el Art. 144 de la Ley Orgánica de Educación Superior

Urcuquí, Diciembre 2021.



Johanna Pamela Pilicita Carua

CI: 1725085110

Dedication

I would like to dedicate this research project to Nelly and Juan, for being the fundamental support of my life, for teaching me to be strong, tenacious, for motivating me to believe in my abilities regardless of adversity, for all the effort they have made to allow me to achieve my dreams. To Laydi, who every day teaches me to be a better person, for being my company and support during 22 years. To my friends from Yachay Tech, Alexandra, Saulo, and Andrés for constantly being by my side, my second family. To my family, who always gave me words of encouragement.

This thesis is also in memory of Leonor, who taught me to get up after a fall and try again.

Acknowledgements

A special acknowledgement to my advisor, Ph.D. Sarah Briceño for the academic guidance throughout the research process, also for the predisposition, support, and management which allowed me to develop the experimentation during the national emergency due to Covid-19, for advice and motivation. Other special thanks to my co-advisor, Ph.D. Gottfried Suppan who guided me in the electrochemistry area from Germany, even with the time difference of seven hours. I want to extend my sincere thanks to Ph.D. Gema González who helped with the SEM characterization, also for the support in my projects, for the guidance, advice, and constant motivation. Also, I want to thank Eng. Daniela Navas and the School of Chemical Science and Engineering for allowed me to get the approval to use the chemical laboratory, especially the potentiostat equipment to perform the electrochemistry experimentation. I would like to thank Eng. Ronny de la Bastida, who allowed me access to AFM characterization at Politécnica Nacional, which complemented my results. Finally, I would like to thank Eng. Esteban Lasso, and Eng. Joselyn Benalcázar who introduced me to the base methodology to develop my research project.

Resumen

La nanotecnología es un campo emergente que ha atraído la atención por su poderoso impacto en materiales avanzados, catalizadores, detección electroquímica entre otros. En este trabajo, se utilizó el método de reducción fotoquímica para sintetizar nanopartículas de oro y plata sobre óxido de grafeno (*GO*), los cuales tienen propiedades superficiales mejoradas para ser aplicadas en la detección electroquímica del peróxido de hidrógeno (H_2O_2). Este estudio propone la síntesis de nanopartículas plasmónicas depositadas sobre óxido de grafeno mediante irradiación de luz a una longitud de onda de excitación de 540 nm. La caracterización de los nanocompositos formados por nanopartículas de oro con caras planas sobre óxido de grafeno (*AuCNPs/GO*) y nanopartículas de plata con caras planas en sobre óxido de grafeno (*AgTNPs/GO*) se realizó mediante espectroscopía UV-Vis, Microscopía electrónica de barrido (SEM), Microscopía de fuerza atómica (AFM), Espectroscopía infrarroja por transformada de fourier (FTIR) y Espectroscopia Raman. La caracterización electroquímica de los electrodos modificados con *AgNPs/GO* y *AgTNPs/GO* se realizó mediante voltametría cíclica (CV), y los parámetros cinéticos se determinaron mediante las teorías de Nicholson Klinger & Kochi. Las propiedades de detección de los nanocompositos para la detección de H_2O_2 se estudiaron mediante voltametría cíclica. Los resultados finales muestran que el método de reducción fotoquímica produce estructuras con caras planas a partir de nanopartículas metálicas cuasi esféricas, generando *AuCNPs/GO* y *AgTNPs/GO*. Además, se observó la mejora de las propiedades de detección utilizando *AuCNPs/GO* y *AgTNPs/GO*, lo que refleja la dependencia de la detección electroquímica en el tipo, tamaño y forma de las nanopartículas. Estos resultados demuestran que el uso de la nanotecnología para crear nanomateriales novedosos permite mejorar las propiedades de los métodos de detección sensibles.

Palabras clave: Nanotecnología, Reducción fotoquímica, detección electroquímica, nanocompositos de oro, nanocompositos de plata.

Abstract

Nanotechnology is an emerging field that has attracted attention for its powerful impact on advanced materials, catalysts, electrochemical sensing, and others. In this work, the photochemical reduction method was used to synthesize gold and silver nanoparticles on graphene oxide (GO), having enhanced surface properties to be applied in the improvement of the electrochemical sensing of hydrogen peroxide (H_2O_2). This study proposes the synthesis of plasmonic nanoparticles deposited on graphene oxide by irradiation of light at 540 nm excitation wavelength. The characterization of gold nanoparticles having planar faces on graphene oxide (*AuCNPs/GO*) and silver nanoparticles having planar faces on graphene oxide (*AgTNPs/GO*) nanocomposites were done by UV-Vis spectroscopy, Scanning Electron Microscopy (SEM), Atomic Force Microscopy (AFM), Fourier Transform Infrared (FTIR), and Raman Spectroscopy. Electrochemical characterization of *AgNPs/GO* and *AgTNPs/GO* modified electrodes were performed by cyclic voltammetry (CV), and kinetic parameters were determined by Nicholson Klinger & Kochi's theories. The sensing properties of the aforementioned materials for the detection of H_2O_2 were elucidated by cyclic voltammetry. Final results show that the photochemical reduction method produces structures with planar faces from quasi-spherical metal nanoparticles, generating *AuCNPs/GO*, and *AgTNPs/GO*. Furthermore, the enhancement of detection properties using *AuCNPs/GO* and *AgTNPs/GO* was observed, which reflects the dependence of electrochemical sensing on the type, size, and shape of nanoparticles. These results demonstrate that the use of nanotechnology to create novel nanomaterials allows the improvement of the properties of sensitive detection methods.

Keywords: Nanotechnology, photochemical reduction, electrochemical sensing, gold nanocomposites, silver nanocomposites.

Contents

List of Figures	x
List of Tables	xii
1 Introduction	1
2 Motivation	3
2.1 Problem Statement	3
2.2 Objectives	4
2.2.1 General Objective	4
2.2.2 Specific Objectives	4
3 Theoretical Background	5
3.1 Nanoscience and Nanotechnology	5
3.2 Nanomaterials	5
3.2.1 Silver Nanoparticles	7
3.2.2 Gold Nanoparticles	7
3.2.3 Surface Plasmon Polariton (SPP) and Localized Surface Plasmon (LSP)	9
3.2.4 Graphene	10
3.2.5 Graphene Oxide (GO)	14
3.2.6 Nanocomposites	15
3.2.7 Photochemical Synthesis Method	17
3.3 Sensors	18
3.3.1 Electrochemical Sensors	18
4 Characterization techniques	21
4.1 Spectroscopy Techniques	21
4.1.1 Ultraviolet-Visible Spectroscopy (UV-Vis)	21
4.1.2 Fourier-Transform Infrared spectroscopy (FT-IR)	23

4.1.3	Raman spectroscopy	24
4.2	Microscopy techniques	26
4.2.1	Scanning Electron Microscopy (SEM)	26
4.2.2	Atomic Force Microscopy (AFM)	27
4.3	Electrochemical Techniques	29
4.3.1	Cyclic Voltammetry (CV)	29
5	Methodology	33
5.1	Chemicals	33
5.2	Synthesis of AgNPs/GO and AuNPs/GO nanocomposites	33
5.2.1	Preparation of <i>GO</i> dispersed solution	33
5.2.2	Light Chamber	34
5.2.3	Chemical synthesis of silver and gold nanoparticles	34
5.2.4	Synthesis of AgNPs/GO and AuNPs/GO nanocomposites	36
5.2.5	Photoreduction of the nanocomposites	36
5.3	Characterization Equipment	37
5.3.1	Spectroscopy Techniques	37
5.3.2	Microscopy techniques	39
5.3.3	Electrochemical Techniques	40
6	Results & Discussion	45
6.1	UV-Vis spectroscopy	45
6.2	Microscopy Techniques	49
6.2.1	Scanning Electron Microscopy (SEM)	49
6.2.2	Atomic Force Microscopy (AFM)	53
6.3	Fourier-Transform Infrared Spectroscopy (FTIR)	58
6.4	Raman Spectroscopy	60
6.5	Electrochemical Analysis	63
6.5.1	Cyclic Voltammetry (CV)	63
7	Conclusions & Outlook	79
	Bibliography	81

List of Figures

3.1	Top-down and bottom-up methods for synthesis of nanoparticles.	6
3.2	Illustration of Surface Plasmon Polariton along a planar metal-dielectric interface.	9
3.3	Illustration of Localized Surface Plasmon along a noble metal.	10
3.4	Graphitic allotropes generated from 2D monolayer graphene.	11
3.5	Illustration of atomic structure and energy levels of the carbon atom.	12
3.6	Hybridization of carbon atom generated in graphene layers.	13
3.7	Representation of honeycomb lattice and reciprocal lattice of graphene.	14
3.8	Illustration of graphene oxide and proposed structure models.	15
3.9	Illustration of photochemical synthesis method.	18
4.1	Schematic representation of a Double Beam UV-Vis spectrophotometer.	22
4.2	Schematic representation of an FTIR spectrophotometer.	24
4.3	Energy diagrams of Stokes, Rayleigh, and anti-Stokes Raman scattering.	25
4.4	Diagram of Raman spectroscopy system.	26
4.5	Diagram of SEM system.	27
4.6	Diagram of AFM system.	29
4.7	Diagram of the main profiles used in cyclic voltammetry.	30
4.8	Experimental setup of an electrochemical cell.	31
5.1	GO solution.	34
5.2	<i>AgNPs</i> and <i>AuNPs</i> solutions obtained before the irradiation.	35
5.3	Light chamber to perform the photo-reduction method.	36
5.4	<i>AgTNPs/GO</i> and <i>AuCNPs/GO</i> solutions obtained by photo-reduction method.	37
5.5	Genova Nano Jenway Spectrophotometer.	38
5.6	Agilent Cary 630 FTIR Spectrometer.	38
5.7	Horiba Scientific - LabRAM Aramis Raman spectrometer.	39
5.8	NaioAFM equipment at Escuela Politécnica Nacional.	40
5.9	μ Stat300 potentiostat equipment.	41
5.10	Graphite electrodes used in the electrochemical methods.	41

5.11	Design of three-electrode micro-cell system.	42
6.1	UV-Vis spectrum of <i>GO</i> dispersed solution.	45
6.2	UV-Vis spectrum of <i>AuNPs/GO</i> and <i>AuCNPs/GO</i>	46
6.3	UV-Vis spectrum of <i>AgNPs/GO</i> and <i>AgTNPs/GO</i>	47
6.4	SEM micrographs of <i>AuCNPs/GO</i>	50
6.5	SEM characterization for <i>AgTNPs/GO</i>	52
6.6	AFM characterization of <i>AuNPs/GO</i>	54
6.7	AFM characterization of <i>AuCNPs/GO</i>	55
6.8	AFM characterization of <i>AgNPs/GO</i>	56
6.9	AFM characterization of <i>AgTNPs/GO</i>	57
6.10	FT-IR spectrum of <i>GO</i>	58
6.11	FTIR Analysis spectra.	59
6.12	Raman spectroscopy analysis.	61
6.13	Cyclic voltammograms for modified <i>GE</i> in an aqueous 1wt. % <i>NaCl</i> electrolyte.	64
6.14	Cyclic voltammograms of 2.5 mM potassium ferricyanide in 0.1 M <i>KCl</i> at modified <i>GE</i> and bare <i>GE</i>	65
6.15	Cyclic voltammograms for modified <i>GE</i> at 2.5 mM of potassium ferricyanide at different scan rates.	66
6.16	Linear Randles-Sevcik plots for anodic and cathodic peaks.	67
6.17	Plots of ψ vs $Yv^{-1/2}$ in potassium ferricyanide at modified electrodes, for the calculation of k^0	70
6.18	Cyclic voltammograms for different concentrations of H_2O_2 in 0.1 M phosphate buffer.	72
6.19	Linear regression to analyze the performance metrics of the nanocomposite-based electrodes.	73
6.20	Stability test recorded for the modified <i>GEs</i>	76
6.21	Percentual decay of the electrochemical signal as a function of the scan number.	77

List of Tables

3.1	Classification of nanomaterials: definition, examples, and applications.	8
3.2	Main methods used for the synthesis of graphene.	12
4.1	Types of reversibility and electrochemical kinetics of different reactions.	30
6.1	UV-Vis absorption bands of <i>GO</i> dispersed, <i>AuNPs/GO</i> , <i>AuCNPs/GO</i> , <i>AgNPs/GO</i> , and <i>AgTNPs/GO</i>	48
6.2	FTIR absorption peaks positions.	60
6.3	Raman bands of <i>GO</i> , <i>AuCNPs/GO</i> and <i>AgTNPs/GO</i>	62
6.4	Diffusion coefficients.	68
6.5	Charge transfer coefficient α	69
6.6	Peak potential separation ΔE_p for 2.5 mM of potassium ferricyanide.	69
6.7	Standard Rate Constant k°	70
6.8	Performance metrics of the nanocomposite-modified electrodes.	74

Chapter 1

Introduction

Nanomaterials have attracted the interest of many researchers due to their enhanced properties strongly dependent on their size and shape¹. The large surface area and quantum mechanical behavior of nano-scaled materials affect the chemical reactivity and electrical, optical, and magnetic properties², therefore, nanomaterials have a wide field of applications³. Metal nanoparticles, specifically gold and silver, can be synthesized using different routes, to obtain very distinct shapes and sizes^{4,5}. Furthermore, by induction of light in metals, oscillations of electrons just in the resonance wavelength are produced, which enhances the spatial resolution depending on the shape of the particles⁶. Based on the easy manipulation of their properties and the high spatial resolution generated by LSPR, both are used in many fields, especially in biosensing which is the main interest in this research work^{7,8}. Nanomaterials tend to agglomerate due to the strong forces of attraction generated by their small size, therefore, it is necessary to stabilize them on a surface that attracts metal ions to act as crystal growth sites and form a nanocomposite, in this case graphene oxide (*GO*) has been used as support for metal nanoparticles⁹.

Gold and silver nanoparticles generate quasi-spherical structures^{10,11}, but using the ability of *Au* and *Ag* to promote dislocation in the atomic planes due to their low stacking-fault energy, the formation of planar structures can be generated by exposing the nanoparticles to an etching agent¹². Furthermore, the plasmonic properties of nanoparticles allow their growth when they are exposed to different plasmon excitations¹³, therefore, a photochemical reduction method could be applied to improve the process. Surface Plasmon Resonance (SPR) for *Au* occurs at a shorter wavelength than *Ag*, consequently, the range of tunability is broader for *Ag* nanoparticles, which generates a better response in the formation of well-defined nanoparticles for *Ag* than *Au* nanostructures¹⁴. Synthesis of *Au* and *Ag* nanoparticles using the same method could reflect the differences in properties due to the different SPR of each one.

Synergistic properties between *GO* and metal nanoparticles enhance the stability, dispersion, and catalytic activity of nanocomposites, which is an important feature to be applied in the sensing field¹⁵. There are many investigations where the spherical nanoparticles suspended on *GO* used for detection are studied^{9,16,17}, but few promote the use of nanoparticles having planar faces such as nanoprism or nanocubic shapes with enhanced properties to improve the recognition signal in the detection process. Electrochemical sensors, although are widely applied in the industry

due to their low cost and portability¹⁸, in many cases, generate a low signal due to deficiencies in their architecture. However, the implementation of nanomaterials has been proposed to increase the sensitivity of the device and solve this problem¹⁹. Hydrogen peroxide is considered an essential component used in many fields of industry, therefore, it is of great importance to developing low-cost and high-sensitivity H_2O_2 sensors²⁰. H_2O_2 detection could be performed through electrochemical methods, using metal nanoparticles modified electrodes to produce an enhanced signal which can be easily detected¹⁶.

A novel simplified photochemical method for the synthesis in an aqueous solution of silver nanoprisms using Light Emission Diodes was reported by Saade and Araújo in 2014²¹. The research gives information about the shape, size, and stability of *AgNPs* generating an excellent potential for different applications, due to the simple and low-cost method used for their fabrication. But, is it possible to use the same process in the synthesis of particles that have similar properties, such as in the example of the production of gold nanoparticles with enhanced properties?. Solati A. *et al*¹⁴ reported the effects generated when *AuNPs* and *AgNPs* were synthesized using a similar method to Saade and Araújo, resulting in different enhanced properties of each nanoparticle. These types of nanoparticles could be used in studies related to the shape dependence of metallic nanoparticles in the electrocatalytic behavior, as it is explained by Bansal V. *et al* who describe that electrocatalysis is enhanced depending on the shape and size of nanoparticles, given aperture to the investigation of the electrocatalytic reduction of H_2O_2 through electrochemical methods. Then, Shahid M. *et al*¹⁶ describe the fabrication of modified electrodes with nanocomposite formed by graphene and nanoparticles to detect the presence of H_2O_2 in a solution. Although the method described by Saade and Araújo has been investigated with different irradiation wavelengths, Lasso E. demonstrates in his graduation project that nanoparticles with improved electrochemical properties and high viability to be used as materials in electrochemical sensing can be obtained using a wavelength around 540 nm.

In this research work, quasi-spherical gold and silver nanoparticles on graphene oxide (*AuNPs/GO* and *AgNPs/GO*) have been synthesized using a wet chemical method. Subsequently, *AuNPs/GO* and *AgNPs/GO* are exposed to the photochemical reduction method using an irradiation light wavelength of 540 nm to promote the growth of nanoparticles having planar faces on the surface of *GO*. Nanocomposites obtained from the photochemical reduction method are gold nanoparticles with planar faces on graphene oxide (*AuCNPs/GO*) and silver nanoparticles with planar faces on graphene oxide (*AgTNPs/GO*) nanocomposites which have great potential to be used in the enhancement of electrochemical detection techniques. The samples were characterized by UV-Vis spectroscopy, Fourier Transform Infrared spectroscopy (FTIR), Raman spectroscopy. Scanning Electron Microscopy (SEM) and Atomic Force Microscopy (AFM) were used as a complement microscopy characterization to obtain information about the size and shape of the nanoparticles. Finally, electrochemical characterization was performed to determine the potential of *AuCNPs/GO* and *AgTNPs/GO* as electrochemical sensors using modified electrodes with nanocomposites having enhanced surface properties. The expectations of this work are focused on the fabrication of modified electrodes that allow generating high detection signals for low concentrations of H_2O_2 , thus improving the sensing capabilities.

Chapter 2

Motivation

2.1 Problem Statement

Over the years, nanoparticles have been studied due to their high surface area by their small sizes and their controlled-shape, especially the metallic nanoparticles which have a broad field of applications due to their unique properties^{7 22 23 8}. Most research uses simple spherical nanoparticles because the synthesis method is effortless. However, size and shape dependence on the properties enhancement of gold and silver nanoparticles has been verified^{24 5}, but few studies provide information on low-cost methods for the synthesis of metallic nanoparticles with improved properties. Based on the literature, it can be suggested that gold and silver nanoparticles with specific shapes and sizes can be applied to enhance electrochemical detection and biosensors²⁵. To fabricate stable *Au* and *Ag* nanoparticles, the photochemical reduction method is proposed to synthesize small-size nanocomposites with structures having planar faces. The methodology describes the synthesis of nanocomposites having nanoparticles with enhanced interaction surface properties, which uses light to photo-convert quasi-spherical nanoparticles into other specific shapes. Also, dispersed graphene oxide is added to the nanoparticles to avoid agglomerations and improve the stability of the nanocomposite acting like a matrix support^{26 27}.

This research project aims to compare the size and shape dependence of *AuCNPs/GO* and *AgTNPs/GO* nanocomposites, for its potential application as an electrochemical H_2O_2 sensor. Subsequently, after identifying and studying the differences in size, shape, and the structural properties of *AuNPs/GO*, *AgNPs/GO*, *AuCNPs/GO* and *AgTNPs/GO*, an evaluation of the capacity of *AuCNPs/GO* and *AgTNPs/GO* in the generation of the high detection signal is performed. Also, the influence of the size and shape of the nanoparticles on the electrocatalytic behavior of the nanocomposites is studied because it is directly related to the detection properties or the enhancement of the signal. Finally, a comparison between *AuCNPs/GO* and *AgTNPs/GO* nanocomposites modified electrodes is performed to determine the stability and efficiency of an electrochemical sensor.

2.2 Objectives

2.2.1 General Objective

To compare the structural and electrochemical properties of gold and silver nanoparticles on the surface of graphene oxide for the detection of H_2O_2 .

2.2.2 Specific Objectives

- Synthesis of *AuNPs/GO*, *AgNPs/GO*, *AuCNPs/GO* and *AgTNPs/GO* using the photochemical reduction method.
- Characterization of the nanocomposites by using UV-Vis, Scanning Electron Microscopy (SEM), Atomic Force Microscopy, Fourier-Transform Infrared spectroscopy (FT-IR), and Raman spectroscopy.
- Characterization of the nanocomposites by electrochemical methods to determine the kinetic parameters using cyclic voltammetry.
- Fabrication of *AuCNPs/GO* and *AgTNPs/GO* modified carbon electrodes and a home-made electrochemical cell to evaluate their response for H_2O_2 .
- Comparative analysis of the structural properties of *AuCNPs/GO* and *AgTNPs/GO* with the electrochemical response for the detection of H_2O_2 .

Chapter 3

Theoretical Background

3.1 Nanoscience and Nanotechnology

Nanoscience is the study of properties, phenomena, behavior, and manipulation of nano-scaled materials to demonstrate their mechanical, optical, chemical, and electrical properties. The Greek term "nano" refers to the reduced size of materials to the billionth part of a meter^{28 29}. Therefore, nanotechnology is the field focused on the production, design, characterization, and application of micro and macro devices or materials with atomic precision³⁰. Professor Richard Feynman sparked interest in knowing and learning how to control materials at the atomic and molecular levels. In December 1959 during the talk "There is plenty of room at the bottom" he showed his vision about a new technology that would allow manipulating microscopic materials, giving rise to the first discussion on the field known today as nanotechnology³¹. Materials at the nanoscale have unique and specific properties, due to these exceptional characteristics their area of applications is broad. Therefore, the study of nanoscience and nanotechnology has allowed the creation of different types of nanomaterials, increasingly sophisticated characterization equipment with nanometric resolution, and several ways have been found to control their properties for specific objectives.

3.2 Nanomaterials

Nanomaterials are materials with sizes smaller than 100 nm in at least one dimension in their structural composition elements. The properties of nanomaterials strongly depend on their small size, for this reason, it is necessary to have previous knowledge of physics, chemistry, and materials science to understand their behavior¹. A nanomaterial has a very fine grain size and is classified according to spatial dimensionality as zero-dimensional material (0D) such as spheres or clusters, one-dimensional material (1D) such as nanofibers, nanorods or nanowires, two-dimensional material (2D) such as nanofilms and nanorods and three-dimensional material (3D) such as nanostructured materials or nanoparticles³². The main characteristics of nano-sized materials are, (i) they have a greater surface area than a material of the same composition on a larger scale and (ii) their behavior is dominated by quantum theory. The first

directly affects the chemical reactivity and electrical properties, and the second involves the optical, electrical, and magnetic behavior². The methods used for the manufacture and synthesis of nanomaterials depend on the properties, morphology, and applications of each material. Two techniques are used primarily because they allow controlling the synthesis of materials at the nanoscale. Top-down, such as Laser ablation, ball milling, lithography, and others which enable producing nanomaterials from materials of a larger size. Bottom-up such as chemical vapor deposition (CVD), atomic layer deposition, electrodeposition, among others that allow us to create nanomaterials from smaller components such as atoms or molecules^{32,33}. Top-down and bottom-up methods are shown in Fig. 3.1.

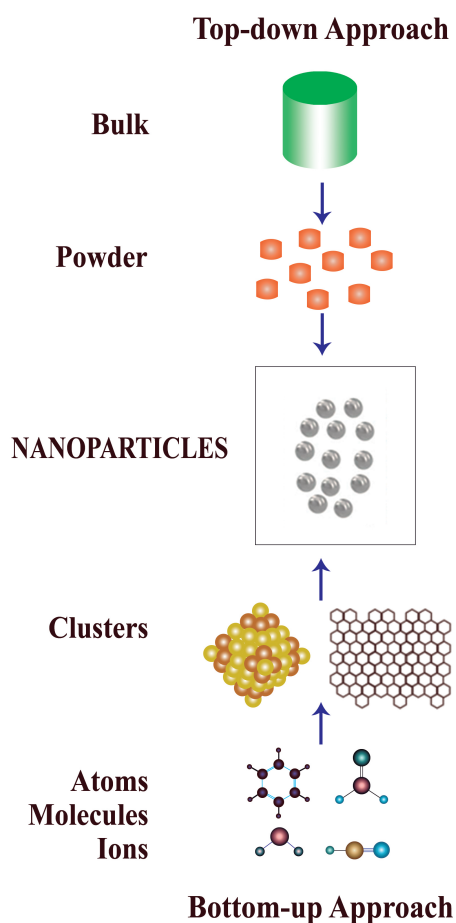


Figure 3.1: Methods used in manufacture and synthesis of nanoparticles: (i) Top-down approach which uses bulk materials to form nanoparticles. (ii) Bottom-up approach which allows forming clusters from atoms or molecules to create nanoparticles.

The fundamental component in the fabrication of nanomaterials is the nanoparticle. Nanoparticles (NPs) are only in the range of 1 to 100 nm and can be found in 0D, 1D, 2D, 3D depending on the shape of the synthesized material³⁴. The nano-size characteristic of NPs is responsible for the physicochemical properties of a substance. NPs can be synthesized using different techniques that show the variation of shape and size through the specific color of the sample, any disturbance or change in the reagents used can alter their properties, for this reason, those are novel materials and have a wide field of applications³. NPs are classified according to their morphology, size, and chemical properties, but the better-defined NPs organization is shown in Table. 3.1.

3.2.1 Silver Nanoparticles

Silver nanoparticles (AgNPs) are materials synthesized using silver noble metal as the precursor. They have a broad application field due to their physical properties such as optical, electrical, and magnetic that depend directly on their small size and shape²⁴. Also, they have specific chemical properties including biological and high thermal conductivity⁸. AgNPs are used in antibacterial applications, drug delivery, medical coatings, cosmetic products, electronic components, composite fibers, diagnosis, and biosensors materials^{23,8}. Silver nanoparticles can be easily synthesized using gas-phase, solid-phase, and liquid-phase routes. Gas and solid-phase routes are physical syntheses and the liquid-phase route includes chemical and environmental-friendly synthesis⁴. AgNPs is widely used owing to their localized surface plasmon resonance, easy production methods and high conductivity, but this kind of nanoparticles are not entirely stable because they tend to oxidize in presence of oxygen⁴.

3.2.2 Gold Nanoparticles

Gold nanoparticles like AuNPs are widely applied due to their size and shape-dependent properties. AuNPs show the surface plasmon absorption in the visible region³⁵. As all nanomaterials, their electronic, magnetic, optical, physical, and chemical properties differ from bulk to nanoscale³⁶. Base on the synthesis method, AuNPs can present different shapes such as spherical, nanoprisms, nanorods, nanocubes, and nanoshells⁵. AuNPs are used for drug delivery, chemical sensors, environmental remediation, DNA detection, and genomics-based on their versatile surface chemistry and specific properties²². They are synthesized using different physical, chemical, and biological routes depending on the size, shape, and application required³⁷. The relevant properties attributed to gold nanoparticles are conductivity, physicochemical, and surface plasmon resonance which are helpful for biosensing⁷.

Nanoparticles in general can be classified according to their composition, morphology and physical and chemical properties. The most current types are carbon-based nanoparticles, metallic-based nanoparticles, ceramic-based nanoparticles, semiconductor-based nanoparticles, and polymeric-based nanoparticles. Some examples, the main characteristics and the potential applications of the different types of nanoparticles are exposed in Table 3.1.

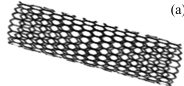
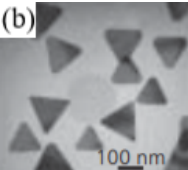
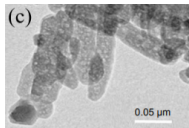
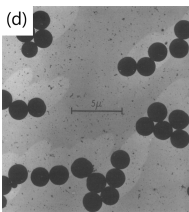
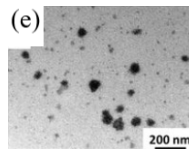
Carbon NPs	Metallic NPs	Ceramic NPs	Semiconductor NPs	Polymeric NPs
 (a)	 (b)	 (c)	 (d)	 (e)
Carbon nanotubes Graphene oxide Fullerenes Graphene quantum dots	They are synthesized using metal precursors to obtain specific optoelectrical properties due to the well-known localized surface plasmon resonance (LSPR)	Inorganic systems can be synthesized to modified size, shape, and porosity without changing pH. For example hydroxyapatite, calcium carbonate, zirconia, alumina.	They have a strong luminescence at visible range due to bandgap, which allows having a size depended on emission. For example Silicon, GaN, CdSe.	They are prepared using polymers. They are biodegradable, stable, easy to synthesis, and large-scale fabrication.
Applications				
Biosensing Drug delivery Tissue engineering Imaging Diagnosis	Antimicrobial Cancer therapy Diagnosis Drug delivery Imaging ROS scavenging Wound healing	Drug delivery Bone tissue engineering Pharmaceutical science Photodynamic therapy Gene delivery	Optoelectronics Solar energy conversion Catalysis Luminescence	Medicine Electronics Sensors to pollution Drug delivery Photonics

Table 3.1: Classification of nanoparticles: definition, examples, and applications. Carbon-based NPs: (a) carbon nanotubes³⁸. Metal-based NPs: (b) TEM micrograph of triangular silver nanoplates^{39 340}. Ceramic-based NPs: (c) TEM micrograph of rod-shaped hydroxyapatite (HAp) nanoparticles^{41 42}. Semiconductor-based NPs: (d) Electron micrograph of silica spheres nanoparticles^{43 44 45}. Polymeric-based NPs: (e) TEM image of PDMAEMA polymer nanoparticles^{46 47 48}.

3.2.3 Surface Plasmon Polariton (SPP) and Localized Surface Plasmon (LSP)

Surface Plasmon Polariton is the surface electromagnetic wave that occurs along the planar metal-dielectric interface⁴⁹. This phenomenon happens mainly on the surface of metallic nanoparticles. When an intense wavelength of light is irradiated on the small surface of a nanoparticle, its electron cloud generates a wave (oscillation) coherent with the wavelength of induced light. As is shown in Fig. 3.2 the electric field is coming through which creates a distortion in the electron cloud that makes up that surface plasmon. Therefore, the incident light is absorbed if is in tune with the resonant frequency of the surface plasmon. This physical effect is responsible for the nanoparticles having a specific color⁵⁰. This behavior intensifies the electromagnetic response at the interface leading to an improvement in the sensitivity of SPPs as a function of surface conditions⁴⁹.

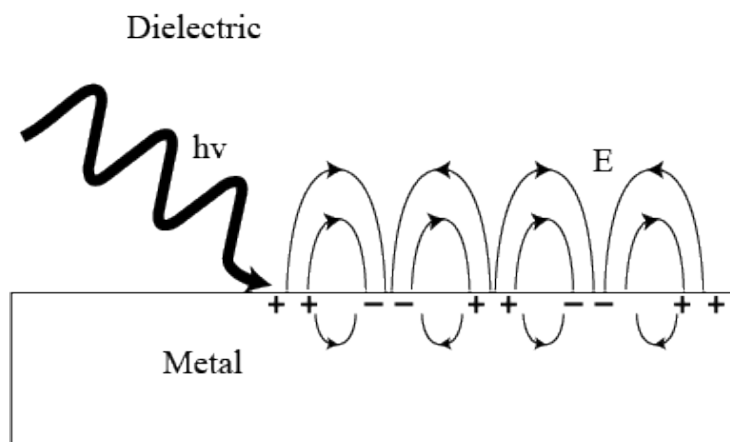


Figure 3.2: Illustration of propagation of surface Plasmon Polariton along the planar metal-dielectric interface, where an external electric field distorts in the electron cloud of the metal.

Localized Surface Plasmon is an optical effect generated by the induction of light in noble metals producing the collective oscillations of electrons in the conduction band. LSP takes place only in materials with a negative and small positive dielectric constant to generate a temporal dipole moment⁵¹, as illustrated in Fig. 3.3. The near-field amplitude is enhanced just in the resonance wavelength, which means an enhancement in light intensity resulting in a high spatial resolution which highly depends on the size of nanoparticles⁶. SPR is induced plasmons oscillating along the surface of metal-dielectric and LSPR is induced plasmons oscillating locally to the nanostructure. As a result, the resonant condition created in LSPR produces an increase in the scattering and absorption useful for biosensing⁵².

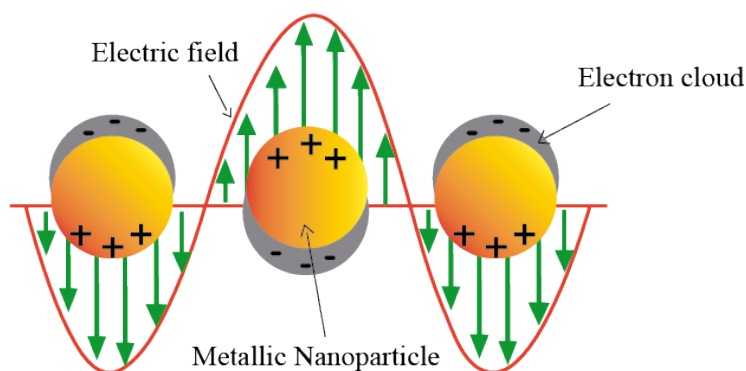


Figure 3.3: Illustration of oscillation of Localized Surface Plasmon along a noble metal, where a temporal dipole moment is generated due to the induction of light.

3.2.4 Graphene

Graphene is a carbon-based material studied theoretically since 1947 by Wallace who described the instability of semi-metallic phase in 2-dimensional graphite. Even so, several studies were performed to studying the properties of graphite in two dimensions, until 2004 when Novoselov and Geim exhibited research for producing monolayer graphene using the mechanical exfoliation method⁵³. Graphene is a one-atom-thick planar sheet of carbon atoms packed in a honeycomb crystal structure⁵⁴. 2D monolayer graphene has sp^2 -bonded carbon atoms being the essential structural element of graphite, carbon nanotubes, fullerenes, and other carbon allotropes⁵⁵ shown in Fig. 3.4. All of the them are classified as carbon-based nanoparticles because are synthesized from a carbon-structured precursor. Graphite is a 3D carbon allotrope which can be used as electrode material because it is a good conductor of electricity with a high melting point⁵⁶. Graphene is a 2D carbon allotrope, its very thin atomic thickness unify with the sp^2 -bonded carbon atoms allows the graphene structure to be the stronger and stiffer material which can be used in many applications⁵⁷. Fullerene is a 0D carbon allotrope, it spherical geometry is very stable, resist high temperatures and pressures to be used in batteries and others electronic devices⁵⁶. Carbon nanotube is a 1D carbon allotrope which also can be used as electrode due to its high surface area and high electrical and thermal conductivity⁵⁸.

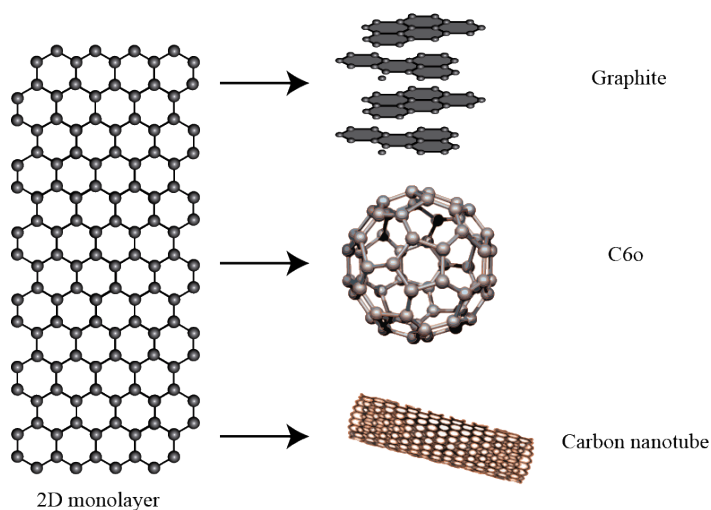


Figure 3.4: sp^2 -bonded carbon atoms in a 2D monolayer graphene and more graphitic forms: 0D (fullerenes), 1D (nanotubes), and 3D (graphite).

Characterizations of graphene over the years have demonstrated its extraordinary properties including extreme mechanical strength, high thermal conductivity, high current density, ballistic transport, chemical inertness, and superhydrophobicity^{59 54}. In addition, these properties have allowed the development of countless applications for graphene in nano-electronic devices, transparent conductors, nanocomposites, energy storage and energy conversion devices, drug delivery, biosensing, and chemical sensors⁵⁷. Graphene is currently synthesized on a small and large scale using the methods described in the diagram shown in Table. 3.2. Chemical Vapor Deposition is an effective method to produce uniform and high quality graphene at large scale. Exfoliation method produces good quality graphene in a very easy way which could be used in low cost productions. Epitaxial Growth helps in the large scale production of few-layer graphene being a potential method to be applied in the industry. Finally, Wet-Chemical is a low cost method which generates specifically graphene oxide, this technique is used for the requirements of this work in order to obtain a stable graphene oxide to be used in the formation of a nanocomposite⁶⁰.

GRAPHENE SYNTHESIS METHODS			
Chemical Vapor Deposition (CVD)	Exfoliation	Epitaxial Growth	Wet-Chemistry
It uses a nanoscale thick thin layer of a transition metal deposited on an isolated substrate into a furnace to be heated up to 1000° C in a hydrocarbon gas of methane or hydrogen environment.	It consists of removing mechanically a part of the surface from highly ordered graphite crystals using Scotch tape, to obtain single-layer graphene with good structural and electrical quality.	It involves the annealing of SiC crystal at controlled and high temperature and vacuum to obtain multilayer graphene. The quality and number of layers can be easily controlled by changing the conditions of the precursors.	It is based on the transformation of graphite into acid-intercalated graphite oxide to be evaporated, ultrasound, and centrifugated to obtain precipitation of graphene.

Table 3.2: Main methods used for graphene synthesis: chemical vapor deposition (CVD), exfoliation method, epitaxial growth, and wet-chemistry method. Information adapted from Sergey Mikhailov⁶⁰.

Graphene structure

Graphene is made up entirely of carbon atoms. Carbon is the sixth element in the periodic table and the most important one due to its ability to form bonding geometries in sp^1 , sp^2 , and sp^3 hybridizations at one-, two- and three-dimensional space correspondingly. The carbon atom has six electrons, two in the first orbital strongly bonded to the nucleus and four as valence electrons⁶¹. Atomic structure and energy levels of the carbon atom are observed in Fig. 3.5.

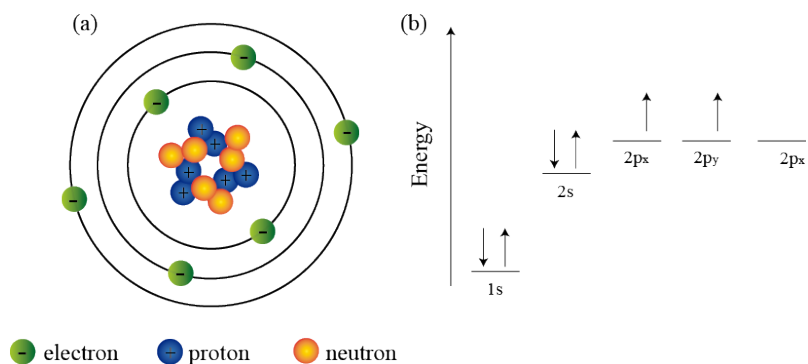


Figure 3.5: (a) Atomic structure of carbon atom. (b) Energy levels for outer electrons in the carbon atom.

Graphene shares sp^2 electrons with their neighboring carbon atoms to form a mesh-like hexagonal planar structure constituting a two-dimensional lattice⁵³. In graphene, three electrons of each carbon atom along the edges of the hexagons are σ -bonds corresponding to sp^2 hybridization. As well, electrons in p_z -orbitals interact creating delocalized π -cloud over the entire graphene layer⁶². As a result, π -bond is formed by p_z -orbitals, and σ -bond is created by $2s$, $2p_x$, and $2p_y$ orbitals⁵³. Fig. 3.6 exhibits the formation of sp^2 hybridization for graphene.

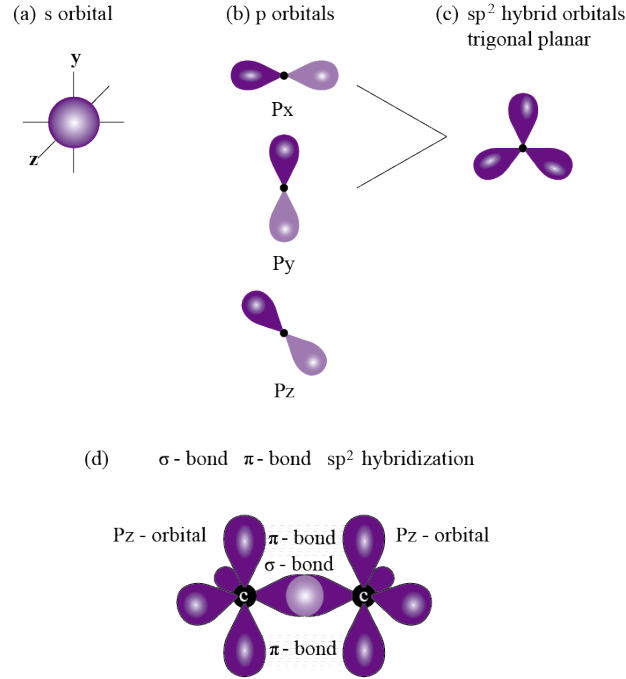


Figure 3.6: (a) Hybridization of s orbital. (b) Hybridization of p_x , p_y , p_z orbitals. (c) Hybridization of sp^2 orbital formed by s, p_x , and p_y orbitals. (d) σ bond and π bond formed by sp^2 hybridization in graphene structure.

Graphene has a honeycomb lattice that expands its layers only in x -, y -plane. Additionally, in z -plane graphene layers are stacked to form bilayer and multi-layer⁶². The crystal structure of graphene has two atoms in its unit cell to form a hexagonal lattice of monolayer graphene, illustrated in Fig. 3.7. Those are represented as primitive lattice vectors a_1 and a_2 chosen to be⁶³:

$$\vec{a}_1 = \frac{a}{2} (\sqrt{3}, 1), \vec{a}_2 = \frac{a}{2} (\sqrt{3}, -1), \quad (3.1)$$

where $C-C$ atoms distance is $a = 1.42\text{\AA}$ and the lattice constant is $|a_1| = |a_2| = 2.46\text{\AA}$, which represents the distance between unit cells⁶³.

Similarly, the reciprocal lattice vectors represented by b_1 and b_2 as shown in Fig. 3.7 are rotated 30° with respect to \vec{a}_1 and \vec{a}_2 . Those are given by⁶³:

$$\vec{b}_1 = \frac{2\pi}{a} \left(\frac{1}{\sqrt{3}}, 1 \right), \vec{b}_2 = \frac{2\pi}{a} \left(\frac{1}{\sqrt{3}}, -1 \right), \quad (3.2)$$

where the lattice constant in the reciprocal space is $\frac{4\pi}{\sqrt{3}a}$ ⁶³.

In order to make multi-layer graphene, Van der Waals bonding occurs between sheets creating a lattice spacing of $c = 6.71 \text{ \AA}$. Primitive and reciprocal lattice vectors for multi-layer graphene are given by \vec{a}_3 and \vec{b}_3 respectively⁶⁴.

$$\vec{a}_3 = c(0, 0, 1), \vec{b}_3 = \frac{2\pi}{c}(0, 0, 1), \quad (3.3)$$

where the intersection of $k_z = \frac{2\pi}{c}$ forms a hexagonal prism of height $\pm \frac{4\pi}{c}$ ⁶⁴ as represented in Fig. 3.7.

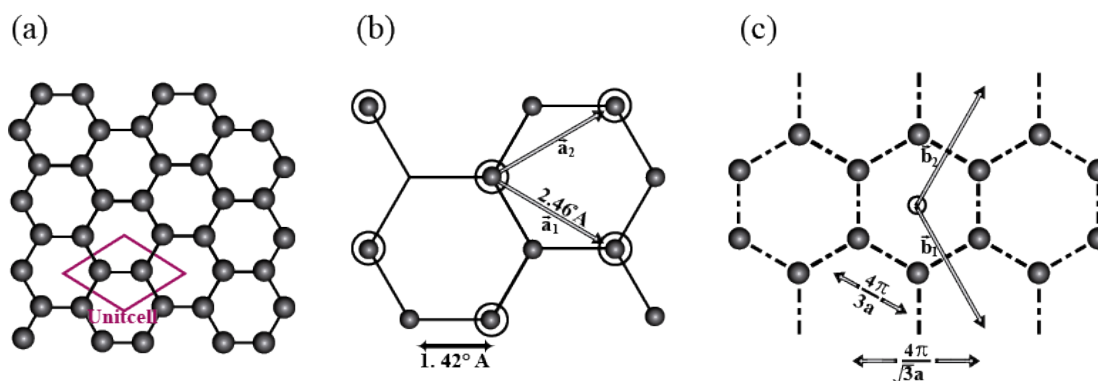


Figure 3.7: (a) Honeycomb lattice of graphene and unit cell which allows the formation of graphene monolayer. (b) Representation of c-c atoms distance, lattice constant, and primitive lattice vectors in the graphene crystal structure. (c) Reciprocal lattice of graphene highlighting the reciprocal unit vectors and reciprocal lattice constant.

3.2.5 Graphene Oxide (GO)

Graphene oxide involves the oxygenated two-dimensional structure of graphite. It was first synthesized in 1859 by Sir Benjamin Collin Brodie and studied one century after by Lerf and Klinowsky⁶⁵. GO is a non-stoichiometric carbon material generated by introducing oxygen functional groups such as carbonyl, hydroxyl, epoxy, phenol, or impurities of Sulphur in the hexagonal lattice of graphene layers^{66,67}. The specific structural features for oxidized graphene have not yet been fully developed, therefore several models have been presented to eliminate ambiguity around its chemical structure⁶⁸, which are shown in Fig. 3.8.

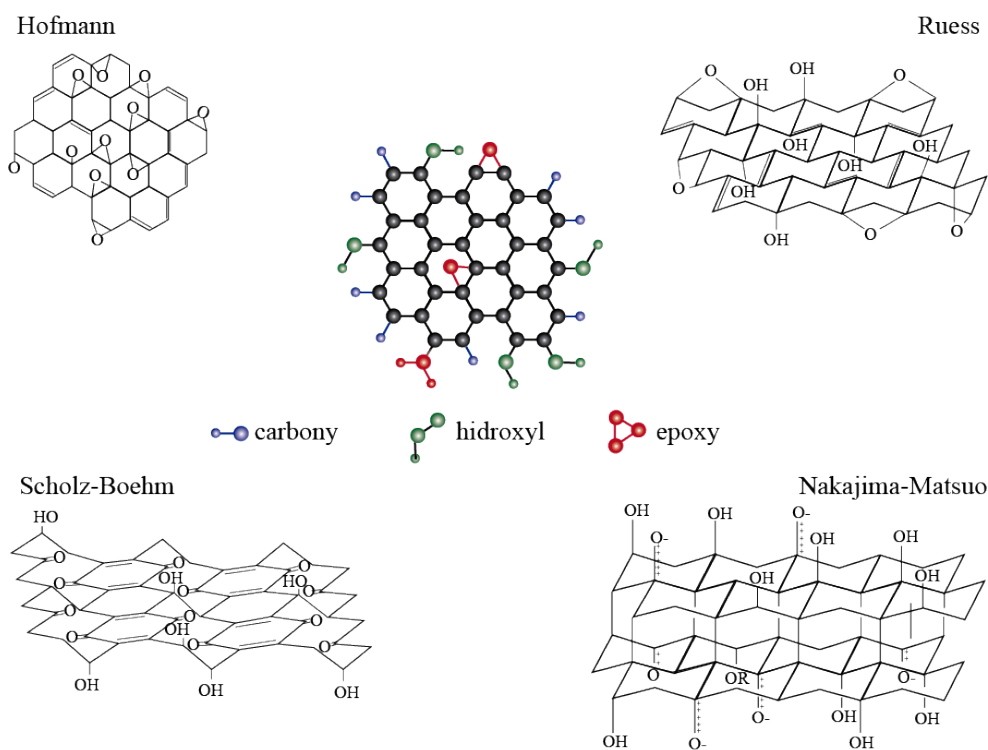


Figure 3.8: Illustration of graphene oxide with carbonyl, hydroxyl, and epoxy functional groups and some proposed structure models such as Hofmann, Ruess, Scholz-Boehm, and Nakajima-Matsuo.

Graphene oxide can be synthesized from low-cost graphite and using cost-effective synthesis methods such as dip coating, spray coating, spin coating, or Hummer's technique, making GO attractive for high-performance industrial applications⁶⁵. Furthermore, it is highly hydrophilic so it is capable of forming stable colloids in aqueous media to facilitate the assembly of macroscopic structures⁶⁹. The commercial and industrial applications of GO are reflected in electronics devices, energy storage devices, biosensors, biomedical fields, water purification, coating technology, and nanocomposites. The advances are expanding rapidly due to new processes developed that combine oxidized graphene with other nanomaterials to improve existing mechanisms⁶⁹.

3.2.6 Nanocomposites

Nanocomposites are the result of the combination of two or more materials comprised to blend, achieve and accomplish the best properties of each one⁷⁰. To be considered nanocomposites, at least one phase of materials must demonstrate dimensions at nanoscale⁷¹. The main property of nanocomposites is their ability to assemble characteristics of components of different natures to create a new material with better features than it has on its own⁷⁰. Thence, they provide a huge range of applications in electronics, optical communications, drug delivery,

fibers and films, UV protection, anti-corrosion coatings, chemical sensing, among others^{72 70}.

The classification of nanocomposites is based on two aspects: (i) according to their matrix materials and (ii) depending on their engineering applications^{73 70}.

According to the matrix materials, nanocomposites are classified as⁷³:

- 1 Ceramic-based nanocomposites
- 2 Metal-based nanocomposites
- 3 Polymer-based nanocomposites
- 4 Carbon-based nanocomposites

The matrix of ceramic-based nanocomposites is mainly conformed by Al_2O_3 and SiC ⁷³. They have extraordinary electrical and mechanical properties for which they can be applied in various fields, mainly in biomedicine due to their biocompatibility, chemical stability, and high wear resistance⁷⁴. Ceramic-based nanocomposites are fabricated using powder method, polymer precursor route, spray pyrolysis, sol-gel process, colloidal and precipitation approaches, and template synthesis⁷⁵. Some common examples are Al_2O_3/SiO_2 , SiO_2/Ni , Al_2O_3/TiO_2 , Al_2O_3/CNT ⁷¹.

Metal-based nanocomposites consist of a metal matrix with a nanoscale reinforcement material⁷⁵. They show extraordinary features, i.e., tensile and compressive behavior, ductility, toughness with high strength and modulus, high-temperature mechanical properties, wear resistance, creep, damping, and dry/wet corrosion resistance⁷⁶. The main fabrication methods used for the synthesis of metal-based nanocomposites are coprecipitation, sol-gel, hydrothermal, stir casting, disintegrated melt deposition (DMD), powder metallurgy (PM), friction stir processing among others^{76 77}.

Polymer-based nanocomposites use one-, two- and three-dimensional nanoadditives as reinforcement materials and the main matrix component is a polymer. They exhibit a set of exceptional properties such as high strength and elastic stiffness with small additives concentrations, barrier resistance, flame retardancy, wear resistance, magnetic, electrical, and optical properties. As well, lightweight, high durability, easy processing, corrosion resistance, ductility, and low cost. The properties in polymer nanocomposites depend on: (i) process of fabrication, (ii) type of adhesion at the matrix, (iii) nanoparticle characteristics, (iv) morphology of the system, (v) degree of mixing of two phases, and (vi) type of polymer used, these can be; thermoplastics, thermosets, elastomers, natural and biodegradable⁷⁵.

Carbon-based nanocomposites are fully carbon matrix materials such as activated carbon, graphene, carbon dots, graphene oxide, carbon nanotubes, and carbon aerogels²⁶. Although they are made mostly of carbon materials, these nanocomposites reach their maximum efficacy with polymers and metallic nanoparticles^{26 27}. Therefore, the range of applications is extensive, as it is used in electrochemical power sources, food packaging, solar cells, electric vehicles, nanoelectronic devices, chemical sensors, supercapacitors, and biosensors^{27 70 26}. The production methods used to synthesized carbon-based nanocomposites are sonication, stirrer, calendaring, melt processing, and in situ polymerization⁷⁸. Depending on their engineering applications, nanocomposites are classified as functional materials and structural materials⁷⁰.

In engineering, nanocomposites are used in different fields according to the properties they have. Functional materials are mainly focused on the electrical, magnetic, and optical behavior of nanocomposites, as well as structural materials, are based mainly on their mechanical properties. The features of nanocomposites are controlled by aspects already introduced⁷⁰.

To generate the effective blend of the material to create a nanocomposite is necessary to enhance its adhesion properties. Therefore some components are added to accomplish this function, specially polymers. In this work polyvinyl alcohol (PVA) is used due to its properties such as: non-toxicity, water solubility, bio-compatibility, environmental friendly, and high adhesion properties because PVA exhibit a large flexible chain having a high concentration of polar groups which contributes to its exceptional characteristics^{79 80}.

3.2.7 Photochemical Synthesis Method

Photochemical synthesis is a novel route to obtain anisotropic metallic nanoparticles. This method implements light radiation to reduce metallic atoms into their metallic state by performing processes of nucleation and growth concurrently⁸¹. This mechanism is based on a seed-mediated growth which allows controlling the reduction of metal ions without using a reducing excess agent. Furthermore, radiation absorption is independent of light-absorbing solutions and products. Additionally, the rate of reactions is well-defined because the reduction reaction is uniformly performed in the entire solution⁸². Nanoparticle formation and growth processes through photochemical synthesis are complex due to the number of variables that control their properties. The size and shape of metallic nanoparticles produced depend mainly on the pH, temperature, and irradiation time, as well as, the precursors and surfactants used for the process⁸¹. As a result of the synthesis, nanostructures with different shapes are generated depending on the change in the variables and precursors used. Nanoprisms, pentagons, hexagons, and other random shapes have been reported, which have potential applications in specific fields^{81 83 21}. The illustration of the photochemical synthesis method is shown in Figure. 3.9.

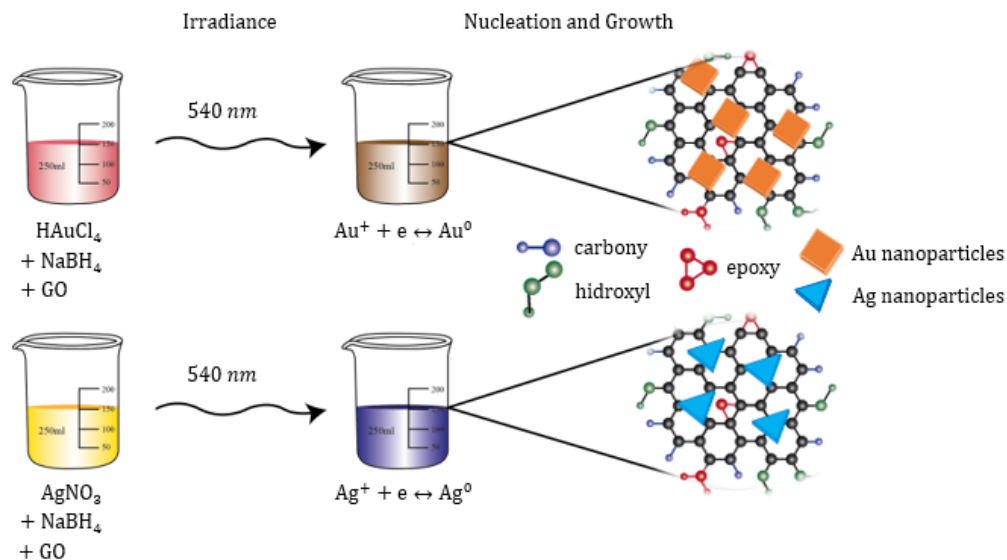


Figure 3.9: Illustration of photochemical synthesis method.

3.3 Sensors

Similar to the human senses, sensors are devices capable of receiving and processing information⁸⁴. The invention of the first thermostat by Warren S. Johnson is considered the beginning of sensor technology, subsequently, countless increasingly sophisticated sensing devices have been worked on⁸⁵. A sensor is an input device that converts physical measures into an electrical signal that can be easily read or observed by an instrument⁸⁵.

The classification of sensors is extensive and considers many parameters such as, the area of detection, physical law, specification, application, power requirement, output signal, stimulus, and type of transducer, which can vary widely. Each type of sensor provides different degrees of accuracy, sensitivity, resolution, linearity, drift, specificity, and ability to operate in other environmental conditions⁸⁵. This research work focuses on electrochemical sensing.

3.3.1 Electrochemical Sensors

One of the most widely applied detection devices in the industry is electrochemical sensors because of their low cost, accessible employment, portability, and straightforward making¹⁸. They are classified in the sensor subgroup of chemical sensors⁸⁶. The main disadvantage of electrochemical sensors is the deficiency of architectures causing a low signal-to-noise ratio. This behavior in the sensor reduces the sensitivity and identification of the response. Nevertheless, to solve that need, the implementation of nanotechnology has been emphasized in the principles of electrochemical sensors, which allows increasing the sensitivity at the device interface¹⁹.

Based on their detection mode, they can implement potentiometric, amperometric, voltammetric, and impedimetric transducers which convert chemical information into different types of measurable signal^{87,88}.

Potentiometric sensors

A potentiometric sensor is a device that provides information about the ion activity inside an electrochemical cell. It measures the accumulation of a charge potential at the working electrode compared to the reference electrode when the current is close to zero¹⁹. The cell potential is determined by the Nernst equation which relates the electrode potential signal logarithmically proportional to the ion activity of redox species consumed in the recognition process⁸⁹:

$$E_{cell} = E_{cell}^0 + \frac{RT}{nF} \ln Q \quad (3.4)$$

Where E is the observed cell potential at close zero currents, E^0 is the standard potential, R is the universal gas constant, T is the absolute temperature in Kelvin, n is the charge number of moles of electrons exchanged, F is the Faraday constant, and Q is called the reaction quotient, which contains the activities of oxidized and reduced redox species in the cell^{89,19}.

Potentiometric devices exhibit three types:

- *Ion-selective electrodes (IES)* are measure electrodes capable to respond to the activity of a specific ionic species in a mixture. They are membrane-based sensors based on semipermeable ion-conducting materials. The main example of IES is the glass pH electrode because it has a high selectivity for hydrogen ions^{90,91}.
- *Coated wire electrodes (CWES)* are conductors coated with an ion-selective polymer membrane to generate electrodes with a high sensibility to changes in electrolyte concentrations⁹⁰.
- *Field-effect transistors (FETS)* are multi-sensing devices that consist of an ion-selective membrane integrated on a field-effect transistor to detect ions of different types simultaneously⁹⁰.

Amperometric and Voltammetric Sensors

Amperometric sensors are based on the measurement of changes in the current generated during electrochemical oxidation and reduction processes¹⁸. The applied potential remains constant at the working electrode regarding the reference electrode⁸⁸. Meanwhile, voltammetric sensors produce current measurements using a potential difference scan from one defined value to another⁹⁰. In both cases, the working feature is based on the electron-transfer reaction which generates measures of current directly associated with the concentration of electroactive species and its reaction rate. The selection of the electrode material is essential for obtaining reliable results for amperometry and voltammetry^{90,86}.

The implementation of novel nanocomposites has allowed the easy miniaturization of electrochemical sensing electrodes to develop systems with higher chemical selectivity, activity, detectability, and stability allowing to achieve dimensions in the order of micrometers and nanometers^{89,18,90}. Chemically modified electrodes (CME) are fabricated by immobilization of micro and nanostructures on the electrode surface using a method such as, chemical reactions, chemisorption, composite formation, or polymer coating⁹⁰.

Chapter 4

Characterization techniques

4.1 Spectroscopy Techniques

4.1.1 Ultraviolet-Visible Spectroscopy (UV-Vis)

UV-Vis spectroscopy is a characterization technique used to record the absorption of radiations in ultraviolet and visible range⁹². In the electromagnetic spectrum, ultraviolet includes wavelengths from 10 *nm* to 400 *nm*, and visible is in the region from 400 *nm* to 800 *nm*. Absorption of light energy occurs when light passes through an analyte sample, exciting electrons from the ground state to the excited state of the material called electronic transitions.⁹³ During the electronic transition process, light is absorbed by molecules to promote electrons toward higher energy levels, which according to the amount of analyte in the sample will generate a decrease in the intensity of incident light⁹⁴.

The spectrophotometer uses information about the transition to generating a plot of wavelengths of absorbed radiations versus optical density or absorbance which is defined perfectly by Lambert-Beer Law⁹². Lambert-Beer Law describes the behavior of light intensity when crossing through a thin slice containing an absorbing sample, it is expressed by the following equation.

$$\log_{10} \frac{I_0}{I} = A = \epsilon cl \quad (4.1)$$

Where I_0 represents the intensity of incident radiation, I is the intensity of radiation after passing the sample solution, A is called the absorbance, ϵ is the molar extinction coefficient, which measures the probability of an electronic transition occurs in a molecule in presence of light, it is constant for each wavelength, c is the concentration of solute and is given in $\frac{\text{mol}}{\text{L}}$, and l represents the path length of the sample given in cm. According to equation 4.1, the absorption of incident radiation made by a sample solution is proportional to the number of absorbed molecules^{92,94}.

Instrumentation

UV-Vis spectroscopy is based on the interaction between light and matter. Although there are different spectrophotometers of this type, with components more sophisticated than others, they all maintain the same five essential elements, those are: (i) A well build *radiation source*, which generates broadband electromagnetic radiation. (ii) A *wavelength selector* of different types, sizes, and shapes. It allows selecting a specific wavelength from the broadband generated by the source. (iii) A *sample holder*, which determines the area where the sample is going to be fixed. (iv) A *transducer* that allows detecting the intensity of radiation that is generated after passing the absorbed sample. (v) A *signal processing*, which converts the detected information into an absorbance spectrum^{94,94}. According to the number of radiation sources, two types of UV-Vis spectrophotometers can be identified.

- *Single-Beam UV-Vis spectrophotometer*: It uses a single light beam and a single sample holder. Therefore, the machine is calibrated using a reference or standard solution before measuring the sample, to subtract the effects produced by the solvent⁹⁴.
- *Double Beam UV-Vis spectrophotometer*: In this type, two light beams and two sample holders are used to measure the standard solution and sample at the same time, to generate better precision in the measurements⁹⁴. A schematic representation of this type is shown in Fig. 4.1.

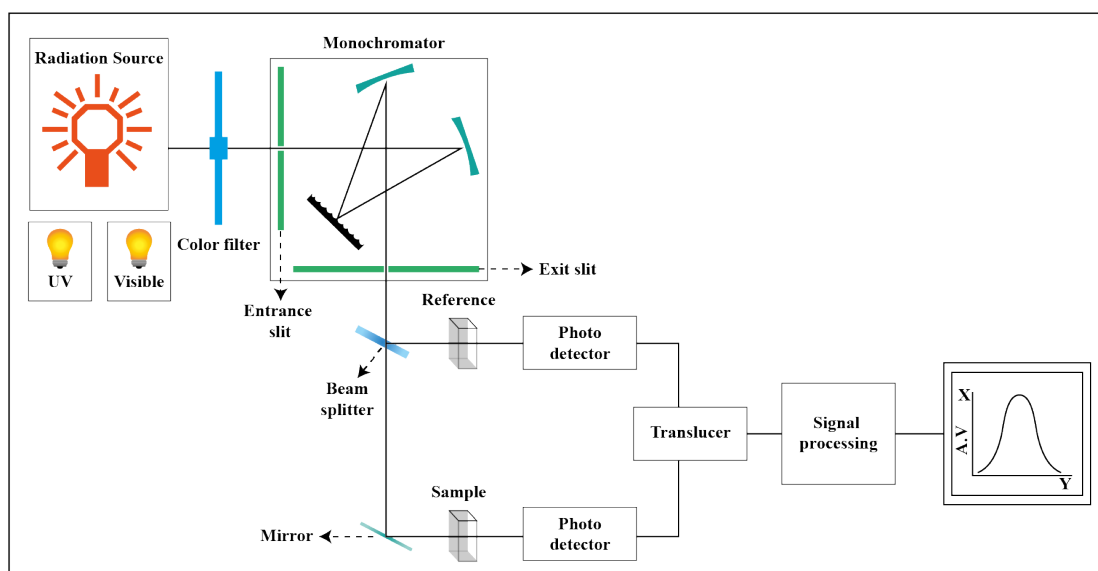


Figure 4.1: Schematic representation of a Double Beam UV-Vis spectrophotometer.

4.1.2 Fourier-Transform Infrared spectroscopy (FT-IR)

Fourier-Transform Infrared Spectroscopy is a high sensitivity analytical technique used to study the interaction between infrared radiation and molecular rotations to determine the chemical composition of molecular compounds⁹⁵. Infrared spectroscopy uses modulated IR radiation to change the dipole moment of IR active molecules. The interaction between the sample and the infrared light generates the atom-to-atom vibrations due to an absorption process. Different bonds in molecules oscillate at different energies absorbing different wavelengths. FT-IR spectrometer can measure the frequency of vibrations and the intensity of individual absorption bands to generate an absorbance-transmittance vs wavenumber (cm^{-1}) spectra over the range of 4000-600 cm^{-1} as a fingerprint because it is unique to a molecule⁹⁶.

The absorption process in FT-IR happens only for the frequencies of the bonds that match the radiation frequencies, therefore, different modes of vibration are generated depending on the molecule. The simplest vibration modes in IR are stretching and bending vibrations⁹⁷.

- **Stretching Vibration:** It is generated for molecules that contain at least two or three identical groups. It could be symmetric and asymmetric, having asymmetric stretch higher energy than symmetric⁹⁷.
- **Bending Vibration:** It generates changes in the bond length maintaining its angle. It could be in-plane or out of plane⁹⁷.

Instrumentation

The main components of FTIR spectrometers are: (i) light source, (ii) interferometer, (iii) sample compartment, (iv) detector, (v) amplifier, and (vi) computer⁹⁸. The *light source* generates energy in radiation form to reach the sample and take the information to the detector, the *interferometer* which translates the information with extraordinary accuracy based on interferometry theory, the *sample compartment* maintains the sample in the proper measurement conditions, a *detector*, *amplifier*, and *computer* which generates the spectra to be studied easily⁹⁷. The internal configuration scheme of FTIR is given in Fig. 4.2

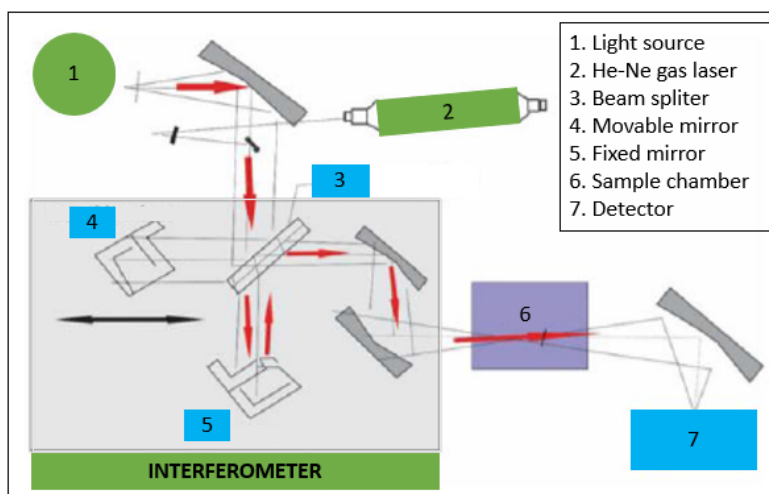


Figure 4.2: Schematic representation of an FTIR spectrophotometer. Adapted from Khan⁹⁷.

4.1.3 Raman spectroscopy

Raman spectroscopy is a scattering technique used to determine the vibrational motions of molecules through measurements of inelastic scattering of light⁹⁹. This characterization technique follows the Raman effect detected by Sir Chandrasekhra Venkata Raman and Kariamanikkam Srinivasa Krishnan in 1928 who observed that photons reaching a sample are inelastically scattered when interacts with different vibration modes of molecules contained in sample^{100 101}. Raman phenomenon can be explained using concepts of classical physics and with quantum-mechanical theory to have a better understanding, both consider the effect of a dipole moment determined by polarizability of the molecule¹⁰². According to quantum mechanics, when a photon excites an electron it immediately recombines emitting a photon of different energy, but energy and momentum must be conserved, therefore the existence of a quasi-particle must be considered, in this way a transition is generated from an initial to final energy level via an intermediate called virtual state⁹⁹.

Schematic observations exhibit that vibrational and rotational states of molecules are excited from low energy levels to virtual states because they do not have enough energy to reach an electronically excited state. After getting a virtual state, a decay to lower energy states is observed generating different types of scattering¹⁰³:

- *Rayleigh scattering*: The molecule returns just to the initial state¹⁰⁰.

$$h\nu_{0r} = h\nu_0 \quad (4.2)$$

- *Stokes scattering*: The molecule decays to a higher state than the initial¹⁰⁰.

$$h\nu_{0s} = h\nu_0 - h\nu_k \quad (4.3)$$

- *Anti-Stokes scattering*: The molecule decays to a lower state than the initial ¹⁰⁰.

$$h\nu_{0a} = h\nu_0 + h\nu_k \quad (4.4)$$

Rayleigh, stokes, and anti-stokes scattering are schematically represented in Fig. 4.3.

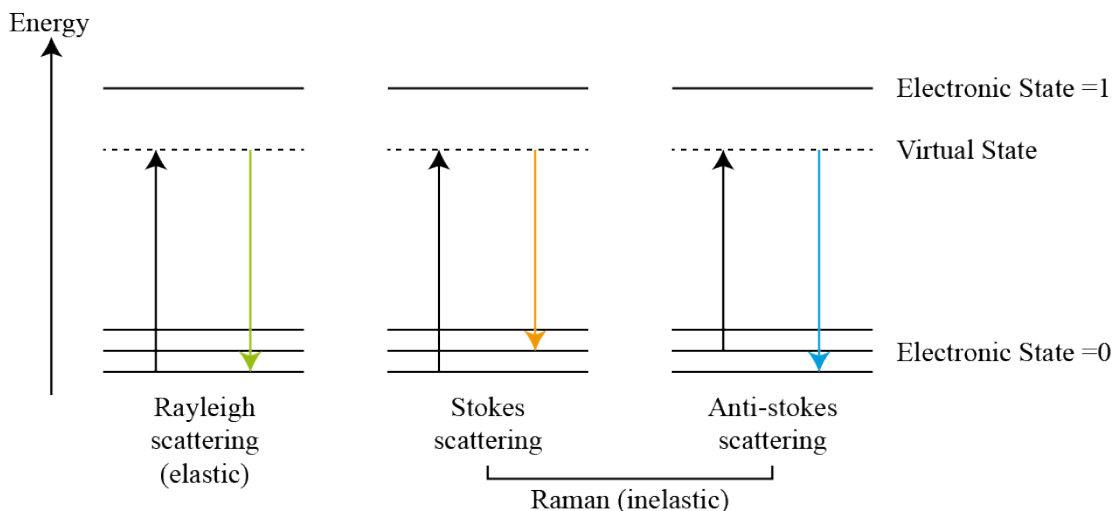


Figure 4.3: Energy diagrams of Stokes, Rayleigh, and anti-Stokes Raman scattering. Vibrational modes of molecules are excited from low energy levels to reach virtual states and finally decay to lower energy states.

Instrumentation

The main components of any Raman spectrophotometer are four: (i) The *excitation source* which must be very intense and as monochromatic as possible to observe clear and narrow bands in the final Raman spectrum¹⁰⁰. Solid-state lasers of specific wavelengths of 532 nm, 785 nm, 830 nm y 1064 nm are used in Raman spectroscopy⁹⁹. (ii) The *sample illumination* must follow a specific geometry depending on the nature of the sample. The incident excitation source can accomplish a specific optical configuration, for liquids must be at 90°, and for solids at 180° to collect efficiently the scattered radiation. (iii) A *wavelength selector* allows to eliminating any unwanted signal, in Raman spectroscopy the primary signal to remove comes from Rayleigh scattering. Interference filters, prisms and grating monochromators can be used to reduce noise in the signal recorded by the detector of the equipment¹⁰². (iv) The *processing system* is mainly formed by a detector which helps to collect the electron pulses generated by the system to then be amplified and converted into an image known as the Raman spectrum¹⁰². The internal configuration of the Raman spectrophotometer is observed in Fig. 4.4.

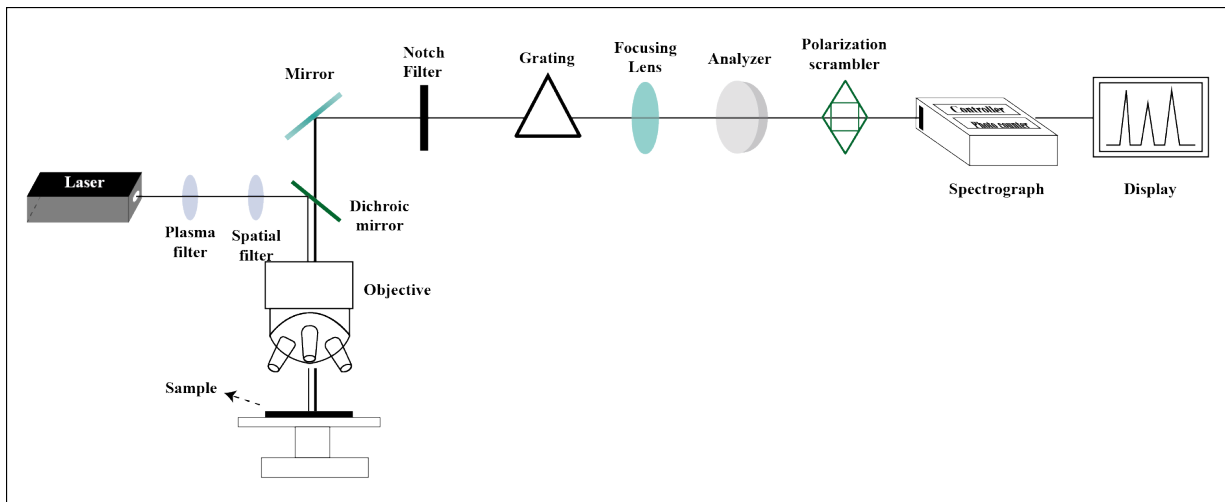


Figure 4.4: Schematic diagram of Raman spectroscopy system, components and configuration.

4.2 Microscopy techniques

4.2.1 Scanning Electron Microscopy (SEM)

SEM is a characterization technique used to analyze the morphology, crystalline structure, orientation of materials, and chemical composition of nano and micro-scaled solids¹⁰⁴. SEM is based on the research works of Ruska and Knoll who created the transmission electron microscope around the thirteenth of the last century. It was studied and improved by many scientists throughout the years until 1965 when SEM was available to the public, even today this technique continues to evolve its operating principle¹⁰⁵. The working principle of SEM begins when the primary electron beam interacts with the atoms in the specimen to produce information mainly about the topography of the sample and to be transformed into an image¹⁰⁶. The interactions generated during the acquisition process are elastic and inelastic. Elastic scattering is formed by the deflection of the incident electrons due to the specimen. Electrons that are elastically scattered through an angle higher than 90 degrees are called backscattered electrons (BSE)¹⁰⁴. SEM works similarly that TEM, first the electron beam is produced by tungsten wire in the electron gun. Second, the electron beam goes through the electric field and lenses in the vacuum column. Third, an electron beam is guided to hit the surface of the sample generating secondary electrons, auger electrons, backscattered electrons, X-rays, and cathodoluminescence as signals which are enveloped by electrical detectors to be converted into digital images¹⁰⁶.

Instrumentation

Instrumentation of SEM consists mainly of:

- **Electron column:** Where the traveling of electron beam under vacuum conditions is generated, to reach a specific point of the sample by electromagnetic deflection coils¹⁰⁶.
- **Electron gun:** It is a source that generates electrons of high energy¹⁰⁵.
- **Condenser Lenses:** Cause the convergence of the beam to focus it into the sample¹⁰⁶.
- **Apertures:** Reduce and eliminate the extra electrons reaching the sample to have better resolution¹⁰⁴.
- **Specimen Chamber:** Control the stage specimen stage to have better conditions to perform the measurements¹⁰⁶.
- **Electron Detectors:** Collect the signal generated during the interaction electron beam-specimen¹⁰⁶.

Scanning Electron Microscopy instrumentation is shown in Figure 4.5.

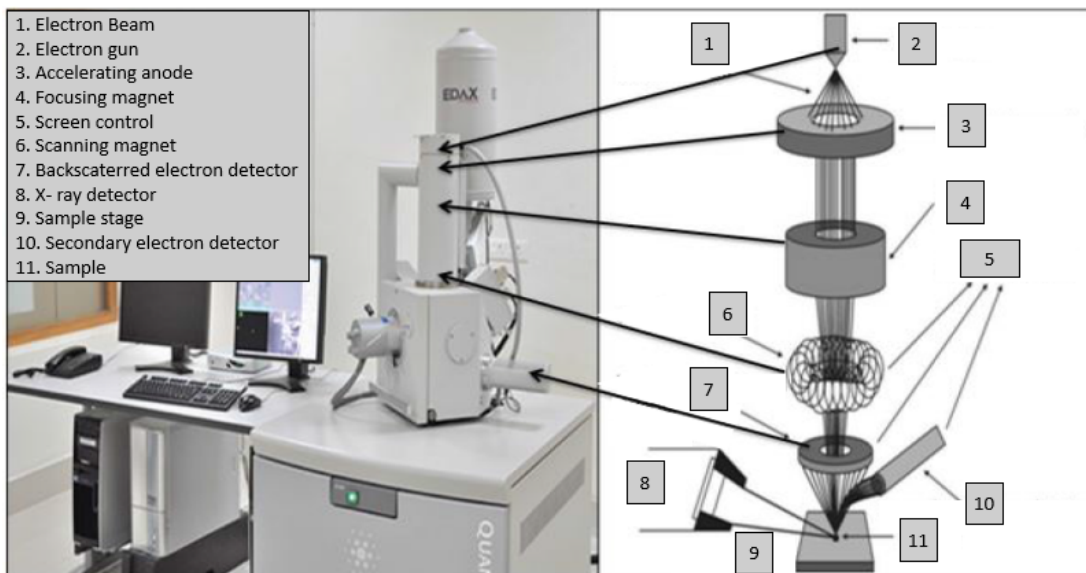


Figure 4.5: Image of SEM microscope and components of the electron column. Adapted from Kannan¹⁰⁶.

4.2.2 Atomic Force Microscopy (AFM)

Atomic force microscopy is a powerful characterization technique used to study the structure and surface properties of nanomaterials. AFM maps the topography of the sample using a cantilever containing a probing tip. AFM was created by Gerd Binnig, Calvin F. Quate, and Christoph Gerber in 1986 to solve the limitations of scanning tunneling microscopy (STM). Consequently, AFM allows investigating conductive and non-conductive materials, becoming a forerunner of the STM technique¹⁰⁷. AFM performs measurement recording the forces generated by the interaction

of a sharp probe and the surface of the sample¹⁰⁸. Therefore, AFM imaging allows obtaining images with an atomic resolution of 10^{-10} meters¹⁰⁹.

Atomic force microscopy constructs a three-dimensional image using a cantilever which behaves as a force sensor. To perform the measurements, the sample is placed on a piezoelectric scanning allowing to move it in X and Y directions¹⁰⁹. In one end of the cantilever a probe is attached and a laser is focused on the other free end. The cantilever and the probe act as a spring, generating deflections when they interact with the sample. The deflections are detected by a position-sensitive detector through changes in the direction of the laser-focused in the cantilever¹⁰⁸.

In AFM, two main working modes can be distinguished, the contact mode and the dynamic model.

- **Contact mode:** In contact mode, the cantilever is configured to generate a direct contact between the sample and the probe. It means that the force inserted is very high, which generates some friction forces in the surface of the sample¹⁰⁷. This mode is not recommended for measuring soft materials, because it could damage the sample surface and could break or pull off the probe from the cantilever. Materials with hard surfaces can be studied with high resolution using the contact mode¹¹⁰.
- **Dynamic mode:** In dynamic mode, AFM measures changes in the amplitude and frequency of cantilever caused by attractive and repulsive forces. The forces depend on the interaction of the tip and the sample generating information about its topography¹⁰⁷. Dynamic mode is divided into two types according to the amplitude and frequency used for the measurements.
 - *Non-contact mode:* It uses an amplitude of 1-10 nm and a cantilever oscillating at a frequency of 100kHz. Soft samples can be imaging with non-contact method because very feeble interaction forces are generated avoiding the damage of the sample surface¹¹¹.
 - *Tapping mode:* In this mode the cantilever is vibrating near its resonance frequency and the amplitude is in the order of 20-200 nm. Tapping mode allows intermittent sample-probe contact due to low forces applied. It is also appropriate to measure soft samples¹⁰⁹.

Instrumentation

AFM principle is determined by the measurements in sample-probe interaction forces. Therefore, to achieve an atomic resolution, five components are incorporated into atomic force microscopy instrumentation. Those components are: (i) The *tip and cantilever* which are considered the most important components of AFM because they are located close to the sample to interacts directly generating qualitative information about interaction forces¹¹¹. (ii) A *laser source* is used to detects the deflections in the cantilever caused by attractive and repulsive forces generated by sample-probe interactions¹⁰⁷. (iii) *The detector* is used to monitor and record the changes in the position of the laser source caused by deviations in the cantilever. A high-resolution deflection detector is commonly used to magnify the motion signals¹¹¹. (iv) The *piezoelectric scanner* controls the movements between the probe and the sample, providing precise information about vertical displacement of the scanner and cantilever deflections¹⁰⁸. Piezoelectric allows AFM to record three-dimensional images of the surface topography of the sample¹⁰⁷. The schematic diagram of the experimental set-up used in AFM is observed in Fig. 5.8.

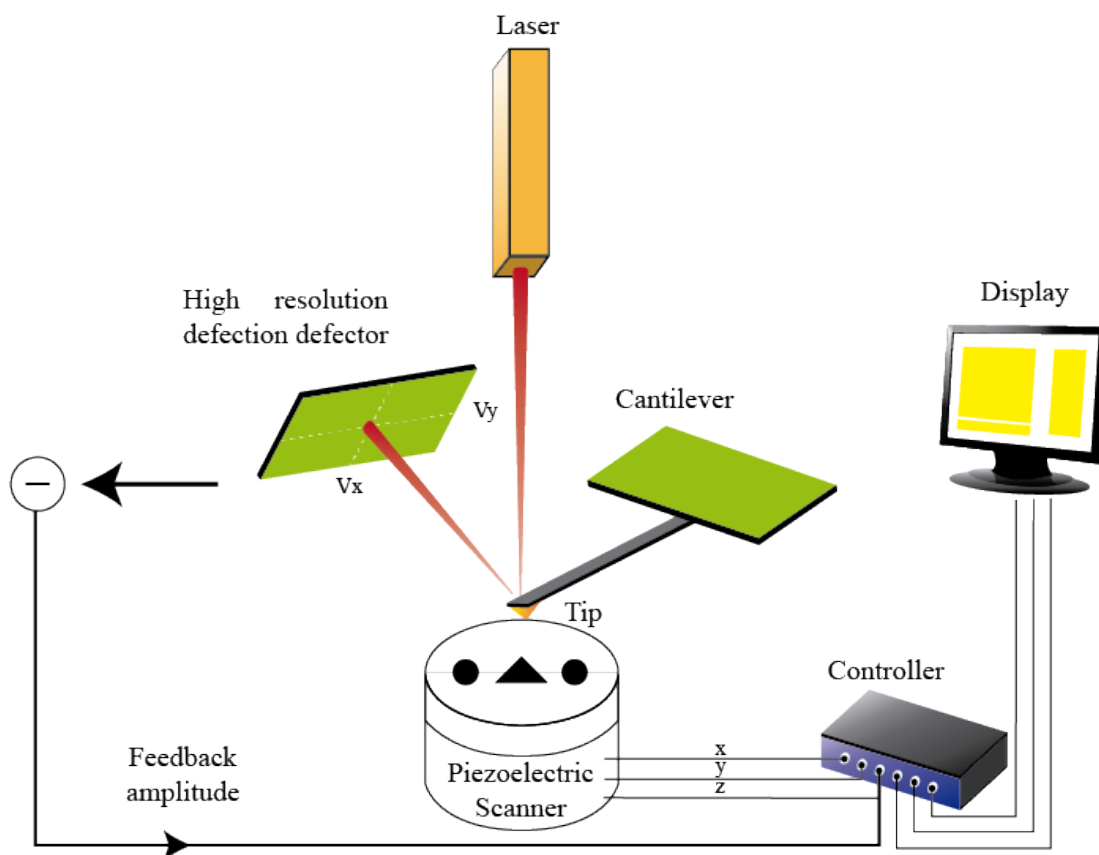


Figure 4.6: Schematic illustration of AFM general working principle.

4.3 Electrochemical Techniques

Electrochemical techniques are based on electrochemistry principles to study a system's redox response to an electrical (voltage or current) stimulus. Reduction and oxidation reactions are studied to provide information about the concentration, kinetics, reaction mechanism, and chemical behavior of the species contained in an electrolyte solution¹¹².

4.3.1 Cyclic Voltammetry (CV)

Cyclic Voltammetry has become one of the fundamental electrochemical techniques for the study of molecular species through observations of peak current, peak potential, and different shapes of voltammograms which are specific for each redox system¹¹³. CV uses the electronic instrumentation of potentiostat as an external power source. The potentiostat device applies a swept voltage between the working electrode and the reference electrode to

obtain the measurement of current between the working electrode and counter electrode¹¹⁴, observed in Fig. 4.7 (a). During cyclic voltammetry, the potential of the working electrode changes following a triangular waveform shows in Fig. 4.7 (b). The potential is swept initially from E_1 to E_2 represented as A and D points, in D the potential is switched to reach the end in E_1 identified as G ¹¹⁵.

Cyclic voltammetry measurements result in a current-potential curve called a cyclic voltammogram similar to the profile shown in Fig. 4.7 (c). In a cyclic voltammogram, the x-axis represents the potential applied by the potentiostat, and the y-axis shows the current corresponding to each potential value¹¹⁴.

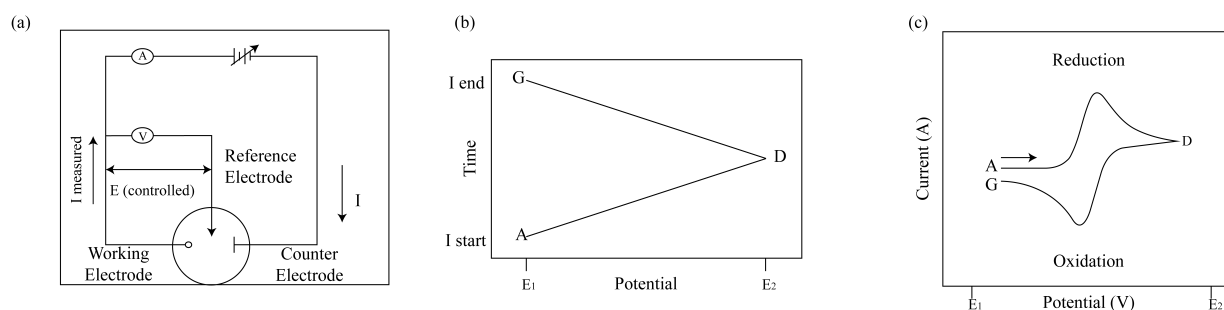


Figure 4.7: Important features of cyclic voltammetry: (a) Simplified circuit used in the set-up of cyclic voltammetry. (b) Triangular potential waveform produced by a forward and backward scan of cyclic voltammetry. (c) Cyclic voltammogram.

Cyclic voltammetry methods exhibit three types of reactions due to the electron transfer kinetics between the analyte and electrode of any kind¹¹⁵. They are reversible, semi-reversible, and irreversible processes. These are described in Table 4.1.

Reaction	Description
Reversible	Low barrier to electron transfer and fast electrode kinetics ¹¹⁵ .
Quasi reversible	Limited electron transfer kinetics ¹¹⁶ .
Irreversible	High barrier to electron transfer and very sluggish transfer kinetics. ¹¹⁵

Table 4.1: Types of reversibility and electrochemical kinetics of different reactions.

Cell Components

The main components used to generate cyclic voltammograms are, an electrochemical cell as observed in Fig. 4.8, a potentiostat device or an external voltage source, and an electrochemical software employed to translate signal

generated by cyclic voltammetry into cyclic voltammograms¹¹³.

The experimental setup required to achieve electrochemical measurements is composed of three elements: (i) An electrochemical cell, (ii) an electrolyte, and (iii) a set of electrodes¹¹⁵. The electrochemical cell is an inert vessel where the experiments are made. In this structure, all the components are encapsulated to generate the chemical reactions necessary for sensing¹¹⁵. Electrolyte solutions facilitate the cell reaction maintaining the migration of ions across the electrodes efficiently. The electrolyte allows ions to move in solution to compensate the charge and close the electrical circuit of the sensor. A suitable electrolyte is a mixture of a solvent and a supporting electrolyte. The electrolyte must be stable toward oxidation and reduction processes and purified within the electrochemical window. The supporting electrolyte must be highly soluble in the solvent, chemically and electrochemically inert, and also purified¹¹⁵.

The electrochemical cell uses a *reference electrode*, a *counter or auxiliary electrode*, and a *working electrode*. An external voltage is required to provide a stable potential signal to drive the specific reaction for the sensing process¹⁹. The *Reference electrode* is a high stability electrode that maintains stable and well-defined potential in the electrochemical cell to control and measure it. The current flow through the reference electrode is close to zero. The exact value depends on the material from which the electrode is made. Commonly used reference electrodes are standard hydrogen electrode (SHE), silver chloride electrode, copper/copper sulfate electrode, mercury/mercurous chloride (calomel) electrode, among others¹¹⁷. A *Counter or auxiliary electrode* is made of inert material. It is used to close the current circuit in the electrochemical cell because it does not interfere with the reactions. The *Working electrode* is where the electrochemical reactions occur that are under study. The electrode can be modified to facilitate specific reactions or improve sensibility¹¹⁸.

The setup of the electrochemical cell used in this study is illustrated in Fig. 4.8.

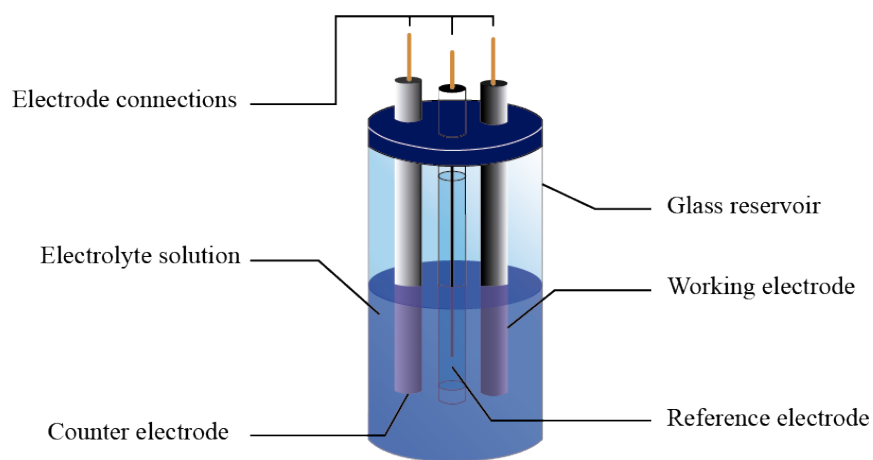


Figure 4.8: Experimental setup of an electrochemical cell. It is composed of three electrodes fixed inside a glass reservoir and immersed in an electrolyte solution connected to the potentiostat. Adapted from Kosala Wijeratne¹¹⁹.

Chapter 5

Methodology

5.1 Chemicals

Silver nitrate $AgNO_3$ 99%, sodium borohydride ($NaBH_4$) 98%, polyvinyl alcohol (*PVA*) average Mw 85,000 - 124,000, 87-89% hydrolyzed, and gold chloride ($HAuCl_4$) 99% were purchased from Sigma Aldrich. Trisodium citrate ($Na_3C_6H_5O_7$) 99% and hydrogen peroxide (H_2O_2) 30% were purchased from Lobachemie. Ammonium hydroxide (NH_4OH) 1%, sodium chloride ($NaCl$) 99%, sulfuric acid (H_2SO_4) 98% were purchased at M&M representations. Graphene oxide powder was purchased from Abalonyx Innovative materials 105 with a C/O atomic ratio = 2.5 - 2.6. Potassium ferricyanide ($K_3[Fe(CN)_6]^{3-/4-}$) 99%, and phosphate buffer 98% at a pH of 7 were purchased from Fisher Chemical.

5.2 Synthesis of AgNPs/GO and AuNPs/GO nanocomposites

5.2.1 Preparation of GO dispersed solution

0.1wt% of *GO* was prepared by dispersing 0.013 g of *GO* powder in 9.9 mL of water. Then, 100 μ L of *PVA* 1wt% were added to the solution. Finally, *GO* with *PVA* was put under sonication for 2h at room temperature conditions. After 2h the *GO* dispersion takes a brown color, as shown in Fig. 5.1, which indicates a visible dispersion and stability of *GO* powder in water and *PVA*.



Figure 5.1: GO powder dispersed in water and PVA.

5.2.2 Light Chamber

A high-power light chamber was fabricated using the process proposed by Saade & Araújo²¹. A PVC tube of 17 cm of longitude and 11.5 cm of diameter was used as the chamber structure and high power LEDs (5 W) were used as the light source. To fabricate the chamber, six LEDs lights of 540 nm excitation wavelength were connected in series to place them at the bottom of the PVC tube forming a ring. This specific wavelength was used because previous studies in our lab demonstrated that the electrochemical properties are better for nanoparticles irradiated with 540 nm than those irradiated with other wavelengths¹²⁰. To ensure good energy distribution toward the sample, the LEDs are equidistantly placed inside the chamber forming a ring. Finally, to avoid any external light contamination, aluminum foil was used at the top of the PVC tube to close the chamber as is shown in Fig. 5.3.

5.2.3 Chemical synthesis of silver and gold nanoparticles

Solutions prepared to perform the chemical synthesis are the following: 10 mL $AgNO_3$ (0.05 M), 10 mL $HAuCl_4$ (0.05 M), 10 mL $NaBH_4$ (100 mM), 10 mL $Na_3C_6H_5O_7$ (75 mM), and hydrogen peroxide (30%w/v).

The chemical synthesis begins by adding 28.4 mL of demineralized water into a 50 mL beaker. Subsequently, 150 μ L of $AgNO_3$ and 400 μ L of trisodium citrate were added and vigorously stirred using a magnetic bar at room temperature. After 3 minutes of stirring, 4 μ L of $NaBH_4$ was added under vigorous stirring for 3 minutes until a light yellow solution was obtained. Then, 60 μ L of H_2O_2 were added, leading to a colorless solution. Finally, 250 μ L of $NaBH_4$ were rapidly injected, turning the colorless solution into a reddish yellow one. In this synthesis, the reducing agent ($NaBH_4$) was used to reduce the ionic silver into metallic generating silver nanoparticles. After adding the stabilizing and reducing agent to the $AgNO_3$ solution, a light yellow solution was observed. Then, the addition of

H_2O_2 generated a colorless solution. Gold and silver nanoparticles can easily modify the stacking sequence in their crystal structure which promotes dislocation in their atomic planes due to their low stacking-fault energy¹². This feature allows the formation of planar structures when metallic nanoparticles are exposed to an etching agent. Next, the last addition of the reducing agent generates a change of color to a reddish yellow one as is shown in Fig. 5.2 (a).

In the chemical synthesis of gold nanoparticles, the same process was followed replacing $AgNO_3$ by $HAuCl_4$. The same quantities were used to keep similar conditions for further comparisons. A reddish solution was obtained from the synthesis. $NaBH_4$ was used as the reducing agent, which reduces all ionic gold components from $HAuCl_4$ into metallic gold to produce Au nanoparticles. Additionally, trisodium citrate was used as a capping agent, helping in the stabilization of the colloid to prevent instant agglomerations during the nucleation and growth process. At this point of synthesis, the aqueous solution turns an extremely soft purple color, almost transparent which indicates the formation of nanoparticles. Subsequently, hydrogen peroxide was used to generate effects in the anisotropic properties of gold nanoparticles. H_2O_2 acts as an etching agent which promotes the formation of planar structures by breaking the isotropic symmetry of fcc nanoparticle structure¹². The addition of H_2O_2 generates another change in the color, in this case, a colorless solution is observed which indicates the oxidation of nanoparticles. Finally, the last addition of $HAuCl_4$ produces a reddish solution having gold nanoparticles, as observed in Fig. 5.2 (b).

The formation of different colors in silver and gold nanoparticles observed in Fig. 5.2, depends on the quality and quantity of components used in the chemical synthesis. Finally, solutions containing silver and gold nanoparticles obtained using wet chemical synthesis will be called as $AgNPs$ and $AuNPs$ respectively.

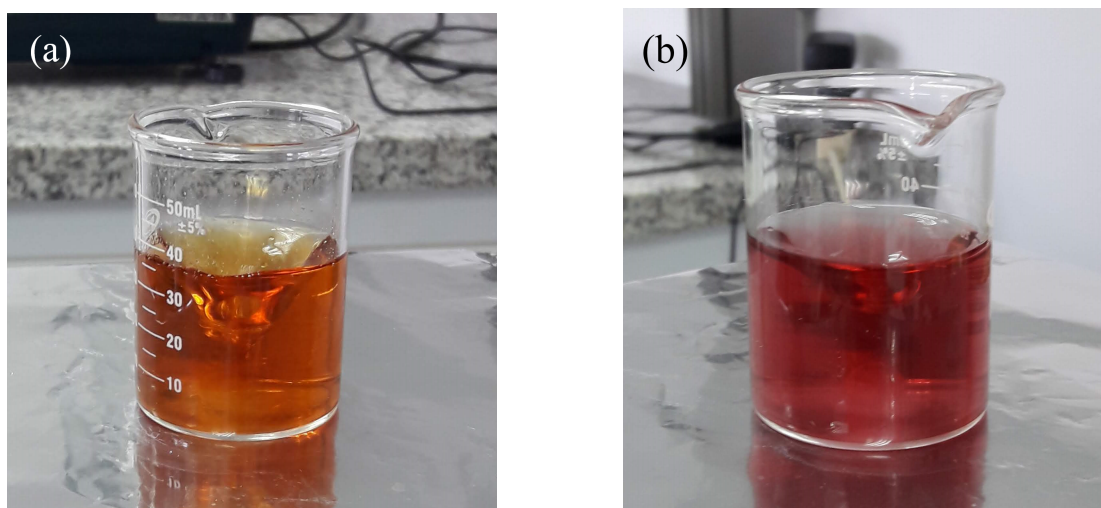


Figure 5.2: Solutions obtained before the irradiation (a) Silver nanoparticles ($AgNPs$) and (b) Gold nanoparticles ($AuNPs$).

5.2.4 Synthesis of AgNPs/GO and AuNPs/GO nanocomposites

To obtain the seed nanocomposites, each 30 mL of AgNPs and AuNPs seed solutions described in Section 5.2.3 are mixed with 50 μL of NH_4OH . Finally, 976 μL of GO solution is added to each one.

5.2.5 Photoreduction of the nanocomposites

The AgNPs/GO and AuNPs/GO seed nanocomposite solutions were filled into 15 mL vials and placed inside the irradiation chamber described in Section 5.2.2 and irradiated with 540 nm wavelength light for 16 hours. To execute the irradiation, a Phywe power supply was used with an applied current of 0.7 A and a voltage of 5 V. The setup used for the photoreduction synthesis is exposed in Fig. 5.3.

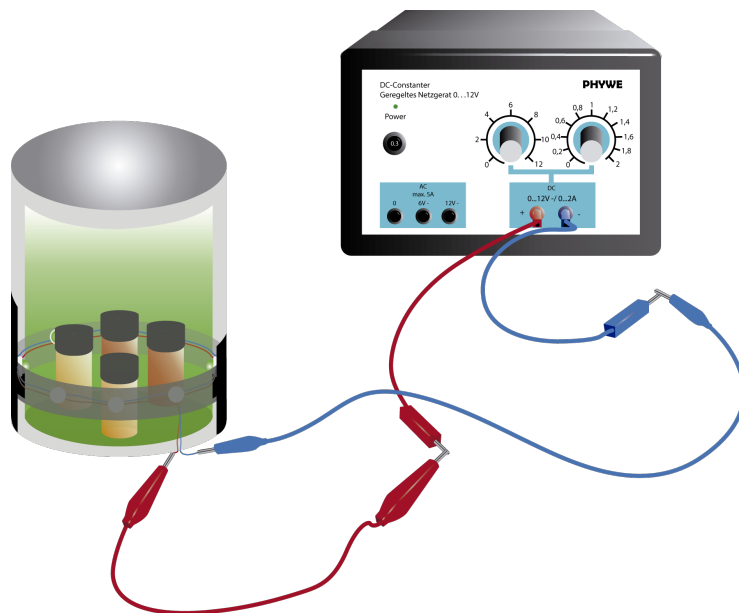


Figure 5.3: Light chamber at 540 nm excitation wavelength used to perform the photo-reduction method.

After 16 h of exposure, the initial color of silver and gold seeds nanocomposites changes to blue and brownish respectively. The final solutions obtained after photoreduction are shown in Fig. 5.4. The same method was used for AuNPs/GO and AgNPs/GO, based on surface plasmon resonance (SPR) and localized surface plasmon resonance (LSPR) theory¹²¹. The total photochemical reduction synthesis involves a redox reaction where the presence of H_2O_2 produces free ions of Au^{3+} or Ag^+ respectively for each sample. Next, the irradiation process generates holes with high energetic levels which are able to oxidize citrate ions and keep electrons on the surface of the nanoparticle to promote the growth of particles by reducing silver ions. In general, the properties of the plasmonic nanoparticles allows the absorption of light to generate an electric field which flows from citrate ions to electron free ions of metals

on each sample, causing the growth of nanoparticles with different size and shapes according to the specific plasmon excitation¹³.

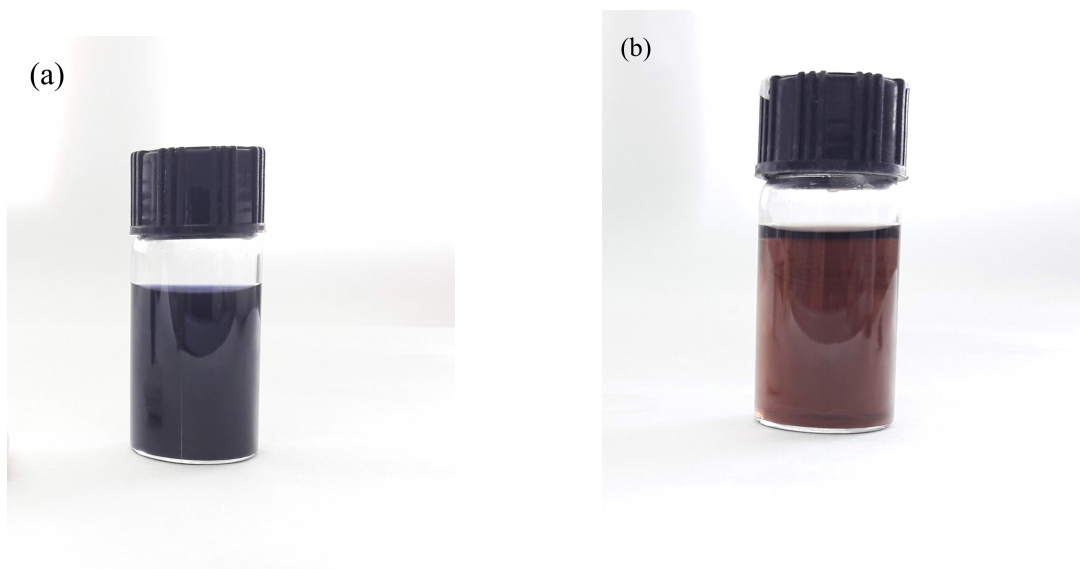


Figure 5.4: Final solutions obtained after photo-reduction (a) Silver nanoparticles on graphene oxide having planar faces (*AgTNPs/GO*) and (b) gold nanoparticles on graphene oxide having planar faces (*AuCNPs/GO*).

5.3 Characterization Equipment

5.3.1 Spectroscopy Techniques

UV-Vis Spectrometer

UV-Vis characterization to analyze the optical properties and absorption spectra of the nanocomposites were performed using a Genova Nano Jenway Spectrophotometer. The equipment was configured to collect data from 300 to 900 *nm* without using any dilutions of the sample. The spectrophotometer requires only 10 μL of pure *Ag* and *Au* nanoparticles fixed on a small membrane because it allows avoiding saturation and perturbations translated as a noise signal. First, the equipment was calibrated using demineralized water to compare the background measurements with the sample to generate a significant signal. Subsequently, seeds solutions and final solutions of *AgNPs/GO* and *AuNPs/GO* nanocomposites were measured to make further comparisons. Genova Nano Jenway Spectrophotometer in Fig. 5.5.



Figure 5.5: Genova Nano Jenway Spectrophotometer

FTIR spectrometer

The analysis of the absorption bands of *AgNPs/GO*, *AgTNPs/GO*, *AuNPs/GO*, and *AuCNPs/GO* nanocomposites were performed using Agilent Cary 630 FTIR spectrometer at Yachay Tech. The data were collected with Agilent MicroLab Software from FTIR equipment. The data was acquired within a range between 400 and 4000 cm^{-1} . Finally, the data was analyzed using Spectragryph and Origin-Pro software. FTIR equipment is shown in Figure 5.6



Figure 5.6: Agilent Cary 630 FTIR Spectrometer.

Raman spectrometer

The analysis of the surface-enhanced Raman scattering effect between metal plasmons and *Go* was performed at Horiba Scientific - LabRAMAN HR Raman spectrometer at Yachay Tech using lasers of 2 different wavelengths: green laser (532 nm) and red laser (633 nm). Raman equipment is shown in Fig. 5.7.

Sample preparation

Samples for Raman measurements were prepared on a silicon substrate. Using a micropipette, 1000 μL of pure *AgTNPs/GO* and *AuCNPs/GO* dispersions were deposited on the surface of the substrate and dried at 30°C.



Figure 5.7: Horiba Scientific - LabRAM Aramis Raman spectrometer.

5.3.2 Microscopy techniques

Scanning Electron Microscopy

SEM micrographs were acquired by a Scanning Electron Microscope PHENOM PRO X from AMPTEK at Yachay Tech. The software used to analyze the images obtained was ImageJ and size distribution determination was performed using Origin Pro software.

Atomic Force Microscopy

NaioAFM equipment from Nanosurf AG Company at Escuela Politécnica Nacional was used to assess the size distribution of *Ag* and *Au* nanocomposites. The measurements were made using phase-contrast imaging in tapping mode with a Tap190AI-G tip. Those parameters were used to prevent damages to the surface of the sample. Finally, the vibration amplitude was chosen to be 110 V and the image size parameter was adjusted according to the required observation. NaioAFM equipment is shown in Fig. 5.8.

Sample Preparation

For AFM measurements, samples of *AgNPs/GO*, *AgTNPs/GO*, *AuNPs/GO*, and *AuCNP/GO* nanocomposites were prepared on a mica sheet used as substrate. First, the mica sheet is exfoliated using Scotch tape 3 times. Then, using a micropipette, 1000 μL of each *Ag* and *Au* nanocomposites without dilution were deposited on the surface of the mica and dried at around 80°C to remove contaminants.

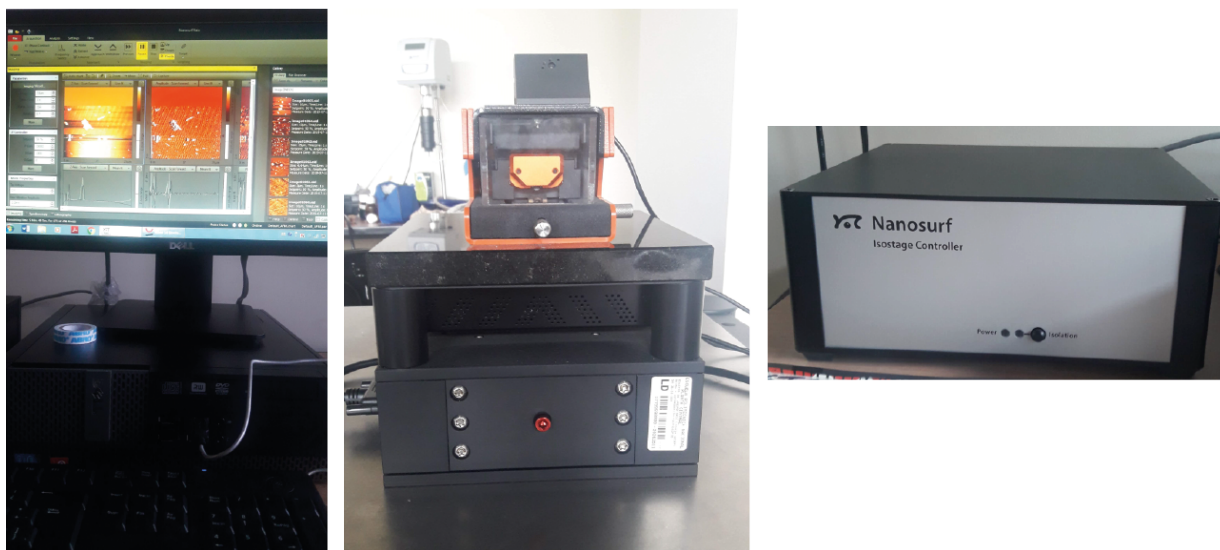


Figure 5.8: NaoAFM equipment used for AFM measurements.

5.3.3 Electrochemical Techniques

Cyclic Voltammetry

Cyclic voltammetry was used to record cyclic voltammograms to determine the kinetic parameters of modified electrodes with metallic nanocomposites, and analyze its application on H_2O_2 sensing. All cyclic voltammograms were obtained using $\mu\text{Stat}300$ potentiostat connected via USB to DropView 8400 Software from Metrohm DropSens Company shown in Fig. 5.9.



Figure 5.9: μ Stat300 potentiostat equipment and DropView 8400 Software used to record cyclic voltammetry measurements.

Modified carbon working electrode

The commercial graphite Pentel Ain Stein pencil lead $0.5 \times 60 \text{ mm-B}$, were cleaned in a $0.5\text{M } H_2SO_4$ solution exposed to continuous potential cyclic between -0.5 V and 1 V vs Gra at a scan rate of 0.5 V/s . Several scans were performed to obtain a clean and homogeneous electrode surface shown in Fig. 5.10. After conditioning the electrode, the nanocomposites were electrochemically deposited on its surface. To attach nanocomposites to the surface of the working electrode, 25 scans were performed using a sweep potential between -1.0 V and 0V vs graphite electrode (Gra) and a scan rate of 0.1 V/s . Finally, to investigate their electrochemical properties of spherical silver nanoparticles on graphene oxide ($AgNPs/GO$), silver nanoparticles on graphene oxide having planar faces ($AgTNPs/GO$), spherical gold nanoparticles on graphene oxide ($AuNPs/GO$), and gold nanoparticles on graphene oxide having planar faces ($AuCNP/GO$) nanocomposites modified electrodes, different measurements in $NaCl$, $(K_3[Fe(CN)_6])^{3-/4-}$ solutions, as well as phosphate buffer, were performed.



Figure 5.10: Graphite electrodes used for recording the cyclic voltammograms.

Electrochemical micro-Cell design

A home-made-micro-cell of about 1.5 mL capacity was built using an Eppendorf vial to perform all electrochemical experiments. Commercial graphite pencil leads were used as reference and counter electrodes, and Ag and Au nanocomposites modified graphite leads were used as working electrodes. The design of the three-electrode micro-cell system is observed in Fig. 5.11.

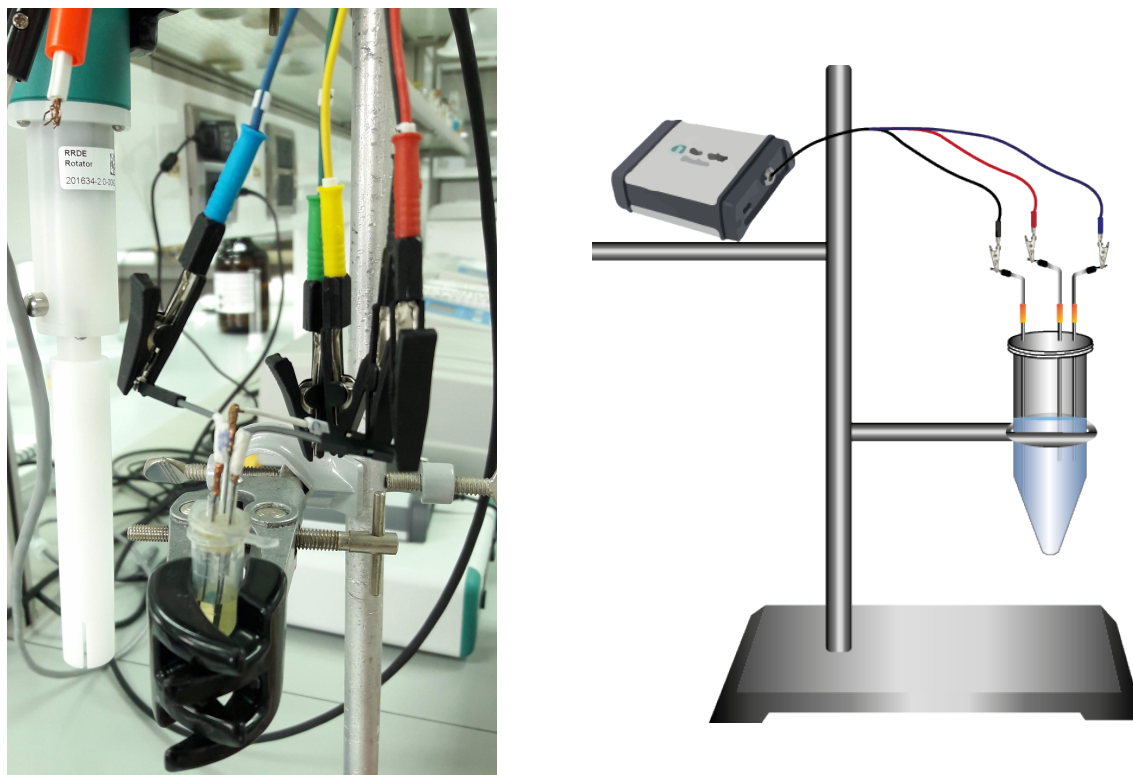


Figure 5.11: Set up and schematic representation of the design of three-electrode micro-cell system respectively used to record the cyclic voltammograms. Electrodes color codes are, blue: reference electrode, black: counter electrode, and red: working electrode.

Electrochemical analysis

To calculate the diffusion coefficients, cyclic voltammograms were recorded for different scan rates: 10, 25, 50, 100, 150, 200 $\frac{mV}{s}$, then the anodic and cathodic peaks were extracted for each one. By analyzing multiple voltammograms at different scan rates, one of the most important variables in cyclic voltammetry, information about the reaction at the working electrode can be obtained. Anodic and cathodic diffusion coefficients can be obtained from the gradient of the Randles-Sevcik equation, which predicts that the peak current is related to the square root of scan rate as shown in equation 5.1.

$$i_p = 0.4463 \frac{(nF)^{3/2}}{(RT)^{1/2}} A(D_i\nu)^{1/2} \quad (5.1)$$

Where i_p is the anodic or cathodic peak, A is the electroactive area, C is the concentration of the analyte, n is the number of transferred electrons in the redox reaction, F is the Faraday's constant, R is the gas constant, T is the temperature, D_i is the anodic or cathodic diffusion coefficient, and ν is the scan rate¹¹⁶.

Using the Randles-Sevcik equation 5.1, a i_p vs $\nu^{1/2}$ plot was created. Manipulating equation 5.1 to obtain equation 5.2, the diffusion coefficients can be determined from the slope.

$$slope = 0.4463AC \frac{(nF)^{3/2}}{(RT)^{1/2}} (D_i)^{1/2} \quad (5.2)$$

Furthermore, information about the reversibility of the redox reaction can be extracted from a voltammogram through calculations of standard rate constant k° which is a quantity that describes the reversibility of the reaction, assuming large values for reversible and medium to very low values for quasi and irreversible reactions¹¹⁶.

Lavagnini *et al*¹²² developed a methodology that unifies methods by Nicholson, Klingler, and Kochi to analyze the separation between anodic and cathodic peak potentials called ΔE_p and the dimensionless kinetic parameter (ψ). These calculations are possible through the relation between ψ and ν given by equation 5.3

$$\psi = k^\circ \left(\frac{\pi D_i n \nu F}{RT} \right)^{-1/2} = k^\circ Y \nu^{-1/2} \quad (5.3)$$

But, Lavagnini *et al* propose the simplified equation for ψ in function of ΔE_p shown in equation 5.4.

$$\psi = \frac{-0.6288 + 0.0021X}{1 - 0.017X} \quad (5.4)$$

Where $X = n \Delta E_p$. The values of k° are obtained from the fit of ψ vs $Y\nu^{-1/2}$.

However, it should be pointed out that to apply the equation 5.4 proposed by Lavagnini, the value of the transfer coefficient (α) should lie within the range of $0.3 < \alpha < 0.7$. Then α can be determined from the anodic or cathodic peak potential and the half-peak potential using the equation 5.5¹¹⁶.

$$\alpha = \frac{1.875RT}{nF |E_p - E_{p/2}|} \quad (5.5)$$

Chapter 6

Results & Discussion

6.1 UV-Vis spectroscopy

UV-Vis spectroscopy was used to study the optical properties and absorption spectra of the samples. Those characteristics are related to the size and shape of the nanoparticles which can be predicted by the observation of different colors exposed on each sample. The graphene oxide dispersed solution was used to prepare the nanocomposites. Fig. 6.1 shows the first peak around 226 nm which represents the $\pi \rightarrow \pi^*$ transitions of aromatic $C - C$ bonds as is detailed in Table 6.1, and the second peak as a shoulder is centered at 301 nm corresponding to $n \rightarrow \pi^*$ transitions of $C = O$ as is shown in Table 6.1 which is in agreement with the literature¹²³.

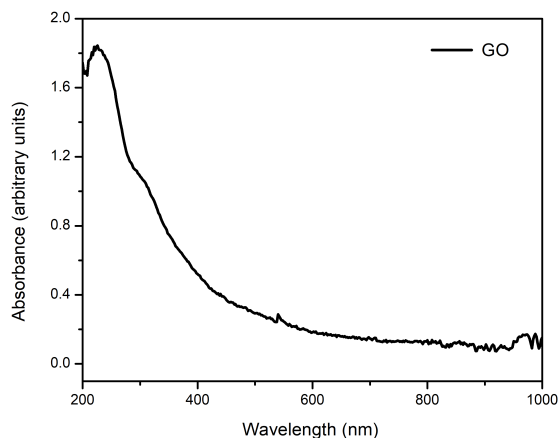


Figure 6.1: UV-Vis spectrum of graphene oxide dispersed solution used to prepare gold and silver nanocomposites.

Gold and silver nanoparticles were obtained through the same method, but each one exhibits a characteristic color that is related to the optical properties and the absorption spectra of the nanocomposites. *AuNPs/GO* and *AgNPs/GO* change their color when exposed to 540 nm of irradiation wavelength forming *AuCNP*s/GO and *AgTNPs/GO* respectively, which is shown in figures 6.2 and 6.3. Fig. 6.2 presents UV-Vis spectra of gold nanocomposite before (*AuNPs/GO*) and been irradiated with 540 nm (*AuCNP*s/GO). The presence of noise in the data does not allow to fully visualize the bands that were generated, therefore, the possible bands which must be observed to have spherical gold nanoparticles and gold nanoparticles on graphene oxide having different structures as nanocubes or nanoplates are shown in figure 6.2 by the brown and reddish arrows respectively. For *AuNPs/GO* and *AuCNP*s/GO the first peak must be observed around 226 nm or a little shifted to the right to be related with $n \rightarrow \pi^*$ transitions of $C = O$ from GO which indicates the interaction between gold nanoparticles and GO sheets to form the nanocomposite¹²⁴. Also the second peak related to GO could be observed around 301 nm or shifted to the right corresponding to $n \rightarrow \pi^*$ transitions of $C = O$ ¹²³, as shown in Table 6.1. In the case of *AuNPs/GO* the strong absorption band must appear around 530 nm corresponding to spherical-shape gold nanoparticles, and for *AuCNP*s/GO the strong band must be shown shifted to the right around 540 nm to observe gold nanoparticles having different shapes^{10 125 126} as is also observed in Table 6.1.

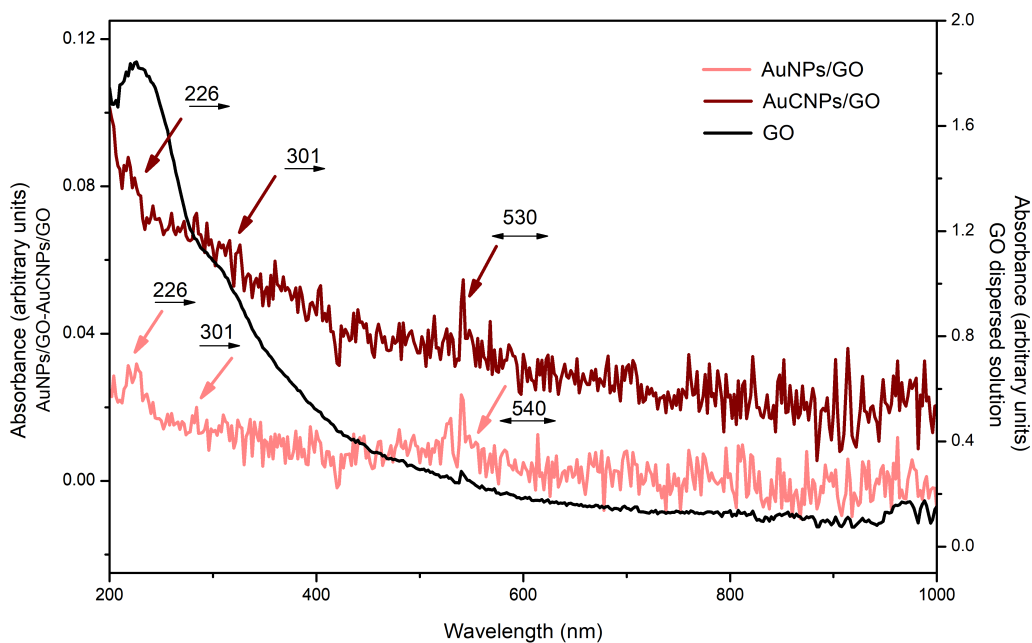


Figure 6.2: UV-Vis spectra of gold nanocomposite before been irradiated (*AuNPs/GO*), and gold nanocomposite after 16 h of irradiation at 540 nm (*AuCNP*s/GO).

On the other hand, Fig. 6.3 presents UV-Vis spectra for $AgNPs/GO$ and ($AgTNPs/GO$). $AgNPs/GO$ nanocomposite exhibits two main absorption bands. The first SPR is observed on 284 nm related to $n \rightarrow \pi^*$ transitions of $C = O$ bonds in graphene oxide solution as is shown in Table 6.1. This band confirms the formation of $AgNPs/GO$ nanocomposite due to interactions between silver nanoparticles and graphene oxide structures, but the spectrum exhibits a blue-shift proposing a possible reduction of graphene oxide during the process of synthesis¹²⁷. Finally, for $AgNPs/GO$ nanocomposite the strongest plasmonic band is centered at 437 nm as is observed in Table 6.1. corresponding to the formation of spherical-shaped silver nanoparticles¹¹. For $AgTNPs/GO$ is difficult to recognize the bands corresponding to the interaction between GO and silver nanoparticles due to the presence of noise. Then, the strongest plasmonic band is observed in 586 nm corresponding to in-plane dipole resonance¹²⁸ as shown in Table 6.1. Furthermore, as a well-defined band and a very weak secondary band are observed, the presence of single modal size distribution can be identified as having a specific particle size¹²⁹.

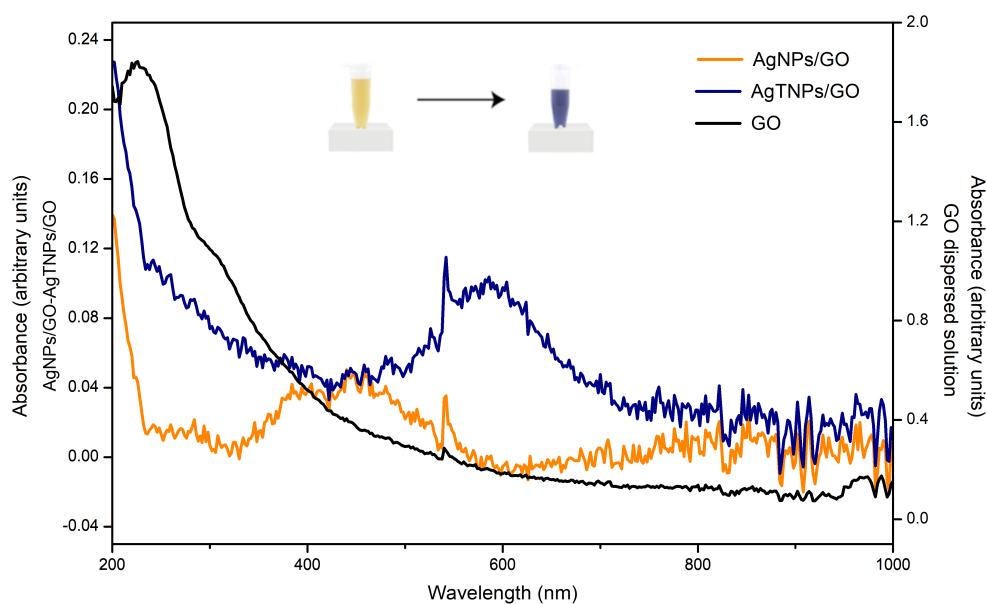


Figure 6.3: UV-Vis spectra of silver nanocomposite before been irradiated ($AgNPs/GO$), and silver nanocomposite after 16 h of irradiation at 540 nm ($AgTNPs/GO$).

Sample	Peak Position (nm)	Transition
GO	226 301	$\pi \rightarrow \pi^*$ transitions of aromatic C – C bonds. $n \rightarrow \pi^*$ transitions of C = O
<i>AuNPs/GO</i>	226 301 530	$\pi \rightarrow \pi^*$ transitions of aromatic C – C bonds from GO which could confirm the formation of nanocomposite due to the interaction between gold nanoparticles and GO sheets ¹²⁴ . $n \rightarrow \pi^*$ transitions of C = O from GO ¹²³ . Strong absorption band corresponding to spherical gold nanoparticles ^{10 125 126} .
<i>AuCNPs/GO</i>	226 301 540	$\pi \rightarrow \pi^*$ transitions of aromatic C – C bonds from GO ¹²⁴ . $n \rightarrow \pi^*$ transitions of C = O from GO ¹²³ . SPR corresponding to the formation of gold nanoparticles having planar faces ^{10 125 126} .
<i>AgNPs/GO</i>	284 437	$n \rightarrow \pi^*$ transitions of C = O bonds coming from GO ¹²⁷ . strongest plasmonic band corresponding to the formation of spherical-shaped AgNPs ¹¹ .
<i>AgTNPs/GO</i>	586	Strong plasmonic band corresponding to in-plane dipole resonance for single modal size distribution ^{129 128} .

Table 6.1: UV-Vis characteristic peaks for GO dispersed solution, *AuNPs/GO*, *AuCNPs/GO*, *AgNPs/GO*, and *AgTNPs/GO* nanocomposites.

The absorbance signal for *AuNPs/GO* and *AuCNPs/GO* nanocomposites shown in Fig. 6.2 is weaker than the absorbance signal for *AgNPs/GO* and *AgTNPs/GO* nanocomposites observed in Fig. 6.3, which is directly related with the concentration of nanoparticles in the nanocomposite according to Lambert-Beer Law exposed in equation 4.1. Therefore, the low signal observed in *AuNPs/GO* and *AuCNPs/GO* nanocomposites spectra could be generated by the low concentration of nanoparticles in the sample, which implicates that the low amount of particles in the nanocomposites generate a decrease in the intensity of absorbance signal. In the case of *AgNPs/GO* and *AgTNPs/GO* nanocomposites, it is observed a higher signal which indicates the higher concentration of nanoparticles in the sample with respect to *AuNPs/GO* and *AuCNPs/GO*. The difference in concentration between these two types of nanocomposites, even when the same method of synthesis was used is related to the wavelength of resonance of gold and silver compounds.

Finally, in Figure 6.2 the characteristic colors generated when *AuNPs/GO* is irradiated with 540 nm to form *AuCNPs/GO* can be observed. The change in color occurs due to the optical properties observed with UV-Vis characterization that are directly related to the size and shape of nanoparticles. In the case of the silver nanocomposites, the transition of the color from yellow to blue is observed, which confirms the change in size and

shape, therefore, the presence of different resonance modes are expected. The same process is observed in Figure 6.3 for gold nanocomposites, where a change in the color solution from a reddish one to a brown is observed. This fact corroborates the influence of the photoreduction method on the shape and size of the nanocomposites.

6.2 Microscopy Techniques

6.2.1 Scanning Electron Microscopy (SEM)

AuCNPs/GO and *AgTNPs/GO* samples were characterized using the SEM technique, which allows observe the surface morphology of the sample, giving preliminary information about size and shape due to the of the equipment. SEM micrographs of *AuCNPs/GO* and *AgTNPs/GO* were obtained with a backscattered electron detector (BSD). The main type of contrast distinguished in the images is atomic number contrast or Z-contrast, therefore, a difference in brightness is identified over the entire sample. Z-contrast is given by the number of backscattered electrons reaching the detector, consequently, the higher atomic number of the element, the higher intensity shown in the micrograph¹³⁰. To identify each specimen on the sample, gold and silver nanoparticles having higher atomic numbers will exhibit more brightness than graphene oxide which is composed mainly of carbon atoms.

Figure 6.4 presents the SEM micrographs of *AuCNPs/GO* samples. Figure 6.4 (a) shows a micrograph of gold nanoparticles where *GO* flakes are easily observed in the green circle. The magnification of the highlighted area shown in Fig. 6.4 (a) is observed in micrograph (b). Figure 6.4 (b) reveals the predominance of *GO* flakes which can be identified in red due to their large sizes and brightness, but several smaller nanoparticles can also be identified on *GO* sheets due to the difference in brightness intensities. Also, the cloudy-shape structures can be assigned to the *GO* sheets, near to the background as seen in the red highlighted area in Fig. 6.4 (b), and small bright structures represent small-size gold nanoparticles. Another inset was performed to obtain Figure 6.4 (c) which exhibits the 3D image of two possibilities: (i) a cubic-shape gold particle, (ii) a *GO* flake coated with Au nanoparticles. Finally, Figure 6.4 (d) shows the histogram of the size distribution for *AuCNPs/GO*, the length of the most visible nanoparticles in the micrograph were measured using Image J software. Observations on the size distribution determines that 52% of all measured structures have sizes between 80-120 nm. Then, 21% related with sizes from 40 to 60 nm, and 20% shows sizes from 120 to 160 nm, also 6% related with the formation of the biggest structures are observed in the micrograph.

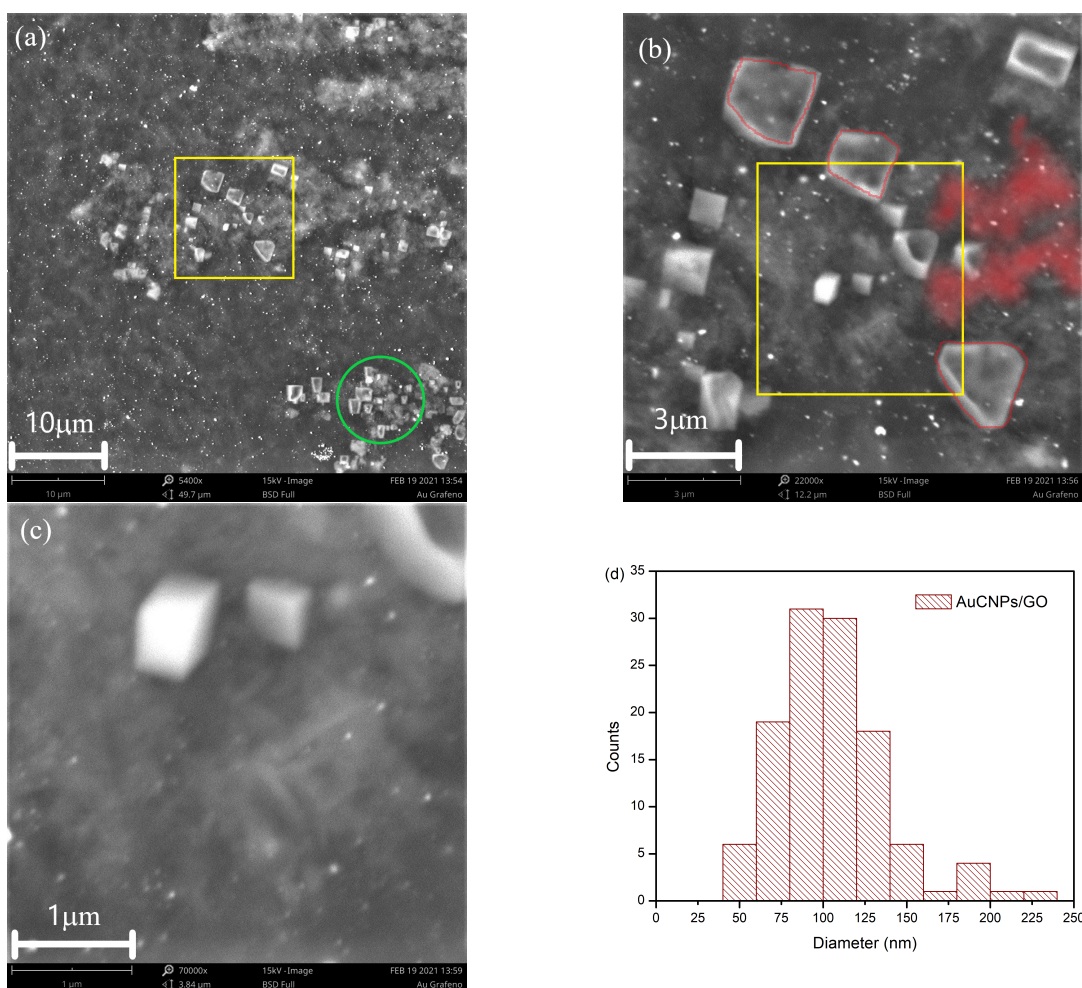


Figure 6.4: SEM characterization for *AuCNPs/GO*. (a) SEM micrograph for *AuCNPs/GO*. (b) Magnification of the yellow area in (a). (c) Yellow area marked in (b). (d) Histogram of the size distribution for *AuCNPs/GO* extracted from (b).

Using UV-Vis characterization, it could be observed that *Au* nanoparticles change the shape and size when they are irradiated with a wavelength of 540 nm. It was expected due to the change in the color of the solution obtained. Gold nanoparticles are formed when gold ions are reduced to metallic form during nucleation. To stabilize the solution, trisodium citrate is added to create a charged interface on the surface of the nanoparticles generating an excess of *Au* ions. To avoid agglomerations, *Au* nanoparticles are deposited in the surface of *GO* dispersed solution by using ammonium hydroxide. The energy generated by the irradiation of 540 nm allows the formation of gold nanoparticles having planar faces similar to platelets due to the trisodium citrate allows the growth according to the associated free energies to the planes in their internal structure¹³¹.

Figure 6.5 presents the SEM micrographs of *AgTNPs/GO* samples. Fig. 6.5 (a) exhibits the existence of Z-contrast where graphene oxide can be identified as cloud-like structures having less brightness than silver nanoparticles. In the micrograph, it is easy to differentiate small brightness structures (*AgNPs*) deposited on large supports with less intensity in brightness (*GO*). In green, a possible aggregation point of silver nanoparticles is identified. The highlighted area shown in 6.5 (a) is observed in (b). Fig. 6.5 (b) allows the observation of two complete graphene oxide sheets with attached nanoparticles. The biggest is observed in the green highlighted area which shows a size around $5 \mu\text{m}$ while the smallest has a size of $2 \mu\text{m}$, indicated by the yellow highlighted area. The magnification of the yellow square in (b) is shown in (c) where silver nanoparticles attached to the *GO* structure are visible. In the micrograph, more agglomerations are observed with greater intensities and sizes than silver nanoparticles. Finally, Fig. 6.5 (d) exhibits the histogram of the size distribution for *AgTNPs/GO*. Size distribution graph shows that 25% of the measured structures have sizes between 80-90 nm. Next, 20% has sizes between 70-80 nm, Then, 12% is related to sizes from 60 to 70 nm, and 11% represents sizes between 90-100 nm. Only 5% have sizes between 40-60 nm. In the end, other sizes represent agglomerations observed in the micrographs.

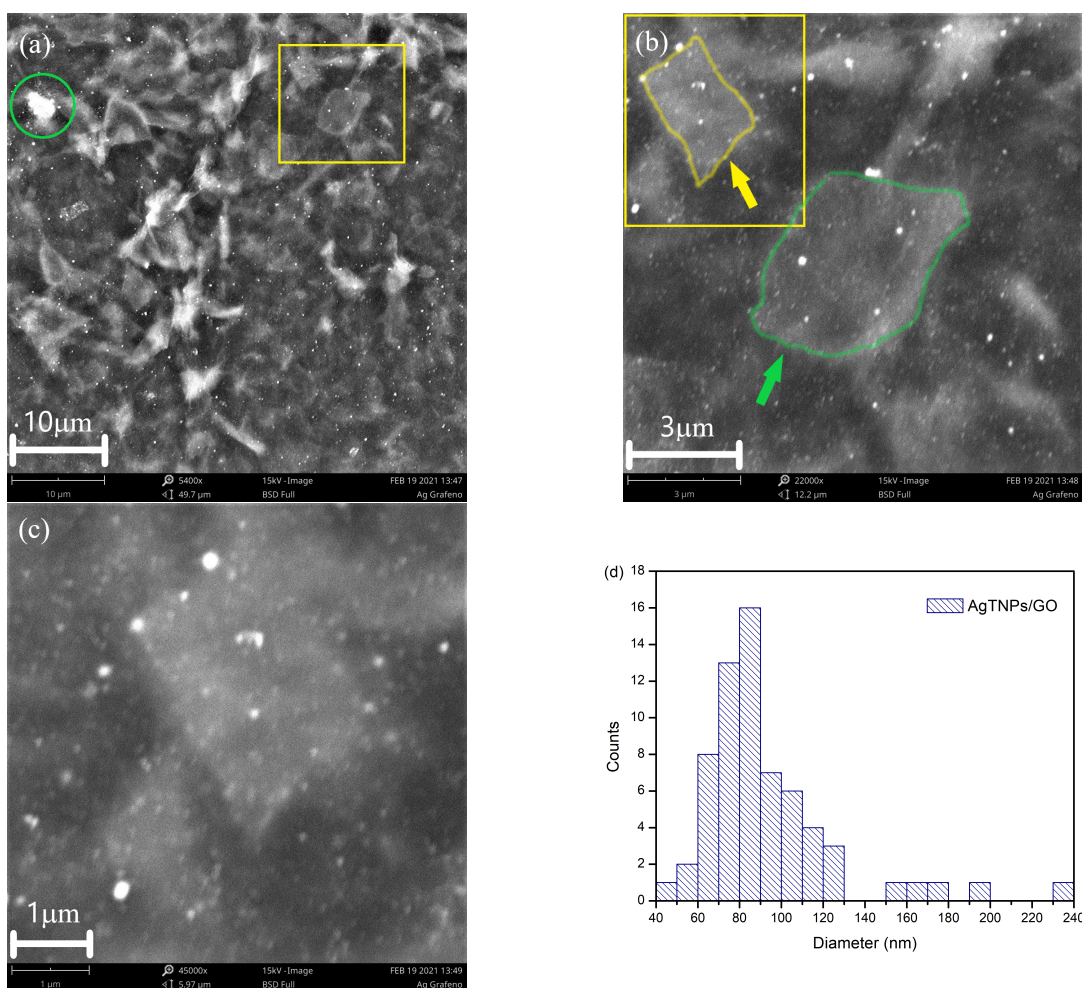


Figure 6.5: SEM characterization for *AgTNPs/GO*. (a) SEM micrograph. (b) Magnification of the yellow area in (a). (c) Yellow area marked in (b). (d) Histogram of the size distribution for *AgTNPs/GO* extracted from (c).

As demonstrated by UV-Vis characterization, *Ag* nanoparticles change the shape and size when they are irradiated with a wavelength of 540 nm . Initially, quasi-spherical silver nanoparticles (*AgNPs/GO*) are obtained, as demonstrated by Lasso E.¹²⁰. The nanoparticles are formed when the nucleation process occurs, silver ions are reduced to metallic silver to form *Ag* nanoparticles. During the synthesis, a stabilizer (*TSC*) was added which prevents agglomeration, subsequently, *Ag* nanoparticles are deposited on the surface of graphene oxide using ammonia from ammonium hydroxide as a ligand. When this solution is exposed to the irradiation of light at 540 nm , the excess of ions generated around the silver nanoparticles is reduced while trisodium citrate allows the formation of other shapes of *Ag* nanostructures such as nanoplates and planar structures as is demonstrated by Lasso E. on his graduation project¹²⁰. This fact of trisodium citrate allows the growth along the lateral direction and the blocking growth along

the vertical direction¹³². It is necessary to emphasize that the morphology of silver nanoparticles cannot be clearly identified due to the limited resolution observed in the SEM micrographs which could also suggest limited resolution measurements of the data extracted from the micrographs, therefore, another characterization method that allows obtaining more accurate measurements is necessary.

6.2.2 Atomic Force Microscopy (AFM)

AFM technique was used to observe the topographic features of the samples to support and corroborate the information obtained with SEM. Atomic Force Microscopy provides information in three dimensions, specifically, the AFM technique generates magnification in x , y , and z . To get measurements in length and height, an analysis in the x and z -axis was performed respectively for *AuNPs/GO*, *AuCNPs/GO*, *AgNPs/GO*, and *AgTNPs/GO* nanocomposites.

Figure 6.6 shows AFM characterization of *AuNPs/GO*. Fig. 6.6 (a) exhibits the micrograph obtained using AFM tapping mode on the surface of the sample. In the image, different well-marked sizes of *AuNPs/GO* are observed. Nanoparticles having different sizes can be well distinguished which will be detailed later. Sample preparation includes an exfoliation of the substrate used to deposit the sample, sometimes the exfoliation is not usually as effective, generating noise observed as thin lines identified by the green arrows. Fig. 6.6 (b) indicates the height against length profile extracted using WSxM software¹³³ from one single *AuNP* in the micrograph on the surface of *GO*. The micrograph shows a slight shift in the background of around 1.46 nm, which can be identified as the substrate where the nanoparticles were deposited. Next, horizontal and vertical scales shown in blue indicate the measurements made to obtain the height and length data of nanoparticles. Fig. 6.6 (c) exhibits the histogram of height distribution for *AuNPs* on *GO*. The main contribution in the histogram is identified for heights between 25-55 nm corresponding to 84% of all structures, but the principal contributions are generated by nanoparticles having 25-30 nm and 40-45 nm which represent the 33% of the total. In the same way, Fig. 6.6 (d) indicates the histogram of lengths distribution for *AuNPs* on *GO*. The histogram shows lengths greater than 100 nm which represent the 23% of particles observed in (a), but the 77% corresponds to sizes less than 100 nm, where the 33% is related with lengths between 60 to 70 nm indicating the main contribution in the histogram represented by the biggest bar.

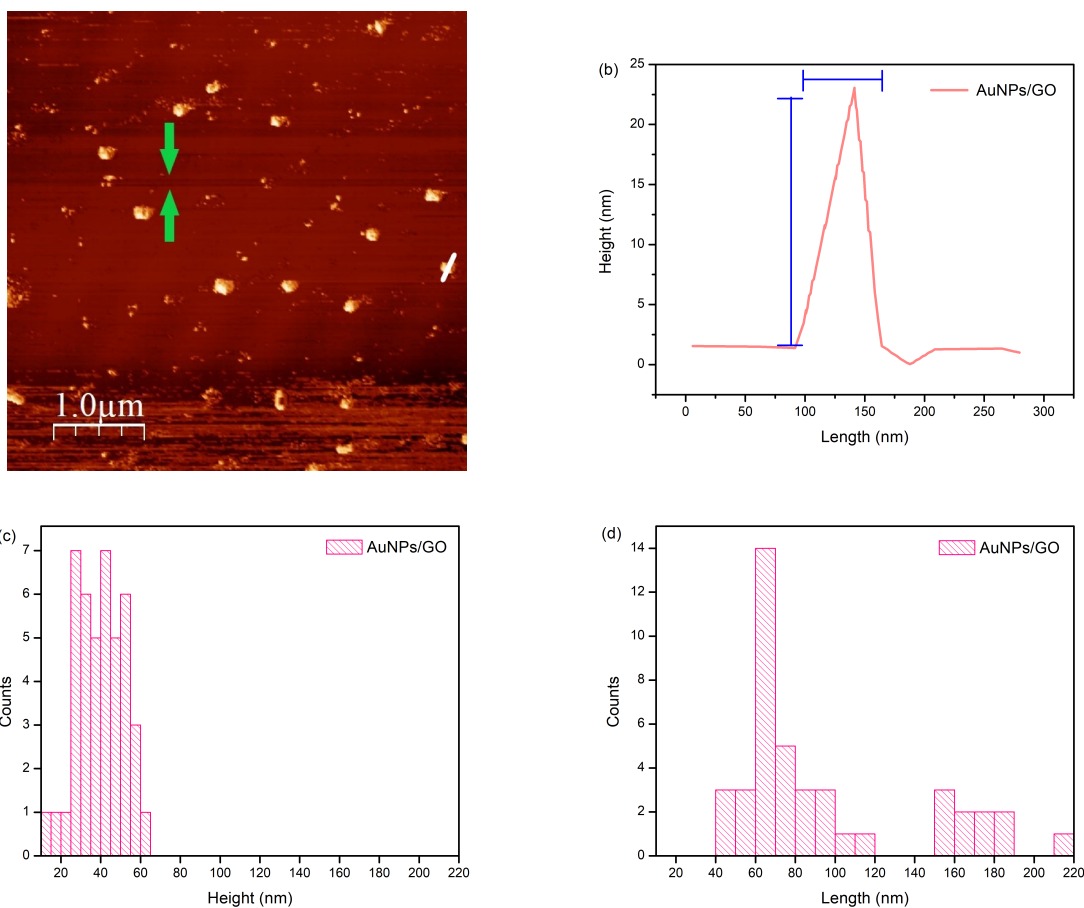


Figure 6.6: AFM characterization of *AuNPs/GO*. (a) AFM micrograph of *AuNPs* on *GO*. (b) Height against length profile measured for a single nanoparticle obtained from (a). (c) Histogram of height distribution for *AuNPs/GO*. (d) Histogram of length distribution for *AuNPs/GO*.

Figure 6.7 shows AFM characterization of *AuCNPs/GO*. Fig 6.7 (a) shows the smaller nanoparticles observed near the background in the SEM micrograph exhibited in Figure. 6.4 (b). AFM micrograph exhibits small nanoparticles having uniform sizes between 30 and 100 *nm*. It contributes with specific information of an area of the sample which contains the smallest structures generated during the synthesis. Fig 6.7 (b) indicates the height against length profile of a single *AuCNPs* observed in (a), in this case, the substrate manifests a thickness of around 1.91 *nm* shown by the small shift observed in the background of the profile close to zero¹³⁴. In addition, although it is not possible to perfectly identify the shape of *AuCNPs*, a large number of them were exposed to the measurements which generate a kind of planar faces in their topography, perhaps due to the existence of cubic or triangular structures. Fig. 6.7 (c) presents the histogram of height distribution for *AuCNPs* on *GO*. Structures with heights between 30

nm and $50 nm$ are the main contributors with 88% accuracy in the AFM micrograph, but the most frequent height is identified between $45 nm$ and $50 nm$ corresponding to 30 %. Fig. 6.7 (d) shows the histogram of lengths distribution for *AuCNPs*. The image suggests that the principal contribution is given by *AuCNPs* lengths between $70-75 nm$ representing the 33 %, but also other important frequent lengths are observed, namely between $45-50 nm$ and around $95-100 nm$, corresponding to the 20% of *AuCNPs* identified with AFM characterization.

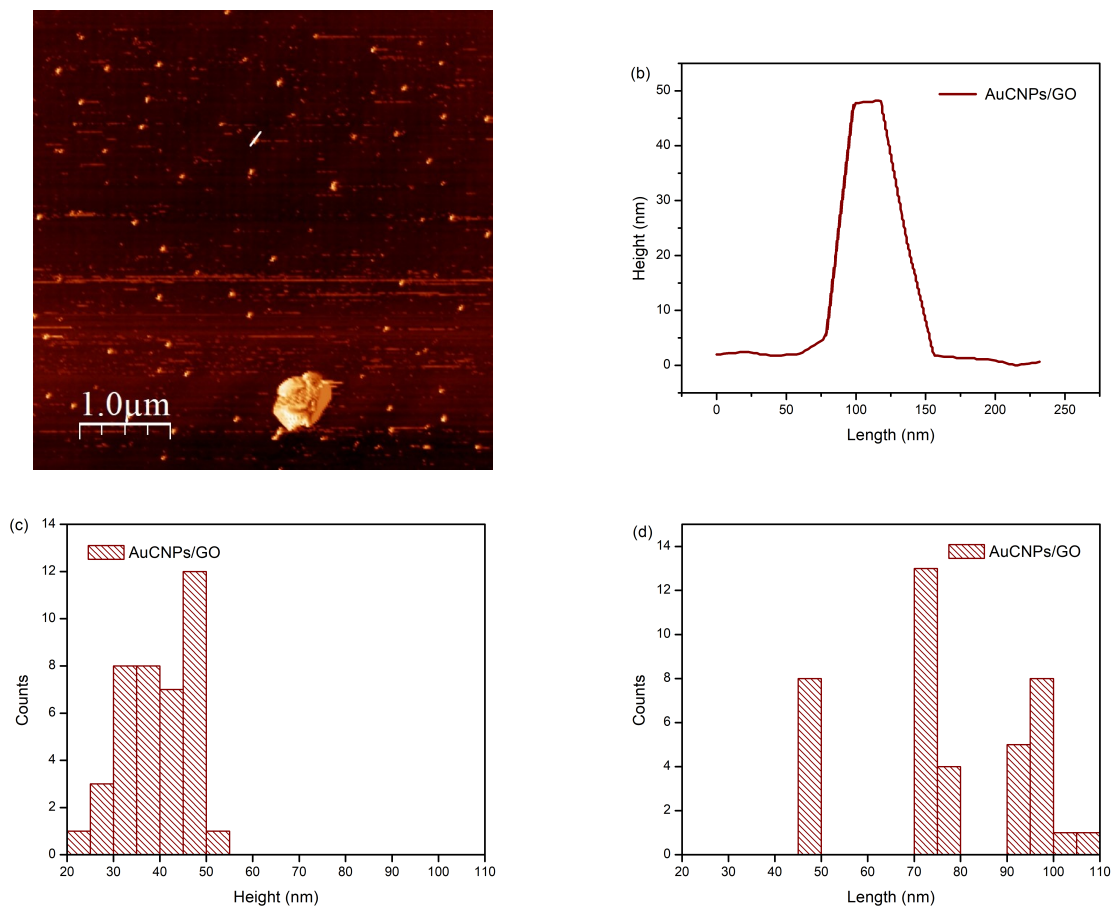


Figure 6.7: AFM characterization of *AuCNPs/GO*. (a) AFM micrograph of *AuCNPs* on *GO*. (b) Height vs length profile measured for one nanoparticle obtained from (a). (c) Histogram of height distribution for *AuCNPs/GO*. (d) Histogram of length distribution for *AuCNPs/GO*.

In Figure 6.8 (a), shows the AFM micrograph of *GO* decorated with *AgNPs*. The scale of the micrograph compared with the one performed for the *AuNPs* exposed in Fig. 6.6 (a) suggests that the synthesis method used reduce the size of the *AgNPs* particles compare to *AuNPs*. Figure 6.8 (b) shows the height vs length plot of a single

AgNP. Figure 6.8 (c) presents the histogram of height measurements made for *AgNPs* on *GO*. The largest number of nanoparticles observed have heights between 21-30 nm which corresponds to the 78% of all *AgNPs* observed in the micrograph Fig. 6.8 (a), shows that the most frequent heights are between 27-30 nm which represent 35% of *AgNPs*. Figure 6.8 (d) shows the main length contributions for *AgNPs* between 37-38 nm corresponding to the 53% of *AgNPs* observed with AFM characterization.

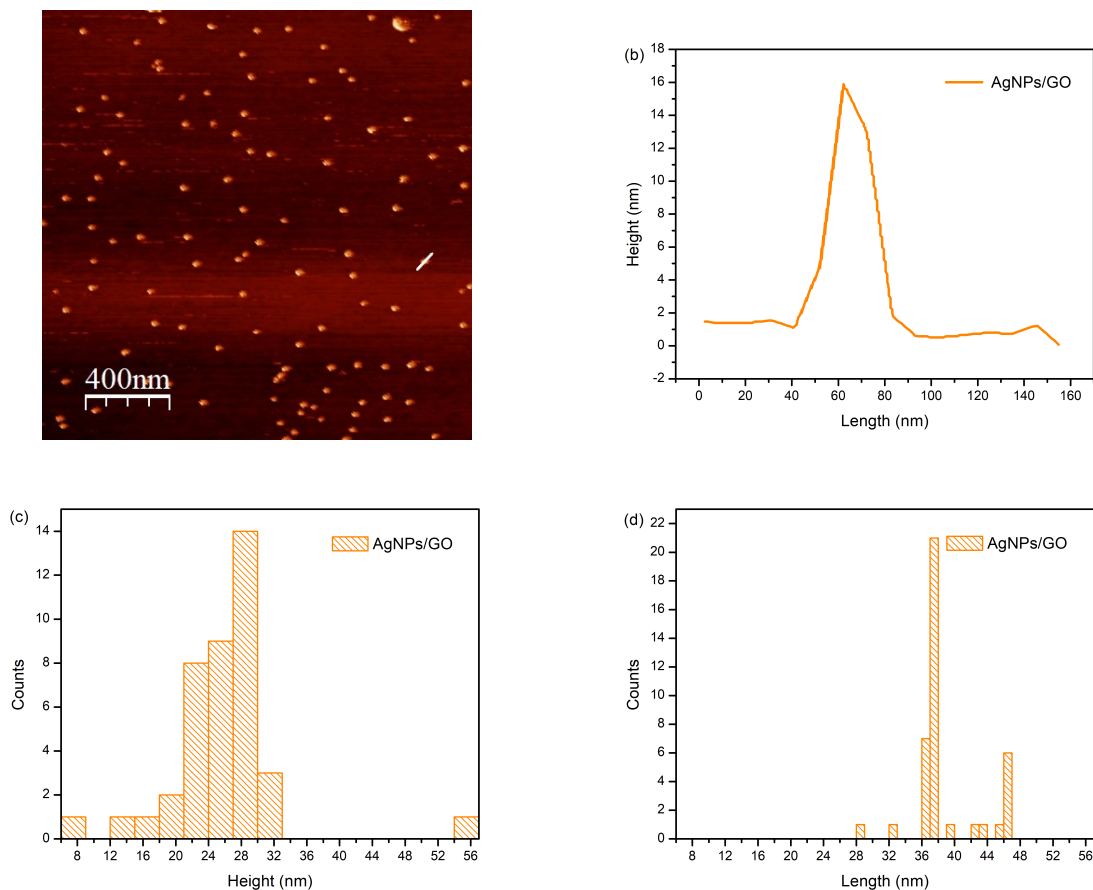


Figure 6.8: AFM characterization of *AgNPs/GO*. (a) AFM micrograph of *AgNPs* on *GO*. (b) Height vs length profile measured for one nanoparticle obtained from (a). (c) Histogram of height distribution for *AgNPs/GO*. (d) Histogram of length distribution for *AgNPs/GO*.

Figure 6.9 shows AFM characterization of *AgTNPs/GO* nanocomposite. In Fig 6.9 (a) AFM micrograph of *AgTNPs* is observed. Uniform *AgTNPs* are visualized in the image. Fig. 6.9 (b) shows the height vs length profile of the micrograph. In this case, the shape of *AgTNPs* can't be visualized very well, but the top of the graph exhibits

a planar topography in the height of the *AgTNP*, which could confirm the existence of structures with planar faces. Fig. 6.9 (c) and Fig. 6.9 (d) present the histograms for height and length distributions of *AgTNPs* respectively. The 100% of *AgTNPs* exhibit heights less than 41 nm observed in Fig. 6.9 (c), and the 100% shows lengths less than 34 nm visualized in Fig. 6.9 (d).

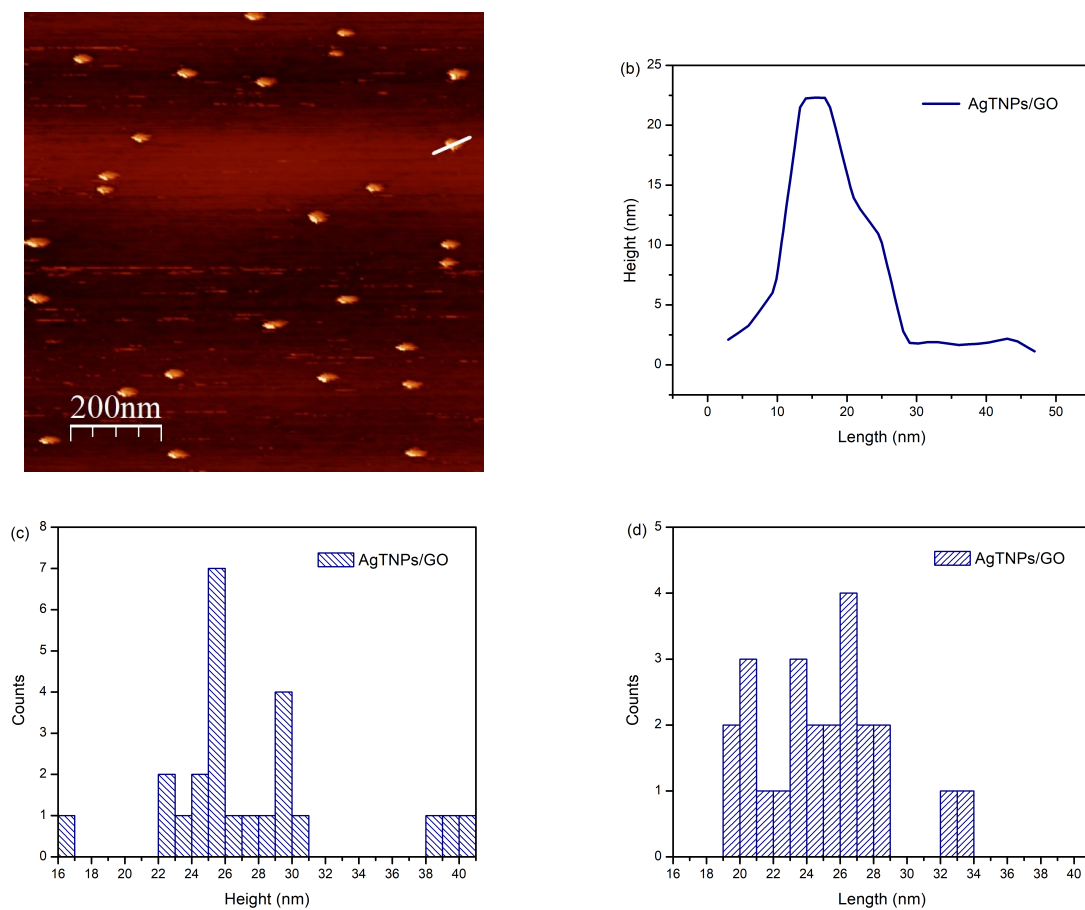


Figure 6.9: AFM characterization of *AgTNPs/GO*. (a) AFM micrograph of *AgTNPs* on *GO*. (b) Height vs length profile measured for one nanoparticle obtained from (a). (c) Histogram of height distribution for *AgTNPs/GO*. (d) Histogram of length distribution for *AgTNPs/GO*.

AFM characterization helped to clarify the issues caused by the limited resolution observed in the SEM micrographs. Histograms obtained from AFM show better resolution therefore nanoparticle size measurements have less error than histograms obtained from SEM, consequently, SEM allowed us to observe the shape of the largest *AgCNMPs*, while AFM characterization allowed us to measure their sizes.

6.3 Fourier Transform Infrared spectroscopy (FTIR)

Figure 6.10 exhibits the FTIR spectrum of *GO* which shows the characteristic absorption bands obtained using this technique. The band at 2915 cm^{-1} suggests the presence of strong and broad *O – H* stretching vibrations¹³⁵, close to this band, a medium *C – H* stretching vibrations represented by 2854 cm^{-1} is observed¹³⁶ as seen in Table 6.2. Next, a shoulder band is exhibited at 2348 cm^{-1} related to strong *O = C = O* stretching vibrations¹³⁷. Also, a band around 2108 cm^{-1} confirms the weak *C ≡ C* stretching vibrations existing in the *GO* lattice¹³⁸ as shown in Table 6.2. After, two subsequent bands in 1700 cm^{-1} , 1560 cm^{-1} , and a shoulder in 1462 cm^{-1} are shown, corresponding to strong *C = O* stretching vibrations¹³⁹, *C – OH* bending vibrations¹³⁹, and an *O – H* deformation¹²³ respectively as seen in Table 6.2. Finally, the absorption band present in 1163 cm^{-1} associated with strong *C – O – H* vibrations are observed¹⁴⁰, and the band at 715 cm^{-1} suggesting the existence of medium *C – H* alkanes vibrations¹³⁸ as is observed in Table 6.2.

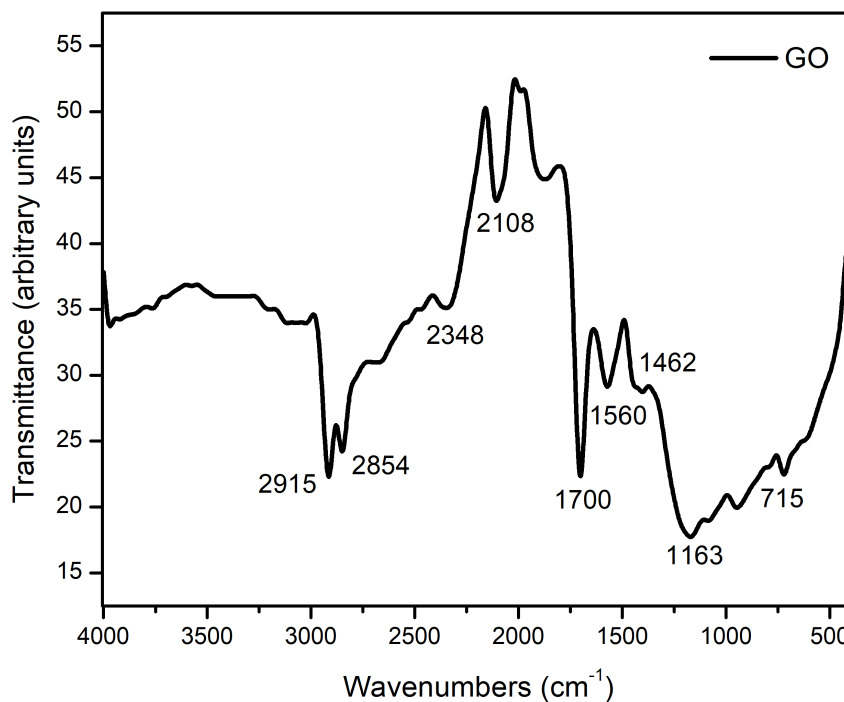


Figure 6.10: FTIR spectrum of graphene oxide (*GO*).

In Figure 6.11 the FTIR spectra of *AuNPs/GO*, *AuCNPs/GO*, *AgNPs/GO* and *AgTNPs/GO* are showed. The

spectrum obtained is the same for each type of nanoparticle, due to the use of the same reagents during the synthesis process, except $HAuCl_4$ and $AgNO_3$, gold and silver precursors to be reduced, therefore, previous FTIR analysis of these chemical compounds will be studied.

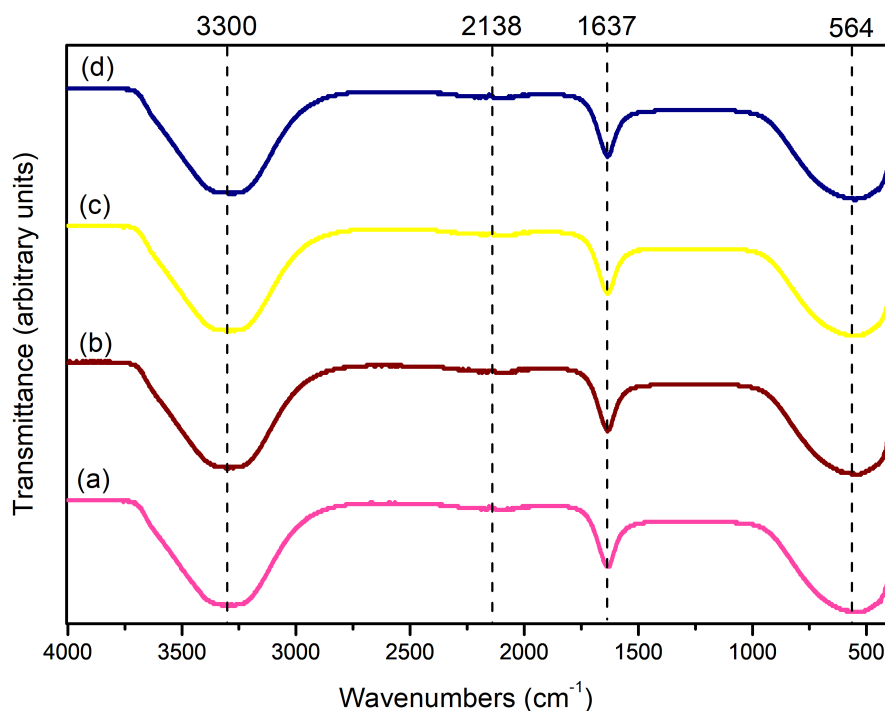


Figure 6.11: FTIR analysis of (a) $AuNPs/GO$. (b) $AuCNPs/GO$. (c) $AgNPs/GO$. (d) $AgTNPs/GO$.

FTIR spectra of $AuNPs/GO$ and $AuCNPs/GO$ samples are distinguished in Fig. 6.11 (a) and 6.11 (b) respectively. Absorption peak at 3300 cm^{-1} was assigned to strong $O-H$ stretching vibration of hydroxyl group¹⁴¹. The next peak around 2138 cm^{-1} lies in the region of strong $C-H$ stretching vibration¹⁴², The absorption peak observed in 1637 cm^{-1} corresponds to $C=O$ strong stretching vibration¹⁴¹, The last peak observed at 564 cm^{-1} is related to $N-H$ bending vibrations¹⁴³ as seen in Table 6.2. In the same way, FTIR spectra of $AgNPs/GO$ and $AgTNPs/GO$ solutions are observed in Fig. 6.11 (c) and 6.11 (d) respectively. The absorption peak at 3300 cm^{-1} was assigned to the strong and broad $O-H$ stretching vibration, the second is observed at 2138 cm^{-1} associated to weak $C-H$ stretching vibrations, the third peak at 1637 cm^{-1} corresponding to medium $N-H$ bending vibration of amine group¹⁴⁴, and the last one centered in 564 cm^{-1} related to strong $-C\equiv C-H$ stretching vibrations which $C-H$ bend is near to 600 cm^{-1} covered by the broad absorption peak as is shown in Table 6.2. Several wavenumbers exposed before, appear in the FTIR spectrum of $AgNO_3$ reagent reported in literature¹⁴⁵. High absorption exhibited

by peaks related to hydrogen vibrations might confirm the reduction of metallic gold and silver ions which allows the formation of nanoparticles¹⁴².

Sample	Approximate Wavenumber (cm^{-1})	Description
<i>GO</i>	2915	Strong and broad <i>O – H</i> stretching vibrations ¹³⁵
	2854	Medium <i>C – H</i> stretching vibrations ¹³⁶
	2348	Strong <i>O = C = O</i> stretching vibrations ¹³⁷
	2108	Weak <i>C ≡ C</i> stretching vibrations ¹³⁸
	1700	Strong <i>C = O</i> stretching vibrations ¹³⁹
	1560	<i>C – OH</i> bending vibrations ¹³⁹
	1462	<i>O – H</i> deformation ¹²³
	1163	Strong <i>C – O – H</i> vibrations ¹⁴⁰
	715	Medium <i>C – H</i> alkanes vibrations ¹³⁸
<i>AuNPs/GO</i> and <i>AuCNP/GO</i>	3300	Strong <i>O–H</i> stretching vibration of hydroxyl group ¹⁴¹
	2138	Strong <i>C – H</i> stretching vibration ¹⁴²
	1637	Strong <i>C = O</i> stretching vibration ¹⁴¹
	564	<i>N – H</i> bending vibrations ¹⁴³
<i>AgNPs/GO</i> and <i>AgTNP/GO</i>	3300	Strong and broad <i>O – H</i> stretching vibration ¹⁴⁴
	2138	Weak <i>C – H</i> stretching vibrations ¹⁴⁴
	1637	Medium <i>N – H</i> bending vibration of amine group ¹⁴⁴
	564	Strong <i>–C ≡ C – H</i> stretching vibrations ¹⁴⁵

Table 6.2: FTIR absorption peaks position of *GO*, *AuNPs/GO*, *AuCNP/GO*, *AgNPs/GO* and *AgTNP/GO* nanocomposites.

6.4 Raman spectroscopy

Raman spectroscopy was performed to analyze the surface-enhanced Raman scattering (SERS) effect caused by the metal plasmons on the surface of gold and silver nanoparticles and the vibrational states of *GO*. This technique provides evidence of defects in the structure, informs about the influence of size and shape on sensing, and analyzes the reduction features of materials¹⁴⁶.

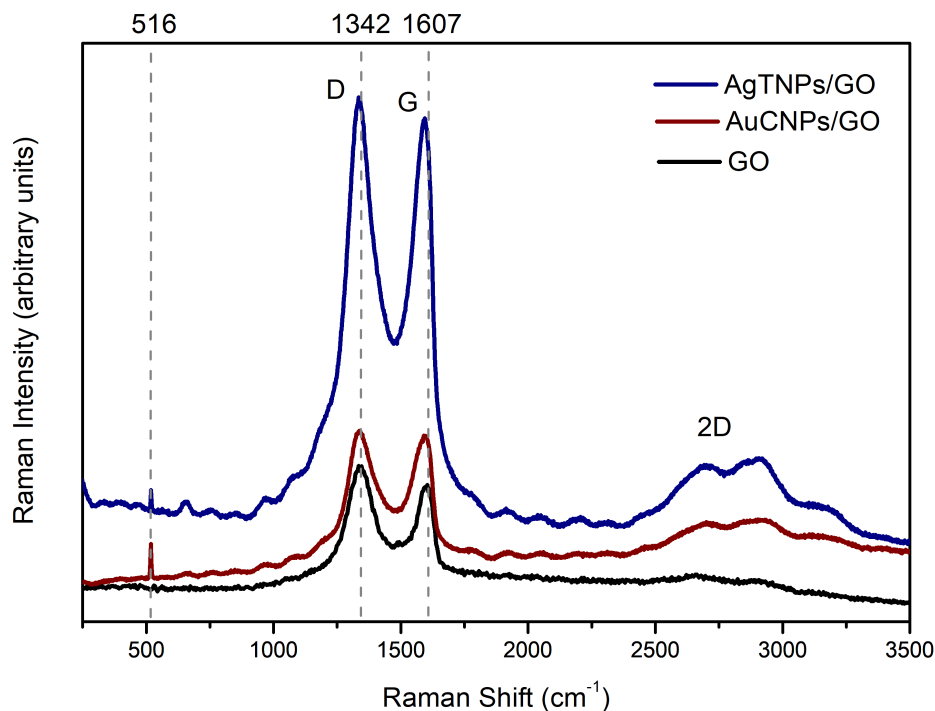


Figure 6.12: Raman spectra of dispersed *GO* solution, *AuCNPs/GO*, and *AgTNPs/GO* nanocomposites excited with 532 nm laser.

The Raman spectrum recorded for the *GO* solution is shown in Figure 6.12, the first peak is observed in 1342 cm^{-1} assigned to D band which is related to out of plane vibrations attributed to the presence of defects in sp^2 -hybridized carbon, and the second in 1607 cm^{-1} associated to G band corresponding to the first-order scattering of the E_{2g} mode¹⁴⁷ as shown in Table 6.3. The same peaks are observed in Fig. 6.12 for *AuCNPs/GO* and *AgTNPs/GO* nanocomposites, but D and G intensities are enhanced with respect to the *GO* solution as seen in Table 6.3. The introduction of *Au* or *Ag* on *GO* causes the increasing of band intensities due to the high electromagnetic fields inside nanoparticles which causes surface-enhanced Raman scattering effect¹²³. Also, a broad 2D band around 2689 cm^{-1} is observed in Raman spectra of *AuCNPs/GO* and *AgTNPs/GO* which is associated with the thickness of *GO*, confirming the presence of few-layer graphene oxide as shown in AFM characterization. Additionally, a band around 516 cm^{-1} appears for *AuCNPs/GO* and *AgTNPs/GO*, which corresponds to *metal – O* vibration. Usually, the Raman shift over the range of $300\text{--}900\text{ cm}^{-1}$ is identified for metal nanocomposites¹⁴⁸. Defects on the samples are analyzed using the intensity ratio of I_D/I_G , Table 6.3 indicates that the intensity ratio is higher for the *GO* solution than *AuCNPs/GO* and *AgTNPs/GO*. Although including *Au* and *Ag* nanoparticles on *GO* means including more defects to its structure, nanoparticles may fulfill the isolated bonds from *GO* to oscillate at a coherent frequency,

generating order vibrations, and reducing the ratio of defects. Finally, the effect of size and shape of nanoparticles in sensing is confirmed by the large difference in intensity between the spectra of *AuCNPs/GO* and *AgTNPs/GO* exhibited in Fig. 6.12. Previous characterizations indicated that *AuCNPs/GO* and *AgTNPs/GO* samples differ in size, having *AuCNPs* structures larger than *AgTNPs*, but *AuCNPs* and *AgTNPs* conserved the planar faces. AFM suggest that the photochemical synthesis generates planar faces. This analysis confirms that the size and shape of the nanoparticles affects the signal generated by Raman spectroscopy, therefore the smaller the structure of the nanoparticles, the greater intensity will be observed in the spectrum, as in the case of *AgTNPs/GO* nanocomposite which sizes were demonstrated to be smaller than *AuCNPs* by SEM characterization technique.

Sample	Raman Shift (cm^{-1})	Description	D (cm^{-1})	G (cm^{-1})	I_D/I_G
<i>GO</i>	1342	D band corresponds to out of plane vibrations attributed to the presence of defects in the sp^2 -hybridized carbon ¹²³	1342	1607	1.13
	1607	G band related to first-order scattering of the E_{2g} mode ¹²³			
<i>AuCNPs/GO</i>	516	Band corresponding to <i>metal – O</i> vibration ¹⁴⁸	1332	1607	1.04
	1334	D band corresponding to vibrations of sp^3 carbon atoms ¹⁴⁹			
	1607	G band related to vibrations of sp^2 carbon atoms ¹⁴⁹			
	2689	2D bands associated with the thickness of <i>GO</i> ¹⁴⁶			
<i>AgTNPs/GO</i>	516	Band corresponding to <i>metal – O</i> vibration ¹⁴⁸	1332	1607	1.04
	1335	D band related with imperfections corresponding to hydroxyl and epoxide groups in carbon ¹⁴⁶			
	1607	G band corresponds to the E_{2g} phonon of sp^2 carbon atoms ¹⁴⁶			
	2689	2D bands associated with the thickness of <i>GO</i> ¹⁴⁶			

Table 6.3: Description of Raman bands of *GO*, *AuCNPs/GO* and *AgTNPs/GO*.

6.5 Electrochemical analysis

6.5.1 Cyclic Voltammetry (CV)

The electrochemical behavior of gold and silver nanocomposites ($AuNPs/GO$, $AuCNP_s/GO$, $AgNPs/GO$, $AgTNP_s/GO$) on the surface of a graphite electrode (GE) was studied by cyclic voltammetry. Figure 6.13 (a) exhibits the cyclic voltammograms of modified graphite (Gra) electrodes with $AuNPs/GO$ and $AuCNP_s/GO$ in an aqueous 1 wt % $NaCl$ solution. Within the studied electrochemical window, which is fairly similar for both samples, no oxidation or reduction peaks due to a redox reaction of the nanocomposites are shown, which can suggest the high stability of gold nanoparticles. In the same way, Figure 6.13 (b) shows the cyclic voltammograms of modified GEs with $AgNPs/GO$ and $AgTNP_s/GO$ in the same electrolyte. The profile for $AgNPs/GO - GE$ exhibits an oxidation peak around -0.11 V, lower than the oxidation peak observed for $AgTNP_s/GO - GE$ a little shifted to -0.10 V which indicates that $AgTNP_s/GO - GE$ is more stable than $AgNPs/GO - GE$. Also, the difference in the magnitude of peak current demonstrates the shape-dependence of the electrochemical behavior, having enhanced properties for $AgTNP_s/GO - GE$ related with the stability of the material²⁵, but it is also observed the most significant signal generated by this electrode which implies unfavorable bigger oxidation than $AgNPs/GO - GE$. Modified electrodes with $AgNPs/GO$ and $AgTNP_s/GO$ indicate irreversible reactions due to the oxidation of Ag to Ag^+ , no reduction peaks are observed. The deposition of high surface area nanocomposites on the surface of graphite electrodes generates an electrochemical capacitor which is based on the electrical charge storage at the surface-electrolyte interface, also called as electric double-layer capacitor. Figure 6.13 shows that the capacitance increases for electrodes modified with $AuCNP_s/GO$ and $AgTNP_s/GO$, because the width of their profiles are bigger than GEs modified with $AuNPs/GO$ and $AgNPs/GO$. This important fact demonstrates that the capacitance of GEs depends on the geometry of the nanoparticles. Section 6.2.2 indicates that $AuCNP_s/GO$ and $AgTNP_s/GO$ generate planar faces, while $AuNPs/GO$ and $AgNPs/GO$ have quasi-spherical shapes. Therefore, planar faces structures provide an increase in the capacitance of GEs more than quasi-spherical shapes.

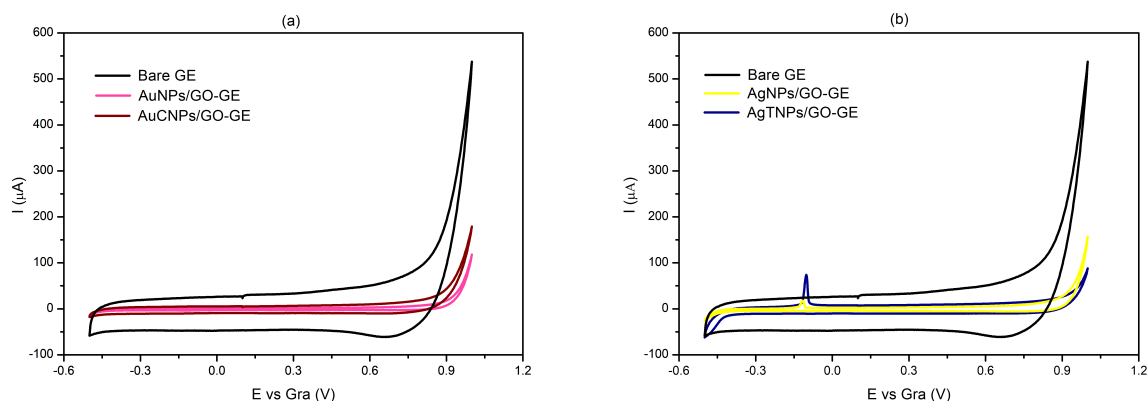


Figure 6.13: Cyclic voltammograms of modified graphite electrodes with nanocomposites in an aqueous 1wt. % $NaCl$ electrolyte with a scan rate of $100 \frac{mV}{s}$. (a) CV of $AuNPs/GO$, and $AuCNPs/GO$ modified GE . (b) CV of $AgNPs/G$, and $AgTNPs/GO$ modified GE .

The redox behavior of the $Fe(CN)_6^{3-/4-}$ redox pair at a bare graphite electrode and modified graphite electrodes with nanocomposites is distinguished in Figure 6.14. The response for the redox reaction between $Fe(CN)_6^{3-/4-}$ and the surface of graphite electrodes exhibits a reversible electrochemical behavior with a peak separation of about 80 mV and a ratio of anodic to cathodic peak currents of about 1. Figure. 6.14 (a) shows the redox behaviour of 2.5 mM $K_3[Fe(CN)_6]$ in 0.1 M KCl at bare graphite electrode ($Bare-GE$) and modified graphite electrodes with $AuNPs/GO$ ($AuNPs/GO-GE$) and $AuCNPs/GO$ ($AuCNPs/GO-GE$) nanocomposites. The electron transfer process effect is revealed in the curves, where the magnitudes of redox current at $AuNPs/GO-GE$ and $AuCNPs/GO-GE$ is higher than those at the bare graphite electrode. This fact demonstrates that the modified electrodes enhance the redox current response because there are conductive nanocomposites on the surface of the electrode facilitating charge transfer¹⁶. In addition, the oxidation and reduction peaks of $AuNPs/GO-GE$ show a higher redox response than $AuCNPs/GO-GE$ which can be attributed to the substrate concentration in the electrode surface, therefore $AuNPs/GO-GE$ could presents the highest concentration¹⁵⁰ which can be attributed to the dependence of the surface deposition of the nanocomposite on the shape of the nanoparticles, having the quasi-spherical shapes better adherence on the electrode surface. Similar behavior is observed for cyclic voltammograms recorded to $AgNPs/GO-GE$, and $AgTNPs/GO-GE$ as observed in Figure. 6.14 (b), where the magnitude of redox current at $AgNPs/GO-GE$ and $AgTNPs/GO-GE$ is higher than those at the bare graphite electrode.

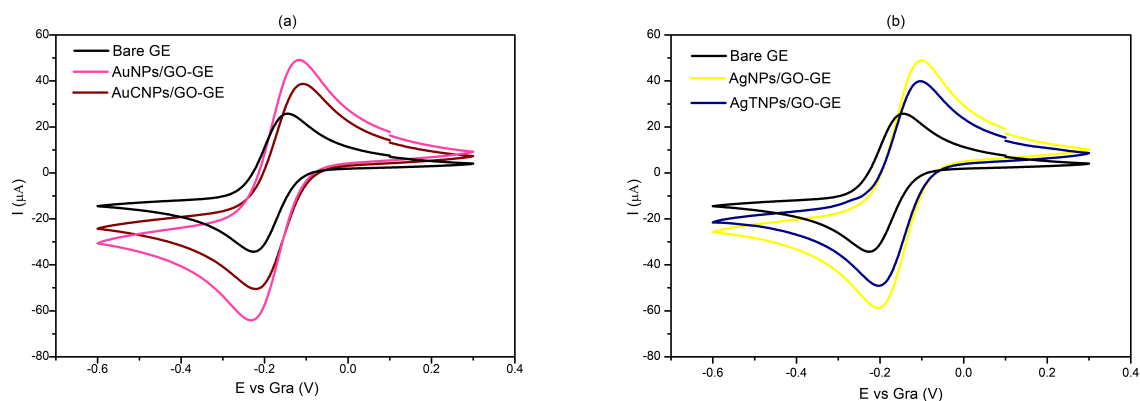


Figure 6.14: Cyclic voltammograms recorded of 2.5 mM $K_3[Fe(CN)_6]$ in 0.1 M KCl at modified graphite electrodes with nanocomposites using a scan rate of $50 \frac{mV}{s}$. (a) Bare graphite electrode, $AuNPs/GO$, and $AuCNPs/GO$ modified GE . (b) Bare graphite electrode, $AgNPs/GO$, and $AgTNPs/GO$ modified GE .

To study the diffusion behavior of the nanocomposite modified electrodes, cyclic voltammograms were recorded for 2.5 mM of $K_3[Fe(CN)_6]$ at 10, 25, 50, 100, 150, 200 $\frac{mV}{s}$, as exhibited in Figure 6.15. The analysis is done through the Randles-Sevcik equation which relates the position of anodic and cathodic peaks with the square root of the scan rate ν as is shown in equation 5.1. Figures 6.15 (a), (b), (c), and (d) show the cyclic voltammograms recorded of 2.5 mM $K_3[Fe(CN)_6]$ in 0.1 M KCl at modified GE with $AuNPs/GO$, $AuCNPs/GO$, $AgNPs/GO$, and $AgTNPs/GO$ respectively which reveal that oxidation peaks for each modified electrode tend to positive shift while the scan rate increases, also a negative shift of the reduction peaks is observed. Consequently, the peak potential separation increases with the increase of the scan rate. In general, the peak current values are directly proportional to scan rate values, namely, in all samples is observed that the magnitude of oxidation and reduction peaks current increases while the scan rate increases as seen in Fig. 6.16. In addition, $AuNPs/GO$, $AuCNPs/GO$, $AgNPs/GO$, and $AgTNPs/GO$ modified electrodes suggest a reversible behavior, and also the peak currents are dependent of the shapes of the nanoparticles. As for gold nanoparticles, Fig. 6.15 (a) shows the analysis of $AuNPs/GO - GE$, where the signals of peak current is in a the smallest range than those for $AuCNPs/GO - GE$ as observed in Fig. 6.15 (b), concerning to silver nanoparticles, Fig. 6.15 (c) and Fig. 6.15 (d) also reveals that the signal of peak current is less intense for $AgNPs/GO - GE$ than for $AgTNPs/GO - GE$. Fig. 6.15 (a) and Fig. 6.15 (c) show the cyclic voltammograms recorded at modified electrodes with spherical-shaped gold and silver nanoparticles, as suggested in Section 6.1, while in Fig. 6.15 (b) and Fig. 6.15 (d), the redox response at modified electrodes with planar faces structures is observed. The peak current separation (ΔE_p) also shows a dependence in the shape of the nanoparticles, given the smaller values for planar faces structures ($AuCNPs/GO - GE$ and $AgTNPs/GO - GE$) as is observed in Table 6.6. Therefore, it could be suggested that the signal intensity improves for those electrodes modified with more planar faces on their structures.

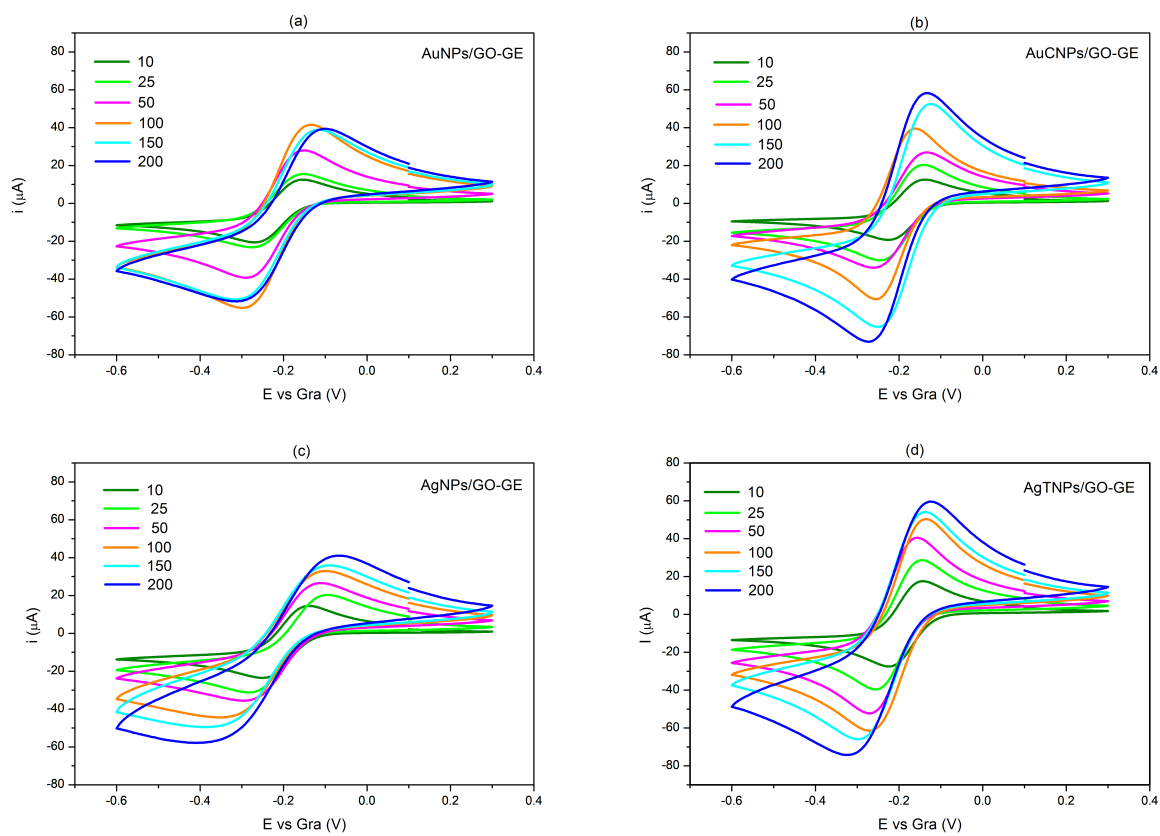


Figure 6.15: Cyclic voltammograms recorded for 2.5 mM of $\text{K}_3[\text{Fe}(\text{CN})_6]$ at different scan rates: 10, 25, 50, 100, 150, 200 $\frac{\text{mV}}{\text{s}}$. (a) AuNPs/GO modified GE. (b) AuCNPs/GO-GE. (c) AgNPs/GO-GE. (d) AgTNPs/GO-GE.

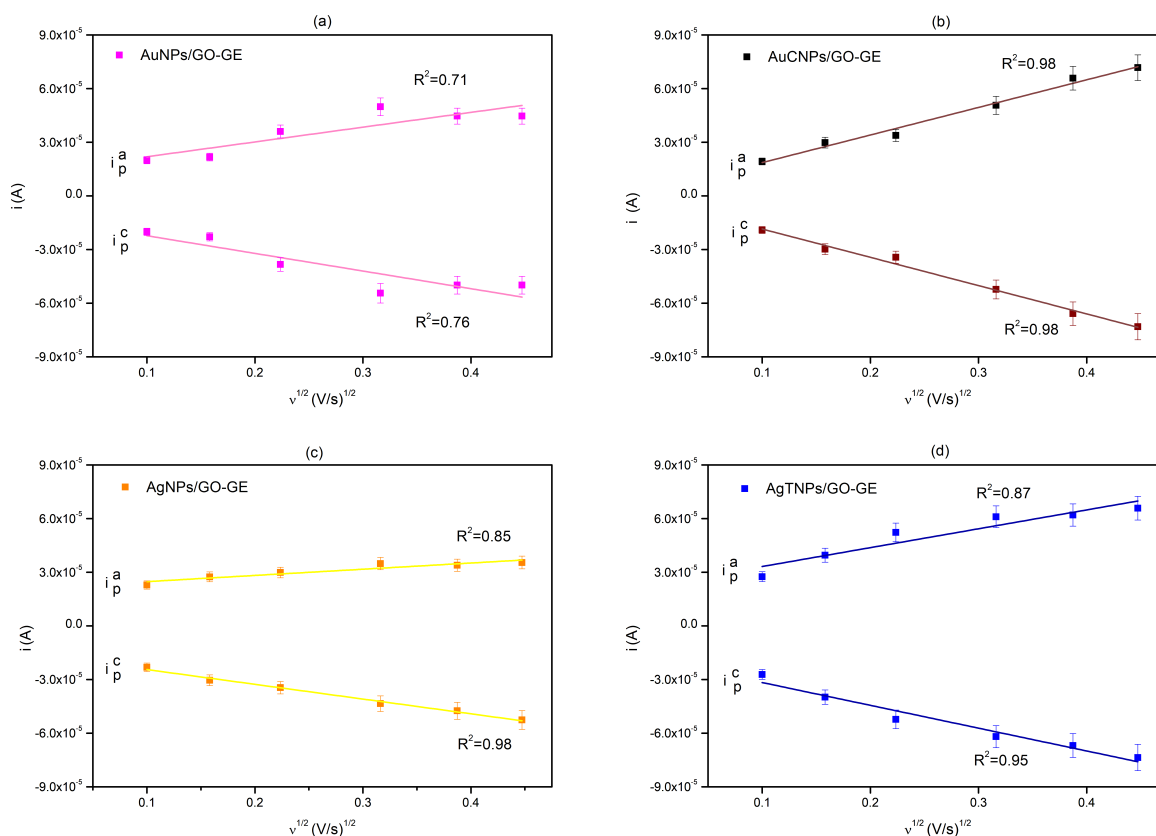


Figure 6.16: Plots of current (i) against square root of scan rate (v) for anodic and cathodic peaks extracted from Fig. 6.15. (a) $AuNPs/GO$ modified GE . (b) $AuCNPs/GO - GE$. (c) $AgNPs/GO - GE$. (d) $AgTNP/GO - GE$.

Diffusion Coefficients

After extracting the values of anodic peak (i_p^a) and cathodic peak (i_p^c), the graphs of i against $v^{1/2}$ are plotted for $AuNPs/GO - GE$, $AuCNPs/GO - GE$, $AgNPs/GO - GE$, and $AgTNP/GO - GE$ using equation 5.2 as shown in Fig. 6.16. By manipulating equation 5.1, the diffusion coefficients can be obtained from the slope of the lineal representation of i against $v^{1/2}$ observed in Fig. 6.16. Table 6.4 shows the calculated diffusion coefficient for the oxidized and reduced form of the redox probe generated during the cyclic voltammetry measurements*. All obtained values are in the range of $10^{-7} \frac{cm^2}{s}$ and $10^{-8} \frac{cm^2}{s}$ indicating that there is no specific influence of the shapes or sizes of NPs on the diffusion process. Although the influence of nanoparticles on the diffusion coefficient is similar for all modified electrodes, in some cases higher coefficients can be expected for nanocomposite-based electrode

*To reduce noise and measurement error, it is recommended to repeat some measurements, which could not be performed due to the pandemic restrictions.

surfaces. For example, research made using chronoamperometric techniques determined a diffusion coefficient of $4.24 \times 10^{-6} \frac{cm^2}{s}$ at carbon electrodes in 1 mM potassium ferricyanide and 0.1 M phosphate buffer¹²², which suggests together with other sources^{151 152 153} that the values in Table 6.4 are lower than those in the literature. Although D depends mainly on the redox species, the effect of the electrode in the measurements cannot be discarded, perhaps an adsorption effect on the electrode surface could cause effects on D , as suggested by Radhi *et al*¹⁵⁴, where a diffusion coefficient of $7.6 \times 10^{-6} \frac{cm^2}{s}$ was determined at 1 mM $K_3[Fe(CN)_6]$ in $KClO_4$ at a glassy carbon electrode while the value change to $7.2 \times 10^{-7} \frac{cm^2}{s}$ when the same GC is modified with polymers¹⁵⁵. Finally, a linear tendency is observed in the redox peak current of all samples, suggesting that the mass transfer in the surface of the electrode is a diffusion-controlled mechanism^{156 157}.

Modified Electrode	Anodic		Cathodic	
	$D^a \left(\frac{cm^2}{s} \right)$	R ²	$D^c \left(\frac{cm^2}{s} \right)$	R ²
AuNPs/GO – GE	1.35E-07	0.71	1.92E-07	0.76
AuCNPs/GO – GE	4.71E-07	0.98	4.95E-07	0.98
AgNPs/GO – GE	2.38E-08	0.85	1.34E-07	0.87
AgTNPs/GO – GE	2.20E-07	0.98	3.21E-07	0.95

Table 6.4: Diffusion coefficients calculated for anodic and cathodic peaks of graphite electrodes modified with AuNPs/GO, AuCNPs/GO, AgNPs/GO, and AgTNPs/GO.

Standard Rate Constant k^0

The analysis of the reversibility of the electrochemical system was made through the calculation of the standard rate constants for AuNPs/GO, AuCNPs/GO, AgNPs/GO, and AgTNPs/GO modified electrodes. The methodology used for the calculations was presented in Section 5.3.3. Equation 5.5 relates the transfer coefficient (α) with the anodic and cathodic peaks and the half-potential. The values of α calculated for measurements in 2.5 mM of $K_3[Fe(CN)_6]$ electrolyte using AuNPs/GO, AuCNPs/GO, AgNPs/GO, and AgTNPs/GO modified electrodes are shown in Table 6.5. Most α values follow the Nicholson criterion of independence of the peak potential separation ΔE_p in respect to the transfer coefficient α , as they lie within a range of around $0.3 < \alpha < 0.7$, therefore k^0 could be calculated using equations 5.3 and 5.4.

GE	AuNPs/GO		AuCNPs/GO		AgNPs/GO		AgTNPs/GO	
	α^a	α^c	α^a	α^c	α^a	α^c	α^a	α^c
10	0.69	0.60	0.73	0.75	0.76	0.60	0.80	0.75
25	0.69	0.57	0.84	0.63	0.62	0.58	0.71	0.74
50	0.69	0.54	0.68	0.63	0.59	0.54	0.72	0.67
100	0.61	0.55	1.12	0.63	0.55	0.34	0.70	0.63
150	0.56	0.48	0.72	0.60	0.51	0.34	0.66	0.49
200	0.52	0.43	0.70	0.61	0.50	0.27	0.60	0.50

Table 6.5: Charge transfer coefficient α calculated for anodic and cathodic peaks of AuNPs/GO, AuCNPs/GO, AgNPs/GO, and AgTNPs/GO graphite electrodes.

As described in Section 5.3.3, the kinetic parameter is obtained using the equation 5.4 and ΔE_p values shown in Table 6.6. Additionally, the data of ΔE_p extracted from cyclic voltammograms indicates a quasi-reversible process for all modified electrodes because the peak potential separation is characterized by $\Delta E_p > \frac{59.2}{n}mV$ as predicted theoretically¹¹⁶.

Scan rate ($\frac{mV}{s}$)	$\Delta E_p(mV)$			
	AuNPs/GO – GE	AuCNPs/GO – GE	AgNPs/GO – GE	AgTNPs/GO – GE
10	117	88	110	82
25	121	102	187	110
50	135	125	176	115
100	163	97	234	132
150	193	124	281	157
200	209	135	337	193

Table 6.6: Peak potential separation ΔE_p for 2.5 mM of $K_3[Fe(CN)_6]$ at AuNPs/GO, AuCNPs/GO, AgNPs/GO, and AgTNPs/GO modified electrodes at different scan rates.

Finally, equation 5.3 allows obtaining the linear relationship of ψ vs $Y\nu^{-1/2}$ as shown in Figure 6.17, from which the standard rate constant k^0 can be obtained as described in Section 5.3.3. Figure 6.17 (a) and 6.17 (b) show different slopes for each sample but also different dimensions of the length in the data of the linear fitting, which indicates the variation of anodic constant Y^a and cathodic constant Y^c for each modified electrode. Data of Y constant and k^0 for anodic and cathodic peaks are observed in Table 6.7.

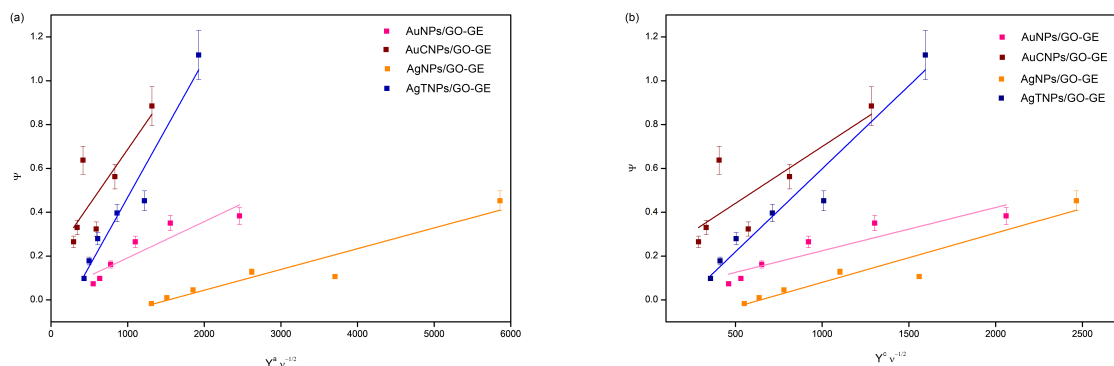


Figure 6.17: Plots of ψ vs $Yv^{-1/2}$ for the system 2.5 mM of $K_3[Fe(CN)_6]$ on $AuNPs/GO$, $AuCNPs/GO-GE$, $AgNPs/GO-GE$, and $AgTNPs/GO-GE$ graphite modified electrodes. (a) Anodic Analysis (b) Cathodic Analysis.

The experimentally determined values of standard rate constant k° are in the order of magnitude of $10^{-4} \text{ cm s}^{-1}$ mainly, in agreement with the literature where k° was calculated using the same calculations at carbon electrodes in 1 mM potassium ferricyanide and 0.1 M phosphate buffer¹²². The biggest values of k° are observed for $AgNPs/GO-GE$, $AgTNPs/GO-GE$ as is shown in Table 6.7 which indicates that the speed of the electron transfer between the nanocomposite modified electrode surface and the electroactive species of the electrolyte is faster for electrodes modified with Ag than Au^{115 158}.

Sample	Anodic			Cathodic		
	$Y^a (\text{cm}^2/\text{sV})^{-1/2}$	$k^\circ (\frac{\text{cm}}{\text{s}})$	$\pm \text{Error} (\frac{\text{cm}}{\text{s}})$	$Y^c (\text{cm}^2/\text{sV})^{-1/2}$	$k^\circ (\frac{\text{cm}}{\text{s}})$	$\pm \text{Error} (\frac{\text{cm}}{\text{s}})$
AuNPs/GO-GE	246.06	1.65E-04	3.54E-05	206.00	1.97E-04	4.23E-05
AuCNPs/GO-GE	131.69	5.05E-04	1.74E-04	128.41	5.18E-04	1.79E-04
AgNPs/GO-GE	585.95	9.46E-05	1.45E-05	246.54	2.25E-04	3.45E-05
AgTNPs/GO-GE	192.64	6.27E-04	7.05E-05	159.49	7.58E-04	8.51E-05

Table 6.7: Standard Rate Constant K° and the respective Y constant calculated for $AuNPs/GO$ modified GE , $AuCNPs/GO-GE$, $AgNPs/GO-GE$, and $AgTNPs/GO-GE$ at anodic and cathodic peaks.

Electrocatalytic reduction of H_2O_2

Ag-Based Nanocomposite Electrodes

Modified surface electrodes with gold and silver nanostructures promise to fabricate sensors with improved electrocatalytic properties for ultrasensitive sensor materials. The electrocatalytic response of H_2O_2 was studied at $AgNPs/GO$ and $AgTNPs/GO$ modified GE through observations on the cyclic voltammetric reduction of different concentrations of H_2O_2 in 0.1 M phosphate buffer at a pH of 7.2. Figure. 6.18 (a) confirms that the buffer solution in

absence of H_2O_2 does not show any non-analyte related redox signals for $AgNPs/GO-GE$ and $AgTNPs/GO-GE$. In Fig. 6.18 (b) a comparison between measurements at $AgNPs/GO-GE$ using the pure buffer in absence of H_2O_2 (in black) and with small additions of H_2O_2 to the buffer is observed. The signal of H_2O_2 is identified as a reduction current response which is generated for concentrations between $800\mu M$ and $6mM$. The reduction peak potential in the smallest concentration ($800\mu M$) is identified around $-1.40 V$ vs *Gra*, which shifts to the negatives while the concentration of H_2O_2 increases, thus the peak potential in the highest concentration ($6mM$) is observed around $-1.60 V$ vs *Gra* indicating the increase of the electrocatalytic effect with the increase of the concentration of H_2O_2 . The inset observed in Fig. 6.18 (b) shows the plot of the peak current i vs concentration $[H_2O_2]$ at $AgNPs/GO-GE$ where the peak current increased with the increase in the concentration of $[H_2O_2]$. A fitting of the data was performed which demonstrates the linear dependence of the peak current with the concentration of $[H_2O_2]$. In Fig. 6.18 (c) and Fig. 6.18 (d) the measurements at $AgTNPs/GO-GE$ using the pure buffer in absence of H_2O_2 (in black) and with additions of H_2O_2 to the buffer are observed. $AgTNPs/GO-GE$ shows a larger signal response range than $AgNPs/GO-GE$, therefore, the measurements are presented in two different graphs to better observations of reduction peaks. The reduction current response at $AgTNPs/GO-GE$ is generated between $400\mu M$ and $6mM$ which confirms the enhancement of electron transfer in the surface of $AgTNPs/GO-GE$ due to the effect of the size and shape of the nanoparticles. The reduction peak potential at $400\mu M$ concentration of H_2O_2 has identified around $-1.40 V$ vs *Gra*, then it shifts to the negatives until reaches a value around $-1.60 V$ vs *Gra* at $6mM$ concentration. The i vs $[H_2O_2]$ graph at $AgTNPs/GO-GE$ is shown in the inset inside Fig. 6.18 (c) and Fig. 6.18 (d), which indicates that the i linearly increased with the increase in $[H_2O_2]$. As seen in Fig. 6.18, the electrodes modified with spherical-shaped silver nanocomposites ($AgNPs/GO-GE$) show comparably lower detection currents than ($AgTNPs/GO-GE$), thus suggesting $AgTNPs/GO-GE$ as the more suitable material for enhanced detection. Experiments with bare graphite electrodes showed inferior results compared to the $AgNPs$ modified electrodes. Modified surface electrodes with gold and silver nanostructures promise to fabricate sensors with improved electrocatalytic properties for ultrasensitive sensor materials. Experiments with bare graphite electrodes showed inferior results compared to the $AgNPs/GO$ modified electrodes^{16 †}.

[†]Due to the COVID-19 pandemic-related laboratory restrictions, preliminary measurements could not be finished and are therefore not shown here.

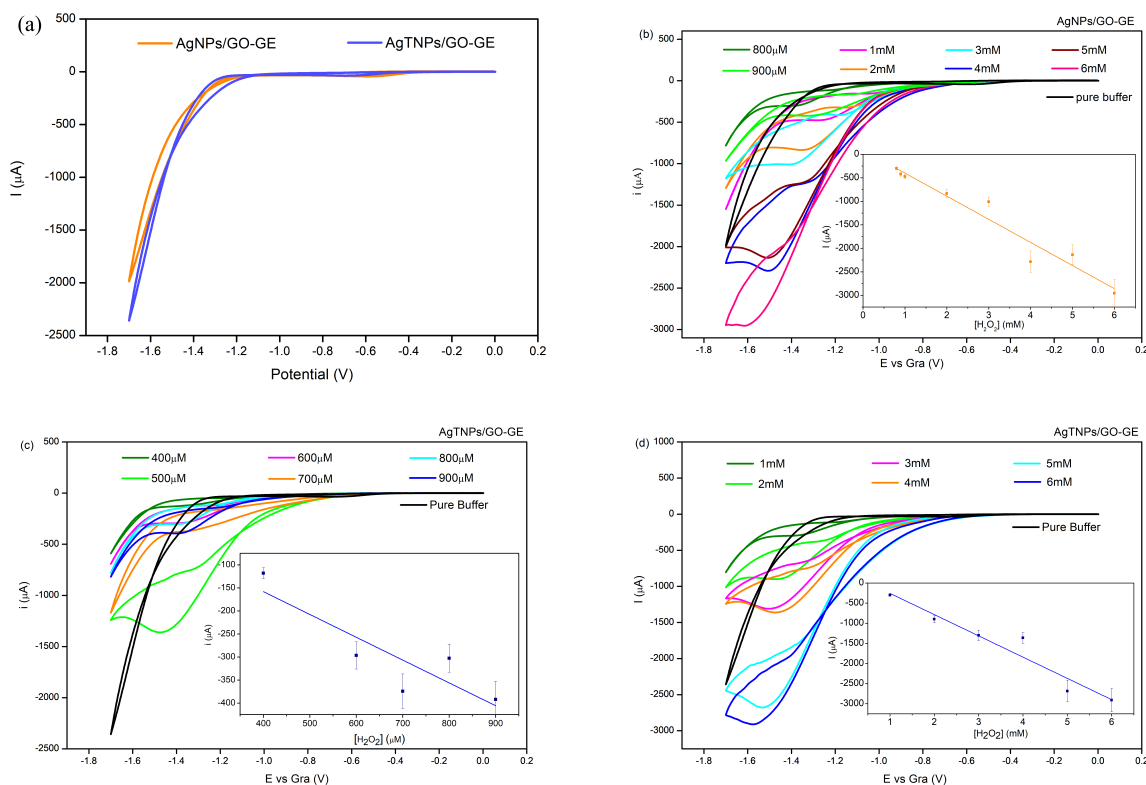


Figure 6.18: Cyclic voltammograms for different concentrations of H_2O_2 in 0.1 M phosphate buffer recorded at a scan rate of $50 \frac{mV}{s}$ at room temperature: (a) Modified Ag-nanocomposite electrodes without H_2O_2 . (b) AgNPs/GO-GE in the presence of H_2O_2 in concentrations between 800 μM to 6 mM. (c) and (d) AgTNPs/GO-GE in the presence of H_2O_2 in concentrations between 300 to 900 μM and 1 to 6 mM, respectively. Insets: Peak current i vs concentration $[H_2O_2]$.

To determine and compare the performance of the AgNPs/GO and AgTNPs/GO nanocomposite modified GEs, an analysis of the sensitivity, limit of detection (LOD), and limit of quantification (LOQ) was made. Sensitivity is calculated as the slope of the linear fit, LOD indicates the lowest analyte concentration that could be detected, and is defined by equation 6.1.

$$LOD = 3 \times \frac{SD}{m} \quad (6.1)$$

LOQ is the lowest analyte concentration detected in the parameters of precision and accuracy, and is given by equation 6.2.

$$LOQ = 10 \times \frac{SD}{m} \quad (6.2)$$

where SD is the standard deviation of the blank, in this case, the extrapolation of the linear regression to zero

concentration is used is used for the calculations as suggested by Look H. *et al*, and m is the slope of the linear regression¹⁵⁹.

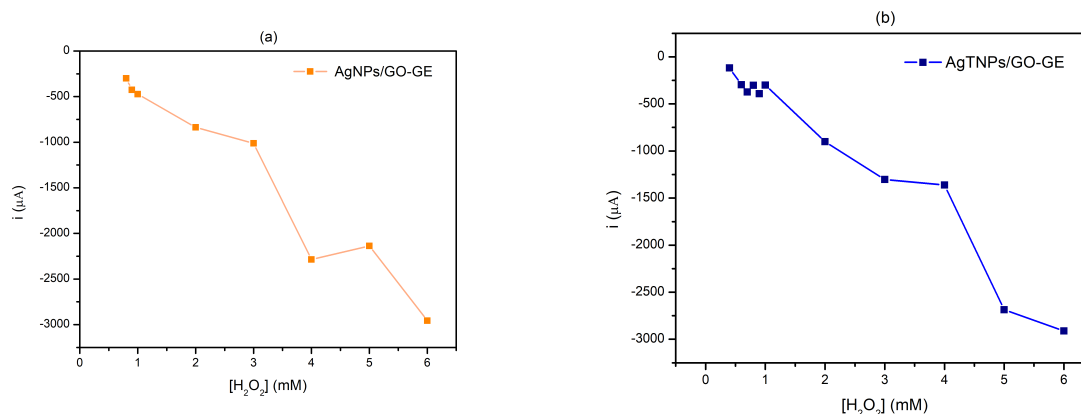


Figure 6.19: Linear regression of peak current i vs concentration of $[H_2O_2]$ to analyze the performance metrics of the nanocomposite-based electrodes. (a) $AgNPs/GO-GE$. (b) $AgTNPs/GO-GE$

Fig. 6.19 shows the current response of $AgNPs/GO-GE$ and $AgTNPs/GO-GE$ to H_2O_2 . Although the sensor based on Ag nanocomposites detects concentrations up to 6 mM, non-linear behavior is observed above 4 mM, therefore those concentrations were not included for the calculation of the sensitivity, LOD and LOQ . Table 6.8 shows the performance metrics calculated for $AgNPs/GO-GE$ and $AgTNPs/GO-GE$, the results indicate that $AgTNPs/GO-GE$ is more sensible than $AgNPs/GO-GE$ by a difference around $134.96 \mu A mM^{-1} cm^{-2}$, consequently, the LOD and LOQ values show that the smallest $[H_2O_2]$ concentrations are detected by $AgTNPs/GO-GE$ as predicted before. The results in Table 6.8 show that $AgTNPs/GO-GE$ is the most sensitive electrode to detect smaller concentrations, which suggest that the shape and size of $AgNPs$ influence the improvement of the detection, in this case $AgTNPs$ with well-defined sizes have demonstrated to be better for these purposes.

Sample	Linearity	Sensitivity	LOD	LOQ	Technique	Ref
<i>AgNPs/GO – GE</i>	0.8-3.0 <i>mM</i>	309.55 μA $mM^{-1} cm^{-2}$	0.68 <i>mM</i>	2.29 <i>mM</i>	CV	This work
<i>AgTNPs/GO – GE</i>	0.4-3.0 <i>mM</i>	444.51 μA $mM^{-1} cm^{-2}$	0.28 <i>mM</i>	0.96 <i>mM</i>	CV	This work
<i>AgNPs</i>	0.005-0.4 <i>mM</i>	0.034 <i>mA</i> $mM^{-1} cm^{-2}$	5.0 μM	–	LSV	[159]
<i>AgNPs@GC</i>	0.005-4.0 <i>mM</i>	0.16 <i>mA</i> $mM^{-1} cm^{-2}$	1.7 μM	–	Amp	[160]
<i>AuNPs</i>	–	52.94 μA $mM^{-1} cm^{-2}$	0.5 μM	–	Amp	[161]

Table 6.8: Performance metrics of the studied *AgNPs/GO* and *AgTNPs/GO* nanocomposite-modified electrodes, and their comparison with sensors based *AgNPs* and *AuNPs* cited in the literature.

Several literature reported the performance metrics for electrochemical sensors using similar modified electrodes with metal nanoparticles. For example, Viswanathan P. *et al* developed a sensor that achieve a sensitivity of $0.034 mA mM^{-1} cm^{-2}$ by using an electrode completely made by *AgNPs*¹⁶⁰, also Yang Z. *et al* calculates a value of $0.16 mM^{-1} cm^{-2}$ using a glassy carbon electrode modified with *Ag* nanoparticles¹⁶¹. In both cases the sensitivity is lower than those obtained in this work as is observed in table 6.8. The limit of detection (*LOD*) of the references are lower than *AgNPs/GO – GE* and *AgTNPs/GO – GE* which could be generated by the higher linear detection produced by the electrodes exposed in the literature. A comparison with *AuNPs* is also observed in the table 6.8, Li S. *et al* suggest a low limit of detection and a sensitivity that could be improve with the enhanced surface area of nanocomposite-based electrodes¹⁶². Results are promising for the study of *Ag*-based electrodes in order to improve their stability, and suggests favorable results in the study of *Au*-based electrodes.

Stability of Nanocomposite Electrodes

Several scans were performed across the potential range between $-1.7V$ and $0V$ to determine the oxidation stability of silver nanoparticles in the system used to study the electrocatalytic reduction of H_2O_2 observed in Fig. 6.20. In

Figures 6.20 (a) and 6.20 (c), $AgNPs/GO$ and $AgTNPs/GO$ modified electrodes were tested in 0.1 M phosphate buffer in absence of H_2O_2 using a scan rate of $50 \frac{mV}{s}$. The stability test was performed by recording 18 consecutive scans at $AgNPs/GO - GE$ in the pure phosphate buffer in absence of H_2O_2 . As the electrodes are not expected to be greatly degraded by the buffer, as consequence, a higher number of scans was chosen to observed changes. In the case of measurements at $AgTNPs/GO - GE$ in the phosphate buffer with H_2O_2 , 9 consecutive scans were made to observe the faster degradation of the electrode in the electrolyte. To visualize changes in the signal response, a percentage decrease in respect to the initial current, $\% \Delta I$, were calculated with each consecutive scan, to simplify the explanation. The difference between the highest and the lowest currents for $AgNPs/GO - GE$, ΔI is $697 \mu A$, while for $AgTNPs/GO - GE$ is exhibit around $\Delta I = 676 \mu A$ in the phosphate buffer in absence of H_2O_2 , demonstrating that the stability of the system is improved with the deposition of high surface area nanocomposites on the electrodes. The last scan (18) at $AgNPs/GO - GE$ shows the peak current around $-1720 \mu A$ while at $AgTNPs/GO - GE$ is observed at $-1920 \mu A$ which reveals the shift to negative currents but maintaining the smallest ΔI . Also, cyclic voltammograms were recorded with $6 \text{ mM } H_2O_2$ (the biggest concentration detected by modified electrodes and a highly oxidative environment) in 0.1 M phosphate buffer. Figure. 6.20 (b), and Figure. 6.20 (d) respectively shows the stability test for $AgNPs/GO - GE$ and $AgTNPs/GO - GE$ respectively. Change in reduction peaks is $\Delta I = 703 \mu A$ for $AgNPs/GO - GE$, and $\Delta I = 544 \mu A$ for $AgTNPs/GO - GE$, which confirms an improvement in the electrode's oxidation resistance for the $AgTNPs/GO - GE$ after the nine scan. As can be seen by comparing the current values of the 9th scan, where at $AgNPs/GO$ and $AgTNPs/GO$ with pure phosphate buffer in absence of H_2O_2 , respectively, the addition of H_2O_2 leads to a faster degradation for the electrodes as previously suggested.

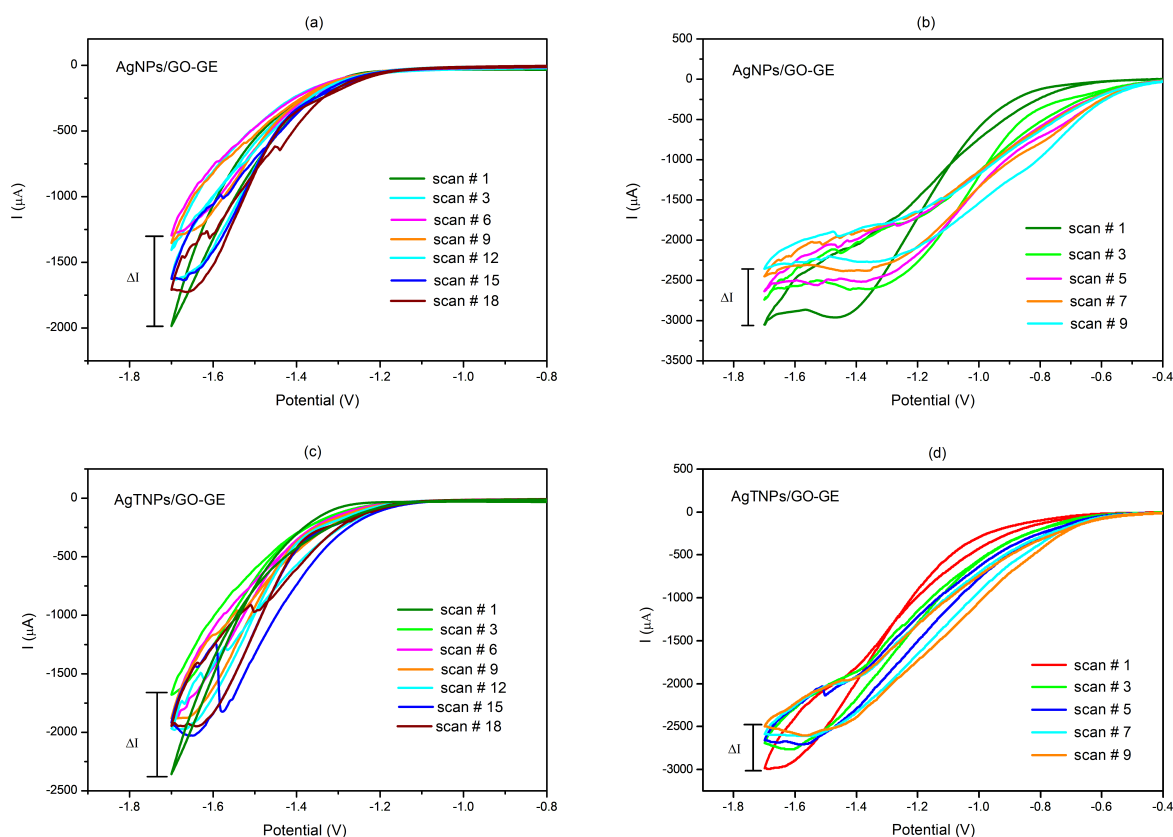


Figure 6.20: Stability test performed by recording several cyclic voltammograms with a scan rate of $50 \frac{mV}{s}$. (a) $AgNPs/GO - GE$ at 0.1 M phosphate buffer in absence of H_2O_2 . (b) $AgNPs/GO - GE$ at 6 mM H_2O_2 in 0.1 M phosphate buffer. (c) $AgTNPs/GO - GE$ at 0.1 M phosphate buffer in absence of H_2O_2 . (d) $AgTNPs/GO - GE$ at 6 mM H_2O_2 in 0.1 M phosphate buffer. Only selected scans are chosen for visibility.

Figure 6.21 shows the representation of the percentual decay that is generated when several scans are recorded for the same electrode. Figure 6.21 (a) represents the scans for $AgNPs/GO - GE$ at 0.1 M phosphate buffer in absence of H_2O_2 . In this case, a maximum decay of -35% is observed in scan number 6. After reaching the maximum decay, an increase in the signal is observed until reaching -10% of the signal generated in the first scan, which occurs around scan number 12, subsequently, the signal tends to stabilize between currents of -10% and -20% of the initially measured value. In Figure 6.21 (b), the current signal for its respective scan number in $AgNPs/GO - GE$ at 6 mM H_2O_2 in 0.1 M phosphate buffer is observed. The current signal decreases following a linear tendency until reaching a decay of -24% . These observations allow us to predict that the decay could be total with a greater number of scan cycles, which makes sense because at some point the small amount of H_2O_2 used for the measurements should be completely consumed, and also could be related with the absence of Ag in the surface of the electrode,

generating a total decrease in the signal. The measurements recorded with $AgTNP_s/GO - GE$ at 0.1 M phosphate buffer in absence of H_2O_2 are shown in Figure 6.21 (c), in this case, the maximum decay signal is observed around -27% for scan number 4. Then the signal increases, reducing the decay to tend to stability between currents of -5% and -15% of the initially measured value. Finally, Figure 6.21 (d) indicates the current signal vs scan number for $AgTNP_s/GO - GE$ at $6\text{ mM } H_2O_2$ in 0.1 M phosphate buffer. In Figure 6.21 (d), the decay shows a linear tendency until decreasing of -15% . Considering the slower decay after 9 cycles of the spherical-shaped $AgNP_s/GO$, a case can be made for the higher stability of the $AgTNP_s/GO$ modified graphite electrodes. The analysis of the percentual decay suggests the stability of $AgTNP_s/GO - GE$ is greater than $AgNP_s/GO - GE$ as the decay is about -29% lower.

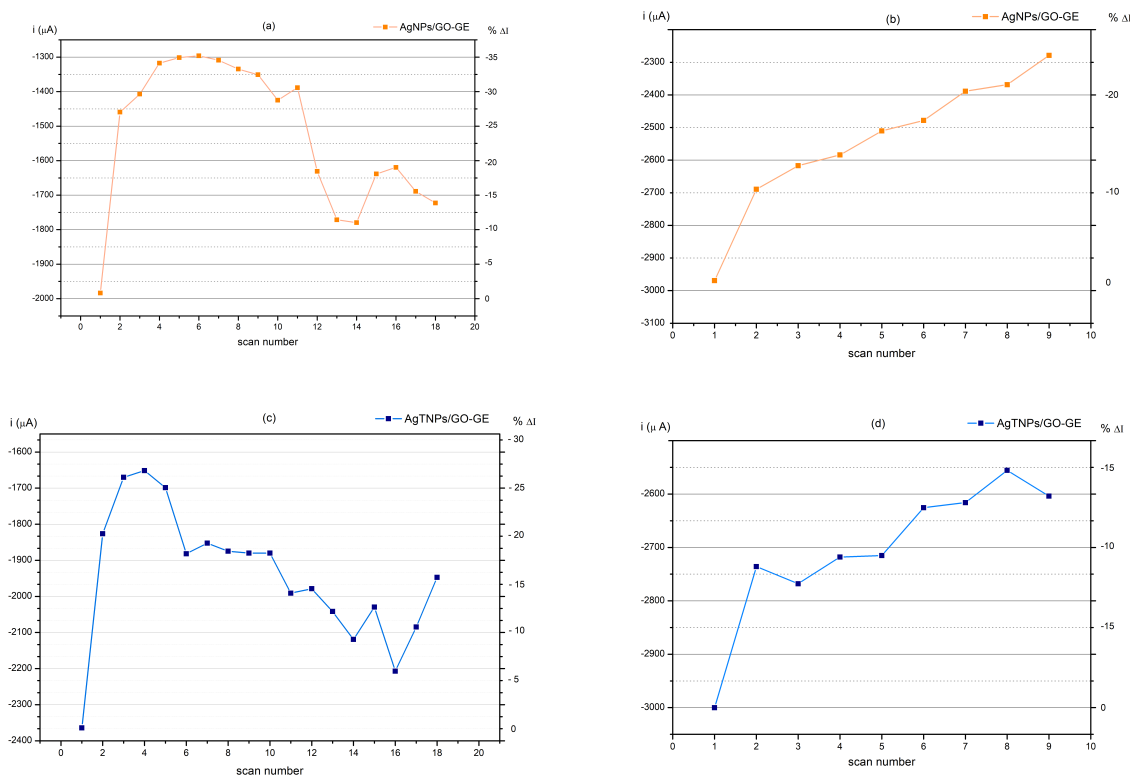


Figure 6.21: Percentual decay of the electrochemical signal as a function of the scan number. (a) $AgNP_s/GO - GE$ at 0.1 M phosphate buffer in absence of H_2O_2 . (b) $AgNP_s/GO - GE$ at $6\text{ mM } H_2O_2$ in 0.1 M phosphate buffer. (c) $AgTNP_s/GO - GE$ at 0.1 M phosphate buffer in absence of H_2O_2 . (d) $AgTNP_s/GO - GE$ at $6\text{ mM } H_2O_2$ in 0.1 M phosphate buffer.

Chapter 7

Conclusions & Outlook

Photochemical reduction of gold and silver nanoparticles was successfully performed, using the photoreduction method. Different characterization techniques demonstrate the improved properties reached. UV-Vis spectroscopy showed that the SPR of *Au* nanoparticles occurs at a shorter wavelength than *Ag*, which influences in the concentration of the formation of well-defined nanostructures. SEM and AFM exhibited the formation of well-defined size nanoparticles for *Ag* and *Au* nanoparticles. Raman spectroscopy allowed the identification of the interaction between graphene and the nanoparticles to demonstrate the stability achieved with this method. The formation of *Ag* and *Au* nanostructures were observed in the SPR absorption spectrum peaks, but always maintaining a planar face that improves the interaction between the surface of nanoparticles and the exposition medium. Furthermore, the results obtained prove that the controlled synthesis of nanoparticles to achieve improved properties does not require the use of expensive equipment.

The deposition of gold and silver nanocomposites with enhanced surface properties on the surface of graphite electrodes was performed to obtain high sensitivity to specific components and a low detection limit. Cyclic voltammetry measurements were recorded to study the surface properties of the electrodes and provide information on the detection capacity of the setup proposed. The electrochemical analysis of diffusion coefficients D^a , D^c , and the standard rate constant k° showed that electrodes modified with nanocomposites exhibit electrode kinetics comparable and superior to similar systems published in the literature in which more sophisticated equipment and expensive procedures are used. Furthermore, the modified electrodes were studied for the electrochemical reduction of H_2O_2 and it was observed that the sensitivity, *LOD* and *LOQ* for *AgTNPs/GO-GE* are superior to *AgNPs/GO-GE*, the results show that in the case of *AgTNPs/GO-GE* the sensitivity is comparable and superior to similar electrodes reported in the literature. Lastly, the redox stability of *AgNPs/GO* and *AgTNPs/GO* modified graphite electrodes was studied in an oxidizing environment, demonstrating that silver nanocomposites having structures with planar faces and small sizes lead to higher stability of the nanocomposites. This home-made and low-cost electrochemical sensor allows fast, precise, sensitive detection using easy-to-use equipment. Also, these sensors can be integrated into miniaturized electrochemical devices due to the use of a micro-cell to perform the measurements. The analysis using cyclic voltammetry presents an excellent tool to determine the detection properties of gold and silver nanocomposites.

The results obtained for *Ag*-based nanocomposite electrodes are promising, but the results in section 6.5.1 also suggest that electrodes with *Au*-based nanocomposites could also deliver comparable to *AgNPs/GO* modified electrodes based on preliminary studies on stability and kinetic parameters. Finally, other characterization techniques could be performed to analyze the specific shape of the nanoparticles, and the modified electrodes could be treated to obtain a more stable signal and improve their durability.

Bibliography

- [1] Vollath, D. Nanomaterials an introduction to synthesis, properties and application. *Environmental Engineering and Management Journal* **2008**, *7*, 865–870.
- [2] Medina, M.; Galván, L.; Reyes, R. Las nanopartículas y el medio ambiente. *Universidad Ciencia y Tecnología* **2016**, *19*.
- [3] Khan, I.; Saeed, K.; Khan, I. Nanoparticles: Properties, applications and toxicities. *Arabian journal of chemistry* **2019**, *12*, 908–931.
- [4] Nakamura, S.; Sato, M.; Sato, Y.; Ando, N.; Takayama, T.; Fujita, M.; Ishihara, M. Synthesis and application of silver nanoparticles (Ag NPs) for the prevention of infection in healthcare workers. *International journal of molecular sciences* **2019**, *20*, 3620.
- [5] Khan, A.; Rashid, R.; Murtaza, G.; Zahra, A. Gold nanoparticles: synthesis and applications in drug delivery. *Tropical journal of pharmaceutical research* **2014**, *13*, 1169–1177.
- [6] Chen, Y.; Ming, H. Review of surface plasmon resonance and localized surface plasmon resonance sensor. *Photonic Sensors* **2012**, *2*, 37–49.
- [7] Yeh, Y.-C.; Creran, B.; Rotello, V. M. Gold nanoparticles: preparation, properties, and applications in bionanotechnology. *Nanoscale* **2012**, *4*, 1871–1880.
- [8] Zhang, X.-F.; Liu, Z.-G.; Shen, W.; Gurunathan, S. Silver nanoparticles: synthesis, characterization, properties, applications, and therapeutic approaches. *International journal of molecular sciences* **2016**, *17*, 1534.
- [9] Huang, L.; Hou, K.; Jia, X.; Pan, H.; Du, M. Preparation of novel silver nanoplates/graphene composite and their application in vanillin electrochemical detection. *Materials Science and Engineering: C* **2014**, *38*, 39–45.
- [10] Oliveira, J. P.; Prado, A. R.; Keijok, W. J.; Ribeiro, M. R.; Pontes, M. J.; Nogueira, B. V.; Guimarães, M. C. A helpful method for controlled synthesis of monodisperse gold nanoparticles through response surface modeling. *Arabian Journal of Chemistry* **2020**, *13*, 216–226.

- [11] Chook, S. W.; Chia, C. H.; Zakaria, S.; Ayob, M. K.; Chee, K. L.; Huang, N. M.; Neoh, H. M.; Lim, H. N.; Jamal, R.; Rahman, R. Antibacterial performance of Ag nanoparticles and AgGO nanocomposites prepared via rapid microwave-assisted synthesis method. *Nanoscale research letters* **2012**, *7*, 1–7.
- [12] Zhang, Q.; Li, N.; Goebel, J.; Lu, Z.; Yin, Y. A Systematic Study of the Synthesis of Silver Nanoplates: Is Citrate a “Magic” Reagent? *Journal of the American Chemical Society* **2011**, *133*, 18931–18939, PMID: 21999679.
- [13] La relevancia de la luz en la formación de nanopartículas de metales coloidales. *Chemical Society Reviews*
- [14] Solati, E.; Dorrnian, D. Comparison between silver and gold nanoparticles prepared by pulsed laser ablation in distilled water. *Journal of Cluster Science* **2015**, *26*, 727–742.
- [15] Lu, X.; Qi, H.; Zhang, X.; Xue, Z.; Jin, J.; Zhou, X.; Liu, X. Highly dispersive Ag nanoparticles on functionalized graphene for an excellent electrochemical sensor of nitroaromatic compounds. *Chemical Communications* **2011**, *47*, 12494–12496.
- [16] others,, *et al.* A glassy carbon electrode modified with graphene oxide and silver nanoparticles for amperometric determination of hydrogen peroxide. *Microchimica Acta* **2016**, *183*, 911–916.
- [17] Zhong, L.; Gan, S.; Fu, X.; Li, F.; Han, D.; Guo, L.; Niu, L. Electrochemically controlled growth of silver nanocrystals on graphene thin film and applications for efficient nonenzymatic H₂O₂ biosensor. *Electrochimica Acta* **2013**, *89*, 222–228.
- [18] Ronkainen, N. J.; Halsall, H. B.; Heineman, W. R. Electrochemical biosensors. *Chemical Society Reviews* **2010**, *39*, 1747–1763.
- [19] Grieshaber, D.; MacKenzie, R.; Vörös, J.; Reimhult, E. Electrochemical biosensors-sensor principles and architectures. *Sensors* **2008**, *8*, 1400–1458.
- [20] Lu, W.; Luo, Y.; Chang, G.; Sun, X. Synthesis of functional SiO₂-coated graphene oxide nanosheets decorated with Ag nanoparticles for H₂O₂ and glucose detection. *Biosensors and Bioelectronics* **2011**, *26*, 4791–4797.
- [21] Saade, J.; de Araújo, C. B. Synthesis of silver nanoprisms: a photochemical approach using light emission diodes. *Materials Chemistry and Physics* **2014**, *148*, 1184–1193.
- [22] others,, *et al.* Gold nanoparticles: various methods of synthesis and antibacterial applications. *Front Biosci* **2014**, *19*, 1320–1344.
- [23] Korbekandi, H.; Irvani, S. *The delivery of nanoparticles*; IntechOpen, 2012.
- [24] Lee, S. H.; Jun, B.-H. Silver nanoparticles: synthesis and application for nanomedicine. *International journal of molecular sciences* **2019**, *20*, 865.

- [25] Bansal, V.; Li, V.; O'Mullane, A. P.; Bhargava, S. K. Shape dependent electrocatalytic behaviour of silver nanoparticles. *CrystEngComm* **2010**, *12*, 4280–4286.
- [26] Siwal, S. S.; Zhang, Q.; Devi, N.; Thakur, V. K. Carbon-based polymer nanocomposite for high-performance energy storage applications. *Polymers* **2020**, *12*, 505.
- [27] Milanova, V.; Petrov, T.; Chauvet, O.; Markova, I. Study of carbon-based nanocomposites with intermetallic (Co-Sn, Ni-Sn) nanoparticles. *Rev Adv Mater Sci* **2014**, *37*, 42–47.
- [28] Thomas, S.; Rafiei, S.; Maghsoodlou, S.; Afzali, A. *Foundations of nanotechnology, volume two: Nanoelements formation and interaction*; CRC Press, 2014.
- [29] Mansoori, G. A. *Principles of nanotechnology: molecular-based study of condensed matter in small systems*; World Scientific, 2005.
- [30] Gleiter, H. Nanoscience and nanotechnology: the key to new studies in areas of science outside of nanoscience and nanotechnology. *MRS bulletin* **2009**, *34*, 456–464.
- [31] Toumey, C. Plenty of room, plenty of history. *Nature nanotechnology* **2009**, *4*, 783–784.
- [32] Dowling, G. H. O. O. P. P. P. R. S. T. W. W., Clift *Nanoscience and nanotechnologies: opportunities and uncertainties*; 2004; p 116.
- [33] Arole, V.; Munde, S. Fabrication of nanomaterials by top-down and bottom-up approaches-an overview. *J. Mater. Sci* **2014**, *1*, 89–93.
- [34] Tiwari, J. N.; Tiwari, R. N.; Kim, K. S. Zero-dimensional, one-dimensional, two-dimensional and three-dimensional nanostructured materials for advanced electrochemical energy devices. *Progress in Materials Science* **2012**, *57*, 724–803.
- [35] Long, N. N.; Vu, L.; Kiem, C. D.; Doanh, S.; Nguyet, C.; Hang, P. T.; Thien, N.; Quynh, L. M. Synthesis and optical properties of colloidal gold nanoparticles. 2009.
- [36] Rad, A. G.; Abbasi, H.; Afzali, M. H. Gold nanoparticles: synthesising, characterizing and reviewing novel application in recent years. *Physics Procedia* **2011**, *22*, 203–208.
- [37] Singh, P.; Pandit, S.; Mokkapati, V.; Garg, A.; Ravikumar, V.; Mijakovic, I. Gold nanoparticles in diagnostics and therapeutics for human cancer. *International journal of molecular sciences* **2018**, *19*, 1979.
- [38] Maiti, D.; Tong, X.; Mou, X.; Yang, K. Carbon-based nanomaterials for biomedical applications: a recent study. *Frontiers in pharmacology* **2019**, *9*, 1401.
- [39] Gatto, F.; Bardi, G. Metallic nanoparticles: General research approaches to immunological characterization. *Nanomaterials* **2018**, *8*, 753.

- [40] Sau, T. K.; Rogach, A. L. *Complex-shaped metal nanoparticles: bottom-up syntheses and applications*; John Wiley & Sons, 2012.
- [41] others,, *et al.* Ceramic nanoparticles: fabrication methods and applications in drug delivery. *Current pharmaceutical design* **2015**, *21*, 6165–6188.
- [42] Sun, H.; Lv, L.; Bai, Y.; Yang, H.; Zhou, H.; Li, C.; Yang, L. Nanotechnology-enabled materials for hemostatic and anti-infection treatments in orthopedic surgery. *International Journal of Nanomedicine* **2018**, *13*, 8325.
- [43] Bangal, M.; Ashtaputer, S.; Marathe, S.; Ethiraj, A.; Hebalkar, N.; Gosavi, S.; Urban, J.; Kulkarni, S. *IWNMS 2004*; Springer, 2005; pp 81–94.
- [44] Ainyette, A. Synthesis of Semiconductor Nanoparticles. *NNIN REU 2006 Research Accomplishments. Materials* 48–49.
- [45] Stöber, W.; Fink, A.; Bohn, E. Controlled growth of monodisperse silica spheres in the micron size range. *Journal of colloid and interface science* **1968**, *26*, 62–69.
- [46] Jasmine, M. D. C.; Prabhu, V. V. Polymeric nanoparticles-the new face in drug delivery and cancer therapy. **2013**,
- [47] Rai, R.; Alwani, S.; Badea, I. Polymeric nanoparticles in gene therapy: New avenues of design and optimization for delivery applications. *Polymers* **2019**, *11*, 745.
- [48] Jiang, F.; Chen, S.; Cao, Z.; Wang, G. A photo, temperature, and pH responsive spiropyran-functionalized polymer: Synthesis, self-assembly and controlled release. *Polymer* **2016**, *83*, 85–91.
- [49] Zayats, A. V.; Smolyaninov, I. I.; Maradudin, A. A. Nano-optics of surface plasmon polaritons. *Physics reports* **2005**, *408*, 131–314.
- [50] Zayats, A. V.; Smolyaninov, I. I. Near-field photonics: surface plasmon polaritons and localized surface plasmons. *Journal of Optics A: Pure and Applied Optics* **2003**, *5*, S16.
- [51] Unser, S.; Bruzas, I.; He, J.; Sagle, L. Localized surface plasmon resonance biosensing: current challenges and approaches. *Sensors* **2015**, *15*, 15684–15716.
- [52] Hammond, J. L.; Bhalla, N.; Rafiee, S. D.; Estrela, P. Localized surface plasmon resonance as a biosensing platform for developing countries. *Biosensors* **2014**, *4*, 172–188.
- [53] Yang, G.; Li, L.; Lee, W. B.; Ng, M. C. Structure of graphene and its disorders: a review. *Science and technology of advanced materials* **2018**, *19*, 613–648.
- [54] Choi, W.; Lahiri, I.; Seelaboyina, R.; Kang, Y. S. Synthesis of graphene and its applications: a review. *Critical Reviews in Solid State and Materials Sciences* **2010**, *35*, 52–71.

- [55] Radadiya, T. M. A properties of graphene. *European Journal of Material Sciences* **2015**, 2, 6–18.
- [56] Pierson, H. O. *Handbook of carbon, graphite, diamonds and fullerenes: processing, properties and applications*; William Andrew, 2012.
- [57] Dinadayalane, T. C.; Leszczynska, D.; Leszczynski, J. *Towards Efficient Designing of Safe Nanomaterials*; 2012; pp 1–26.
- [58] Popov, V. N. Carbon nanotubes: properties and application. *Materials Science and Engineering: R: Reports* **2004**, 43, 61–102.
- [59] Odahara, G.; Ishikawa, T.; Otani, S.; Oshima, C. Self-Standing Graphene Sheets Prepared with Chemical Vapor Deposition and Chemical Etching. *e-journal of surface science and nanotechnology* **2009**, 7, 837–840.
- [60] Mikhailov, S. *Physics and Applications of Graphene: Experiments*; BoD–Books on Demand, 2011.
- [61] Banhart, F. Chains of carbon atoms: a vision or a new nanomaterial? *Beilstein journal of nanotechnology* **2015**, 6, 559–569.
- [62] Krueger, A. *Carbon materials and nanotechnology*; John Wiley & Sons, 2010.
- [63] Jorio, A.; Dresselhaus, M. S.; Saito, R.; Dresselhaus, G. *Raman spectroscopy in graphene related systems*; John Wiley & Sons, 2011.
- [64] Gray, D.; McCaughan, A.; Mookerji, B. Crystal structure of graphite, graphene and silicon. *Physics for Solid State Applications* **2009**, 6.
- [65] Perrozzi, F.; Prezioso, S.; Ottaviano, L. Graphene oxide: from fundamentals to applications. *Journal of Physics: Condensed Matter* **2014**, 27, 013002.
- [66] Khan, Z. U.; Kausar, A.; Ullah, H.; Badshah, A.; Khan, W. U. A review of graphene oxide, graphene buckypaper, and polymer/graphene composites: Properties and fabrication techniques. *Journal of plastic film & sheeting* **2016**, 32, 336–379.
- [67] Sun, L. Structure and synthesis of graphene oxide. *Chinese Journal of Chemical Engineering* **2019**, 27, 2251–2260.
- [68] Dreyer, D. R.; Todd, A. D.; Bielawski, C. W. Harnessing the chemistry of graphene oxide. *Chemical Society Reviews* **2014**, 43, 5288–5301.
- [69] Ray, S. C. Application and uses of graphene oxide and reduced graphene oxide. *Applications of graphene and graphene-oxide based nanomaterials* **2015**, 39–55.
- [70] Pandya, S. Nanocomposites and it's Application-Review. **2007**,

- [71] Camargo, P. H. C.; Satyanarayana, K. G.; Wypych, F. Nanocomposites: synthesis, structure, properties and new application opportunities. *Materials Research* **2009**, *12*, 1–39.
- [72] Din, S. H. Nano-Composites and their Applications: A review. *Characterization and Application of Nanomaterials* **2019**, *2*.
- [73] Sachinjith, K.; KR, S. K. A review on types of nanocomposites and their applications. *International Journal of Advance Research, Ideas and Innovations in Technology* **2018**, *4*.
- [74] Ebrahimi, F. *Nanocomposites: new trends and developments*; BoD–Books on Demand, 2012.
- [75] Khan, W. S.; Hamadneh, N. N.; Khan, W. A. Polymer nanocomposites–synthesis techniques, classification and properties. *Science and applications of Tailored Nanostructures* **2016**, 50.
- [76] Malaki, M.; Xu, W.; Kasar, A. K.; Menezes, P. L.; Dieringa, H.; Varma, R. S.; Gupta, M. Advanced metal matrix nanocomposites. *Metals* **2019**, *9*, 330.
- [77] Lateef, A.; Nazir, R. Metal nanocomposites: synthesis, characterization and their applications. *Sci. Appl. Tailored Nanostructures* **2017**, 239–256.
- [78] Rahmandoust, M.; Ayatollahi, M. R. *Characterization of carbon nanotube based composites under consideration of defects*; Springer, 2016; pp 5–63.
- [79] Devi, J. M.; Umadevi, M. Synthesis and characterization of silver–PVA nanocomposite for sensor and antibacterial applications. *Journal of Cluster Science* **2014**, *25*, 639–650.
- [80] Salah, B.; Ayesb, A. I. Fabrication and Characterization of Nanocomposite Flexible Membranes of PVA and Fe₃O₄. *Molecules* **2021**, *26*, 121.
- [81] Sanabria-Cala, J.; Rodriguez, G. C.; Gauthier, G.; Ladeira, L.; Catano, D. L.; Ballesteros, D. P.; Arenas, D. M. Gold Nanoparticles Formation Mechanism by Photochemical Synthesis. *Chemical Engineering Transactions* **2018**, *64*, 403–408.
- [82] Dong, S.; Tang, C.; Zhou, H.; Zhao, H. Photochemical synthesis of gold nanoparticles by the sunlight radiation using a seeding approach. *Gold bulletin* **2004**, *37*, 187–195.
- [83] Healy, N.; Rathbun, L. *Global Perspectives of Nanoscience and Engineering Education*; Springer, 2016; pp 323–349.
- [84] Powner, E.; Yalcinkaya, F. From basic sensors to intelligent sensors: definitions and examples. *Sensor Review* **1995**, *15*, 19–22.
- [85] McGrath, M. J.; Ni Scanail, C.; Nafus, D. *Sensor technologies: healthcare, wellness, and environmental applications*; Springer Nature, 2013.

- [86] Hanrahan, G.; Patil, D. G.; Wang, J. Electrochemical sensors for environmental monitoring: design, development and applications. *Journal of Environmental Monitoring* **2004**, *6*, 657–664.
- [87] Pohanka, M.; Skládal, P. Electrochemical biosensors—principles and applications. *Journal of applied biomedicine* **2008**, *6*.
- [88] Thévenot, D. R.; Toth, K.; Durst, R. A.; Wilson, G. S. Electrochemical biosensors: recommended definitions and classification. *Biosensors and bioelectronics* **2001**, *16*, 121–131.
- [89] Power, A. C.; Morrin, A. *Electrochemistry*; InTech Rijeka, 2013; pp 141–178.
- [90] Stradiotto, N. R.; Yamanaka, H.; Zandoni, M. V. B. Electrochemical sensors: a powerful tool in analytical chemistry. *Journal of the Brazilian Chemical Society* **2003**, *14*, 159–173.
- [91] Lindner, E. Konstantin N. Mikhelson: Ion-selective electrodes. *Analytical and bioanalytical chemistry* **2014**, *406*, 373–374.
- [92] Yadav, L. D. S. *Organic spectroscopy*; Springer Science & Business Media, 2013.
- [93] Akash, M. S. H.; Rehman, K. *Essentials of Pharmaceutical Analysis*; Springer, 2020.
- [94] Owen, A. *Fundamentals of UV-visible spectroscopy*. **1996**,
- [95] Faix, O. *Methods in lignin chemistry*; Springer, 1992; pp 83–109.
- [96] Berthomieu, C.; Hienerwadel, R. Fourier transform infrared (FTIR) spectroscopy. *Photosynthesis research* **2009**, *101*, 157–170.
- [97] Khan, S. A.; Khan, S. B.; Khan, L. U.; Farooq, A.; Akhtar, K.; Asiri, A. M. *Handbook of Materials Characterization*; Springer, 2018; pp 317–344.
- [98] Colthup, N. B. *Infrared spectroscopy*. **2003**,
- [99] Kuzmany, H. *Solid-state spectroscopy: an introduction*; Springer Science & Business Media, 2009.
- [100] Harris, D. MD and Bertolucci, Symmetry and Spectroscopy: An introduction to vibrational and electronic spectroscopy, edited by Anonymous. 1978.
- [101] Shipp, D. W.; Sinjab, F.; Notingher, I. Raman spectroscopy: techniques and applications in the life sciences. *Advances in Optics and Photonics* **2017**, *9*, 315–428.
- [102] John R. Ferraro, K. N.; Brown, C. W. *Introductory Raman Spectroscopy*, Second Edition. 2003.
- [103] Colthup, N.; Daly, L.; Wiberley, S. *Introduction to Infrared and Raman Spectroscopy*, Academic Press Limited. London, UK **1990**,

- [104] Aharinejad, S.; Lametschwandtner, A. *Microvascular Corrosion Casting in Scanning Electron Microscopy*; Springer, 1992; pp 44–51.
- [105] Mohammed, A.; Abdullah, A. Scanning electron microscopy (SEM): A review. 2018.
- [106] Kannan, M. *Scanning Electron Microscopy: Principle, Components and Applications*.
- [107] Kyeyune, B. Atomic force microscopy. *Africa Institute for Mathematical Science Tanzania*. DOI **2017**, 10.
- [108] Dufrêne, Y. F. Atomic force microscopy, a powerful tool in microbiology. *Journal of bacteriology* **2002**, 184, 5205–5213.
- [109] Jagtap, R.; Ambre, A. Overview literature on atomic force microscopy (AFM): Basics and its important applications for polymer characterization. **2006**,
- [110] Aliofkhazraei, M.; Ali, N. AFM Applications in Micro/Nanostructured Coatings. **2014**,
- [111] Braga, P. C.; Ricci, D. *Atomic force microscopy: biomedical methods and applications*; Springer Science & Business Media, 2004; Vol. 242.
- [112] Allen, J. B.; Larry, R. F. *Electrochemical methods fundamentals and applications*; John Wiley & Sons, 2001.
- [113] Khalafi, L.; Rafiee, M. Cyclic Voltammetry. *Encyclopedia of Physical Organic Chemistry* **2016**, 1–42.
- [114] PS, J.; Sutrave, D. A brief study of cyclic voltammetry and electrochemical analysis. *Int. J. ChemTech Res* **2018**, 11, 77–88.
- [115] Elgrishi, N.; Rountree, K. J.; McCarthy, B. D.; Rountree, E. S.; Eisenhart, T. T.; Dempsey, J. L. A practical beginner's guide to cyclic voltammetry. *Journal of Chemical Education* **2018**, 95, 197–206.
- [116] Zoski, C. G. *Handbook of electrochemistry*; Elsevier, 2006.
- [117] Nevell, T.; Walsh, F. Reference electrodes. *Transactions of the IMF* **1992**, 70, 144–147.
- [118] EC08, A. A. N. Basic overview of the working principle of a potentiostat/galvanostat (PGSTAT)– Electrochemical cell setup. *Metrohm Autolab. BV* **2011**, 1–3.
- [119] Wijeratne, K. *Conducting Polymer Electrodes for Thermogalvanic Cells*; Linköping University Electronic Press, 2019; Vol. 1971.
- [120] Lasso, E. Physical and Electrochemical Characterization of the Photochemically Growth of Silver Nanoplates on Graphene Oxide. *Yachay Tech University* **2020**,
- [121] Síntesis de nanocristales metálicos con control de forma: ¿la química simple se encuentra con la física compleja? *Angewandte Chemie International Edition*

- [122] Lavagnini, I.; Antiochia, R.; Magno, F. An extended method for the practical evaluation of the standard rate constant from cyclic voltammetric data. *Electroanalysis: An International Journal Devoted to Fundamental and Practical Aspects of Electroanalysis* **2004**, *16*, 505–506.
- [123] Çiplak, Z.; Yildiz, N.; Çalimli, A. Investigation of graphene/Ag nanocomposites synthesis parameters for two different synthesis methods. *Fullerenes, Nanotubes and Carbon Nanostructures* **2015**, *23*, 361–370.
- [124] Saravia, S. G. G. d.; Rastelli, S. E.; Angulo-Pineda, C.; Palza, H.; Viera, M. R. Anti-adhesion and antibacterial activity of silver nanoparticles and graphene oxide-silver nanoparticle composites. *Matéria (Rio de Janeiro)* **2020**, *25*.
- [125] Jeon, H. B.; Tsalu, P. V.; Ha, J. W. Shape effect on the refractive index sensitivity at localized surface plasmon resonance inflection points of single gold nanocubes with vertices. *Scientific reports* **2019**, *9*, 1–8.
- [126] Huang, X.; El-Sayed, M. A. Gold nanoparticles: Optical properties and implementations in cancer diagnosis and photothermal therapy. *Journal of advanced research* **2010**, *1*, 13–28.
- [127] Cobos, M.; De-La-Pinta, I.; Quindós, G.; Fernández, M. J.; Fernández, M. D. Graphene oxide–silver nanoparticle nanohybrids: Synthesis, characterization, and antimicrobial properties. *Nanomaterials* **2020**, *10*, 376.
- [128] Bae, Y.; Kim, N. H.; Kim, M.; Lee, K. Y.; Han, S. W. Anisotropic assembly of Ag nanoprisms. *Journal of the American Chemical Society* **2008**, *130*, 5432–5433.
- [129] Xue, C.; Métraux, G. S.; Millstone, J. E.; Mirkin, C. A. Mechanistic study of photomediated triangular silver nanoprism growth. *Journal of the American Chemical Society* **2008**, *130*, 8337–8344.
- [130] Goldstein, J. I.; Newbury, D. E.; Michael, J. R.; Ritchie, N. W.; Scott, J. H. J.; Joy, D. C. *Scanning electron microscopy and X-ray microanalysis*; Springer, 2017.
- [131] Sun, Y.; Xia, Y. Shape-controlled synthesis of gold and silver nanoparticles. *science* **2002**, *298*, 2176–2179.
- [132] Zhang, Q.; Li, N.; Goebel, J.; Lu, Z.; Yin, Y. A systematic study of the synthesis of silver nanoplates: is citrate a “magic” reagent? *Journal of the American Chemical Society* **2011**, *133*, 18931–18939.
- [133] Horcas, I.; Fernández, R.; Gomez-Rodriguez, J.; Colchero, J.; Gómez-Herrero, J.; Baro, A. WSXM: a software for scanning probe microscopy and a tool for nanotechnology. *Review of scientific instruments* **2007**, *78*, 013705.
- [134] Sellam, C.; Zhai, Z.; Zahabi, H.; Picot, O. T.; Deng, H.; Fu, Q.; Bilotti, E.; Peijs, T. High mechanical reinforcing efficiency of layered poly (vinyl alcohol)–graphene oxide nanocomposites. *Nanocomposites* **2015**, *1*, 89–95.
- [135] Ban, F.; Majid, S. R.; Huang, N. M.; Lim, H. Graphene oxide and its electrochemical performance. *Int. J. Electrochem. Sci* **2012**, *7*, 4345–4351.

- [136] Aziz, M.; Halim, F. S. A.; Jaafar, J. Preparation and characterization of graphene membrane electrode assembly. *Jurnal teknologi* **2014**, *69*.
- [137] others,, *et al.* Effect of graphene oxide doping on superconducting properties of bulk MgB₂. *Superconductor Science and Technology* **2013**, *26*, 095008.
- [138] Spectroscopy Tables. http://sdfs.db.aist.go.jp/sdfs/cgi-bin/direct_frame_top.cgi, 2017; Accessed: 31 March 2017.
- [139] Andrijanto, E.; Shoelarta, S.; Subiyanto, G.; Rifki, S. Facile synthesis of graphene from graphite using ascorbic acid as reducing agent. 2016.
- [140] Neelgund, G. M.; Oki, A. Graphene-coupled ZnO: a robust NIR-induced catalyst for rapid photo-oxidation of cyanide. *ACS omega* **2017**, *2*, 9095–9102.
- [141] Gurunathan, S.; Han, J.; Park, J. H.; Kim, J.-H. A green chemistry approach for synthesizing biocompatible gold nanoparticles. *Nanoscale research letters* **2014**, *9*, 1–11.
- [142] Koperuncholan, M. Bioreduction of chloroauric acid (HAuCl₄) for the synthesis of gold nanoparticles (GNPs): A special empathies of pharmacological activity. *Int. J. Phytopharm* **2015**, *5*, 72–80.
- [143] Gopinath, K.; Venkatesh, K.; Ilangovan, R.; Sankaranarayanan, K.; Arumugam, A. Green synthesis of gold nanoparticles from leaf extract of Terminalia arjuna, for the enhanced mitotic cell division and pollen germination activity. *Industrial crops and products* **2013**, *50*, 737–742.
- [144] Moshfegh, M.; Forootanfar, H.; Zare, B.; Shahverdi, A.; Zarrini, G.; Faramarzi, M. Biological synthesis of Au, Ag and Au-Ag bimetallic nanoparticles by α -amylase. *Dig. J. Nanomater. Bios* **2011**, *6*, 1419–1426.
- [145] Upadhyay, P.; Mishra, S. K.; Purohit, S.; Dubey, G.; Singh Chauhan, B.; Srikrishna, S. Antioxidant, antimicrobial and cytotoxic potential of silver nanoparticles synthesized using flavonoid rich alcoholic leaves extract of Reinwardtia indica. *Drug and chemical toxicology* **2019**, *42*, 65–75.
- [146] Gurunathan, S.; Han, J. W.; Park, J. H.; Kim, E.; Choi, Y.-J.; Kwon, D.-N.; Kim, J.-H. Reduced graphene oxide–silver nanoparticle nanocomposite: a potential anticancer nanotherapy. *International journal of nanomedicine* **2015**, *10*, 6257.
- [147] Sharma, N.; Sharma, V.; Jain, Y.; Kumari, M.; Gupta, R.; Sharma, S.; Sachdev, K. Synthesis and characterization of graphene oxide (GO) and reduced graphene oxide (rGO) for gas sensing application. 2017.
- [148] Govindaraju, S.; Ramasamy, M.; Baskaran, R.; Ahn, S. J.; Yun, K. Ultraviolet light and laser irradiation enhances the antibacterial activity of glucosamine-functionalized gold nanoparticles. *International journal of nanomedicine* **2015**, *10*, 67.

- [149] Amanulla, B.; Palanisamy, S.; Chen, S.-M.; Chiu, T.-W.; Velusamy, V.; Hall, J. M.; Chen, T.-W.; Ramaraj, S. K. Selective colorimetric detection of nitrite in water using chitosan stabilized gold nanoparticles decorated reduced graphene oxide. *Scientific reports* **2017**, *7*, 1–9.
- [150] Sandford, C.; Edwards, M. A.; Klunder, K. J.; Hickey, D. P.; Li, M.; Barman, K.; Sigman, M. S.; White, H. S.; Minter, S. D. A synthetic chemist's guide to electroanalytical tools for studying reaction mechanisms. *Chemical science* **2019**, *10*, 6404–6422.
- [151] Kadara, R. O.; Jenkinson, N.; Banks, C. E. Characterisation of commercially available electrochemical sensing platforms. *Sensors and Actuators B: Chemical* **2009**, *138*, 556–562.
- [152] Bard, A.; Mirkin, M. Scanning Electrochemical Microscopy Marcel Dekker. *New York* **2001**,
- [153] Krishnaveni, P.; Ganesh, V. Electron transfer studies of a conventional redox probe in human sweat and saliva bio-mimicking conditions. *Scientific reports* **2021**, *11*, 1–13.
- [154] Radhi, M.; Amir, Y.; Alwan, S.; Tee, T. Electrochemical effect of different modified glassy carbon electrodes on the values of diffusion coefficient for some heavy metal ions. 2013.
- [155] Radhi, M.; Al-Mulla, E. A. J.; Tan, W. Electrochemical characterization of the redox couple of Fe (III)/Fe (II) mediated by grafted polymer electrode. *Research on Chemical Intermediates* **2014**, *40*, 179–192.
- [156] Fayemi, O. E.; Adekunle, A. S.; Ebenso, E. E. Electrochemical determination of serotonin in urine samples based on metal oxide nanoparticles/MWCNT on modified glassy carbon electrode. *Sensing and Bio-Sensing Research* **2017**, *13*, 17–27.
- [157] Yuan, M.-M.; Zou, J.; Huang, Z.-N.; Peng, D.-M.; Yu, J.-G. PtNPs-GNPs-MWCNTs- β -CD nanocomposite modified glassy carbon electrode for sensitive electrochemical detection of folic acid. *Analytical and bioanalytical chemistry* **2020**, 1–14.
- [158] others,, *et al.* Fundamentals and applications. *Electrochemical methods* **2001**, *2*, 580–632.
- [159] Loock, H.-P.; Wentzell, P. D. Detection limits of chemical sensors: Applications and misapplications. *Sensors and Actuators B: Chemical* **2012**, *173*, 157–163.
- [160] Viswanathan, P.; Ramaraj, R. Polyelectrolyte assisted synthesis and enhanced catalysis of silver nanoparticles: Electrocatalytic reduction of hydrogen peroxide and catalytic reduction of 4-nitroaniline. *Journal of Molecular Catalysis A: Chemical* **2016**, *424*, 128–134.
- [161] Yang, Z.; Qi, C.; Zheng, X.; Zheng, J. Synthesis of silver nanoparticle at a gas/liquid interface in the presence of silver seeds and its application for electrochemical sensing. *Talanta* **2015**, *140*, 198–203.
- [162] Li, S.-J.; Hou, L.-L.; Chang, M.-Z.; Yan, J.-J.; Liu, L. A novel enzyme-free hydrogen peroxide sensor based on electrode modified with gold nanoparticles-overoxidized polydopamine composites. *Int. J. Electrochem. Sci* **2016**, *11*, 2887–2896.

